สมบัติไจแอนต์ไดอิเล็กตริกของเซรามิกคอปเปอร์ออกไซด์

นายธานินทร์ ปัจจุโส

วิทยานิพนธ์นี้เป็นส่วนหนึ่งของการศึกษาตามหลักสูตรปริญญาวิทยาศาสตรดุษฎีบัณฑิต
สาขาวิชาฟิสิกส์
มหาวิทยาลัยเทคโนโลยีสุรนารี
ปีการศึกษา 2552

GIANT DIELECTRIC PROPERTIES OF COPPER OXIDE CERAMICS

Thanin Putjuso

A Thesis Submitted in Partial Fulfillment of the Requirements for the

Degree of Doctor of Philosophy in Physics

Suranaree University of Technology

Academic Year 2009

GIANT DIELECTRIC PROPERTIES OF COPPER OXIDE CERAMICS

Suranaree University of Technology has approved this thesis submitted in partial fulfillment of the requirements for the Degree of Doctor of Philosophy.

Thesis Examining Committee

(Asst. Prof. Dr. Chinorat Kobdaj)
Chairperson

(Assoc. Prof. Dr. Prapun Manyum)
Member (Thesis Advisor)

(Assoc. Prof. Dr. Santi Maensiri)
Member

(Asst. Prof. Dr. Prayoon Songsiriritthigul)
Member

(Dr. Teerapon Yamwong)
Member

(Prof. Dr. Sukit Limpijumnong)
Vice Rector for Academic Affairs

(Assoc. Prof. Dr. Prapun Manyum)
Dean of Institute of Science

ธานินทร์ ปัจจุโส : สมบัติไจแอนต์ไดอิเล็กตริกของเซรามิกคอปเปอร์ออกไซด์ (GIANT DIELECTRIC PROPERTIES OF COPPER OXIDE CERAMICS)
อาจารย์ที่ปรึกษา : รองศาสตราจารย์ ดร.ประพันธ์ แม่นยำ, 153 หน้า.

วิทยานิพนธ์นี้เกี่ยวข้องกับการศึกษาคุณสมบัติไดอิเล็กตริกเซรามิกคอปเปอร์ออกไซด์ที่เตรียมจากผงคอปเปอร์ออกไซด์ที่แตกต่างกันสามวิธี ได้แก่ ผงคอปเปอร์ออกไซด์ที่ใช้ทางการค้า เตรียมด้วยการสลายตัวทางความร้อนอย่างง่าย และโดยวิธีการทางสารละลาย ผงคอปเปอร์ออกไซด์ที่เตรียมด้วยวิธีการสลายตัวทางความร้อนและวิธีการทางสารละลายถูกนำมาแคลไซด์ที่อุณหภูมิ 500 600 และ 700°C 6 ชั่วโมง หลังจากนั้นคอปเปอร์ออกไซด์ที่ได้ถูกนำมาศึกษาด้วยเทคนิคการเลี้ยวเบนรังสีเอกซ์ (XRD) และกล้องจุลทรรศน์อิเล็กตรอนแบบส่องกราด (SEM) จากผลการวิเคราะห์ด้วยเทคนิคการเลี้ยวเบนด้วยรังสีเอกซ์ พบว่า ผงคอปเปอร์ออกไซด์ที่เตรียมประกอบด้วยเฟสของคอปเปอร์ออกไซด์มีขนาดของอนุภาคในช่วง 33-39 นาโนเมตรและ 26-34 นาโนเมตร สำหรับผงของคอปเปอร์ออกไซด์ที่เตรียมด้วยการสลายตัวทางความร้อนและสารละลาย ตามลำดับ ส่วนขนาดอนุภาคของคอปเปอร์ออกไซด์ที่เตรียมโดยใช้สารทางการค้ามีขนาดประมาณ 43 นาโนเมตร และพบว่าผงของคอปเปอร์ออกไซด์ที่เตรียมด้วยวิธีต่างๆ แสดงพีคหลักของคอปเปอร์ออกไซด์โดยไม่มีพีคอื่นเจือปน ส่วนผลจากการศึกษาโดยกล้องจุลทรรศน์อิเล็กตรอนแบบส่องกราดพบว่า ขนาดของอนุภาคมีค่าเพิ่มขึ้นเมื่อเพิ่มอุณหภูมิแคลไซด์ หลังจากนั้นนำผงคอปเปอร์ออกไซด์ที่เตรียมได้มาอัดเม็ด และแยกเผาผนึกขึ้นรูปที่อุณหภูมิ 900°C และ 950°C เป็นเวลา 10 ชั่วโมง ในบรรยากาศ จากผลการศึกษาลักษณะสัณฐานวิทยาพื้นผิวของเซรามิกคอปเปอร์ออกไซด์ที่เตรียมได้พบว่า ขนาดของเกรนอยู่ในช่วง 2-3 2-11 และ 1-36 ไมโครเมตร สำหรับเซรามิกที่เตรียมจากผงที่ใช้ทางการค้า ผงที่ได้จากการสลายตัวทางความร้อน และผงที่ได้จากวิธีสารละลาย ตามลำดับ ผลการศึกษาสมบัติไดอิเล็กตริกในช่วงอุณหภูมิ -50°C ถึง 100°C และที่ความถี่ 100 Hz ถึง 1 MHz พบว่า วัสดุเซรามิกคอปเปอร์ออกไซด์ที่เตรียมได้มีค่าไดอิเล็กตริกสูงมากโดยมีค่าประมาณ $10^4 - 10^5$ ในช่วงความถี่ 1-100 kHz และพบพฤติกรรมการปลดปล่อยพลังงานคล้ายเดอบาย ในช่วงอุณหภูมิต่ำพฤติกรรมทางไดอิเล็กตริกดังกล่าวสามารถอธิบายได้โดยอาศัยแบบจำลองสเปกตรัมความต้านทานเชิงซ้อน ซึ่งประกอบไปด้วยส่วนประกอบภายนอก ได้แก่ อิเล็กโทรดและชั้นฉนวน และส่วนประกอบภายใน ได้แก่ เกรนและขอบเขตของเกรน การวิเคราะห์ผลการทดลองโดยใช้แบบจำลองดังกล่าว พบว่า ความต้านทานเชิงซ้อนของส่วนประกอบภายนอกมีค่ามากกว่าความต้านทานเชิงซ้อนของส่วนประกอบภายใน และค่าไดอิเล็กตริกของเซรามิกเหล่านี้ลดลงหลังจากนำไปเผาภายใต้บรรยากาศอาร์กอน และกลับคืนมาเพิ่มขึ้นอีกครั้งหลังจากนำกลับมา

เผาภายใต้บรรยากาศออกซิเจนที่อุณหภูมิ 700°C เป็นเวลา 2 ชั่วโมง การลดลงและการเพิ่มขึ้นของค่าไดอิเล็กตริกมีความสัมพันธ์กับปริมาณออกซิเจนเวคเคนซี (ออกซิเจนไอออน) ในวัสดุคอปเปอร์ออกไซด์ และยังพบว่าค่าไดอิเล็กตริกของวัสดุคอปเปอร์ออกไซด์ที่เตรียมโดยวิธีการสลายตัวทางความร้อนมีค่าสูงกว่าวัสดุคอปเปอร์ออกไซด์ที่เตรียมจากผงคอปเปอร์ออกไซด์ที่ใช้ทางการค้า และที่เตรียมด้วยวิธีทางสารละลาย ส่วนค่าการสูญเสียทางไดอิเล็กตริกของวัสดุคอปเปอร์ออกไซด์ที่เตรียมด้วยวิธีการสลายตัวทางความร้อนมีค่าสูงกว่าวัสดุคอปเปอร์ออกไซด์ที่เตรียมจากผงคอปเปอร์ออกไซด์ในทางการค้าและที่เตียมจากวิธีทางสารละลาย นอกจากนี้ยังพบว่า ค่าคงที่ไดอิเล็กตริกมีค่าลดลงเมื่อเพิ่มความต่างศักย์และกระแสตรงระหว่างทำการวัดค่าคงที่ไดอิเล็กตริก ซึ่งการลดลงของค่าไดอิเล็กตริกนี้เกิดจาก ประจุอิสระได้รับพลังงาน และสามารถข้ามบ่อศักย์ขององค์ประกอบภายนอกของวัสดุคอปเปอร์ออกไซด์ จากการศึกษาผลของความเค้นอัดแกนเดี่ยว พบว่า ค่าคงที่ไดอิเล็กตริกและค่าการสูญเสียทางไดอิเล็กตริกของวัสดุคอปเปอร์ออกไซด์มีค่าเพิ่มขึ้นเมื่อเพิ่มขนาดความเค้นจนมีค่าสูงสุด และจากนั้นมีค่าลดลงเมื่อเพิ่มขนาดความเค้น พฤติกรรมทางไดอิเล็กตริกที่ขึ้นกับความเค้นนี้ สามารถอธิบายได้โดยการโพลาไรซ์ทางไฟฟ้าที่รอยต่อระหว่างอิเล็กโตรดกับผิวของวัสดุตัวอย่าง

สาขาวิชาฟิสิกส์ ลายมือชื่อนักศึกษา____________________
ปีการศึกษา 2552 ลายมือชื่ออาจารย์ที่ปรึกษา____________________
ลายมือชื่ออาจารย์ที่ปรึกษาร่วม____________________

THANIN PUTJUSO : GIANT DIELECTRIC PROPERTIES OF
COPPER OXIDE CERAMICS. THESIS ADVISOR : ASSOC. PROF.
PRAPUN MANYUM, D.Phil. 153 PP.

DIELECTRIC/COPPER OXIDE/SEM/XRD

This thesis is concerned with the study of the dielectric properties of CuO ceramics prepared from the CuO powder obtained from commercial, direct thermal decomposition (DT) and polymer pyrolysis solution route (PR) methods. The DT and PR prepared precursors were calcined at 500, 600 and 700°C in air for 6 h to obtained the crystalline CuO powders with the particle size in the range of 33 - 39 nm and 26 - 34 nm for the DT and PR powders, respectively. The particles size of the commercial crystalline powder is about 43 nm. XRD analysis of these powders shows main phase of the CuO. SEM micrographs reveal that the particle size of the powders increased with increasing calcination temperature. CuO ceramics are prepared from the synthesized powders by sintering. Sintering is conducted in air at 900°C and 950°C for 10 h. The grain sizes of the ceramics obtained from the sintering of the commercial, DT and PR powder are in the range of 2 - 3 μm, 2 - 11 μm and 1 - 36 μm, respectively. All of the sintered CuO ceramics show similar dielectric behavior at the temperature between -50 to 100°C at the frequency between 100 Hz to 1 MHz. Specifically, they exhibit a Debye-like relaxation and showed giant dielectric response with a giant dielectric constant of $\varepsilon' \sim 10^4$ - 10^5 in the frequency range of 1 - 100 kHz. To study the annealing effect on the dielectric properties, the obtained ceramics are then annealed in Ar atmosphere. The dielectric behavior of the as-, Ar-samples can be explained based on a impedance spectroscopy (IS) model. This impedance spectroscopy model and its equivalent circuit consist of a series connection with external and internal part. From the fitting results with this model, it is found that the external resistance (R_{ext}) is higher than the internal resistance (R_{int}). The dielectric constant of these ceramics is decreased after annealing in argon, and can be increased again by re-annealing in oxygen at 700°C for 2 h. The decrease and increase of the dielectric constant are closely related to the concentration of the oxygen vacancies (oxygen ion) in the ceramics. The giant dielectric constant of the ceramics prepared from the DT powder is higher than those of the ceramics prepared from the commercial and PR powder. The dielectric loss tangent of the DT ceramics is higher than those of the other two ceramics. In addition, the dielectric constant is decreased with the increase in the dc-bias voltage since free charge carriers activate to overcome the potential well of the external part of CuO ceramics. The dielectric constant and dielectric loss tangent depend also on the uniaxial compressive stress. Both parameters increase to the maximum value with increasing the compressive stress. They then begin to decrease with further increasing of the compressive stress. This stress-dependent dielectric behavior can be ascribed based on the electrical polarization at interface between electrode and sample surface.

School of Physics
Academic Year 2009

Student's Signature ____________________
Advisor's Signature ____________________
Co-Advisor's Signature ________________

ACKNOWLEDGEMENTS

I would like to express the gratitude to my advisor Assoc. Prof. Dr. Prapun Manyum for his guidance, his patience, his kind support, and his help in proofreading the thesis. I would like to express the appreciation to my co-advisor Assoc. Prof. Dr. Santi Maensiri for his warm hospitality, his advice, his kind support and his kind assistance during my visit at the Department of Physics, Khonkaen University, Thailand. I would like to express the appreciation to Asst. Prof. Dr. Ekaphan Swatsithang for his warm hospitality, his advice, his kind support and his kind assistance during my visit at the Department of Physics, Khonkaen University, Thailand. I thank Asst. Prof. Dr. Prayoon Songsiriritthigul, Asst. Prof. Dr. Chinorat Kobdaj, and Dr. Teerapon Yamwong for contributing as the thesis-examining committees. I thank Asst. Prof. Dr. Rattikorn Yimnirun and Mr. Prasit Thongbai for their advices and his help with some parts of my thesis. I acknowledge MTEC, Thailand. I thank the faculties and friends at the School of Physics, Suranaree University of Technology for their guidances and friendships. I would like to thank my friends in the Crystal Growth Physics Group. I would like to thank my friends in SSMG group, Khon Kaen University for their friendships and helpful discussions. Finally, I would like to express thanks to my parents, my wife, and my sister for their love, encouragement and support.

Thanin Putjuso

CONTENTS

Page

CHAPTER

CONTENTS (Continued)

CONTENTS (Continued)

LIST OF TABLES

LIST OF TABLES (Continued)

Table **Page**

LIST OF FIGURES

LIST OF FIGURES (Continued)

LIST OF FIGURES (Continued)

LIST OF FIGURES (Continued)

LIST OF FIGURES (Continued)

LIST OF FIGURES (Continued)

Figure **Page**

LIST OF FIGURES (Continued)

Figure **Page**

LIST OF FIGURES (Continued)

Figure **Page**

LIST OF FIGURES (Continued)

LIST OF FIGURES (Continued)

Figure **Page**

LIST OF FIGURES (Continued)

Figure **Page**

LIST OF FIGURES (Continued)

Figure **Page**

LIST OF FIGURES (Continued)

LIST OF FIGURES (Continued)

LIST OF FIGURES (Continued)

LIST OF FIGURES (Continued)

LIST OF ABBREVIATIONS

A	The plate capacitor of area
$A^*(\text{orY}^*)$	The complex admittance
A'	The real part of admittance
A''	The imaginary part of admittance
Z^*	The complex impedance
Z'	The real part of complex impedance
Z''	The imaginary part of complex impedance
β	The full width at half maximum
β_0	The widths from the observed X-ray
β_i	The width due to instrumental effects
C	The capacitance
C^*	The complex capacitance
C_{db}	The domain boundary capacitance
C_g	The grain capacitance
C_{gb}	The grain boundary capacitance
C_0	The vacuum capacitance
C_p	The parallel capacitance
D	The crystallite size
$\vec{D}$	The total electric flux density
d_{hkl}	The d-spacing
$\vec{d}$	The distance of separated charges

LIST OF ABBREVIATIONS(Continued)

$\vec{E}$	The electric field
$\vec{E}_C$	The field from the sample outside the cavity
$\vec{E}_L$	The local electric field
$\vec{E}_P$	The field due to charge on the electrodes
E_r	The activation energy
e^-	The electron
ε^*	The complex permittivity
ε'	The dielectric constant
ε''	The dielectric loss
ε_0	The permittivity of free space
$\vec{\mu}, < \vec{\mu} >$	The average dipole moment
G_P	The AC conductance
d_s	The thickness of the sample
I	The current
I^*	The complex current
I_C	The imaginary part of complex current
I_R	The real part of complex current
i	The Boltzmann constant
k	The number of dipoles
N	The oxygen ion at its normal site
O_0	The dipole charge

LIST OF ABBREVIATIONS(Continued)

$\vec{P}$	The electrical charge
Q	The resistor
R	The domain boundary resistance
R_{db}	The gain resistance
R_g	The grain boundary resistance
$R_g b$	The parallel resistance
σ	The conductivity
α	The total polarizability
α_d	The orientation polarizability
α_e	The electronic polarizability
α_i	The ionic polarizability
α_s	The space charge polarizability
θ	The scattering angle (or Bragg angle)
T	Temperature (Kelvin)
t	Time
$\tan\delta$	The dielectric loss tangent
τ	The relaxation time
DT	Direct thermal decomposition method
PR	Polymer pyrolysis solution route method

CHAPTER I

INTRODUCTION

1.1 Introduction

Dielectric oxides constitute a large proportion of materials which are having large-scale technological applications. Recently, there is an increasing demand on dielectric materials to surpass their present abilities to be of use in the fast changing world of electronic devices. Hence, search for new method and new materials which an unusual property is of great importance. Giant dielectric materials ($\varepsilon' \sim 10^4$) have been attracting much attention due to their potential applications in the microelectronic industry. $CaCu_3Ti_4O_{12}$ (Subramanian et al., 2000; Ramirez et al., 2000; Maensiri et al., 2007; Masingboon, 2008; Thongbai et al., 2008b), $Li_xTi_yNi_{1-x-y}O$ (Thongbai et al., 2008c), $A(Fe_{1/2}B_{1/2})O_3$ (A = Ba, Sr, Ca and $6B$ = Nb, Ta, Sb) (Raevski et al., 2003), and CuO (Sarkar et al., 2006; Sarkar et al., 2008a; Sarkar et al., 2008b; Thongbai et al., 2008b; Thongbai et al., 2008c) ceramics are included in the group of so-call "giant dielectric material". It was found that the electrically heterogeneous structure, i.e., semiconducting grain and insulating grain boundary (GB), can be observed in these materials (Sinclair et al., 2002; Liu et al., 2006; Sarkar et al., 2008a). Thus, it is widely accepted that the origin of the giant dielectric properties in these materials is associated with internal barrier layer capacitance (IBLC) effect, based on the interfacial polarization (Maxwell-Wagner polarization) at the GB (Chung et al., 2004; Liu et al., 2005) and/or electrodes (Lunkenheimer et al., 2004). However, the completed explanation of such giant dielectric behavior in these materials is not completely understood. All of these giant dielectric materials are of great interest because they are lead free environmentally friendly materials. Among of the giant dielectric materials, CuO ceramic show a greatest motivation due to its low cost and simple compound. Moreover, CuO can easy be prepared in the pure form and available commercially on a large scale. There was reported that the giant dielectric properties were contributed by the electrical response of grain and GB (Sarkar et al., 2008a). The grain contribution shows a significant role for the giant dielectric behavior at low temperature, whereas the GB contribution is evidence around room temperature and above. Most recently (Thongbai et al., 2008b), it was found that such grain contribution was affected by the grain size. Moreover, it was found that the dc bias had a remarkable influence on the GB contribution. These were supported by the study of the ac electrical conductivity of the CuO ceramics (Thongbai et al., 2008c). However, the reason why grain and GB contribute to the giant dielectric is not completely understood. (Sarkar et al., 2008a), suggested that the contribution of grain might be due to the presence of defects such as oxygen vacancies and existence of internal domains, but the experiments that may use to elucidate these suggestions has not been carried out.

It is widely accepted that the concentration of oxygen vacancies in many oxide ceramics has remarkable effect on their electrical properties. In general, the concentration of oxygen in oxide ceramics can be increased (decreased) by annealing these ceramic in oxidizing atmosphere, i.e annealed in O_2 at intermediately temperature (reducing atmosphere, i.e., annealed in N_2 or Ar)

In this thesis, I study the synthesis and giant dielectric properties of CuO ceramics prepared by a variety of methods including direct thermal decomposition method and solution routes such as polymer-pyrolysis route. These methods are chemical process, which has received considerable attention due to its relative simplicity and usefulness for obtaining a homogeneous and fine powder precursor. The synthesized fine CuO powders are characterized by thermo-gravimetric and different thermal analysis (TG-DTA), X-rays diffraction (XRD), scanning electron microscopy (SEM). Then, the CuO ceramics fabricated using powders prepared by direct thermal decomposition method and solution routes, are sintered in the temperatures at 900 and 950°C for 10h in air. The dielectric properties of CuO ceramics are measured using a Hewlett Packard 4194A Impedance Gain Phase Analyzer at an oscillation voltage of 1 V. The giant dielectric behavior of sintered samples and samples with post-sintering annealing in argon and oxygen is discussed. Moreover, the effects of the dc-bias voltage and uniaxial compressive stress on the giant dielectric response in these CuO ceramics are investigated

1.2 Research objectives

1.2.1 To synthesize CuO powders using a direct thermal decomposition and polymer-pyrolysis solution methods and use these prepared powders for fabrication of CuO ceramics.

1.2.2 To characterize the properties of the obtained CuO powders and ceramics.

1.2.3 To study the dielectric properties of CuO ceramics as functions of frequency, temperature, dc-bias voltage and uniaxial compressive stress.

1.2.4 To gain better understanding concerning with the origin of the observed giant dielectric response in the CuO ceramics.

1.3 Expected results

1.3.1 Single phase CuO powder can be prepared by the direct thermal decomposition method and by the polymer-pyrolysis solution route methods.

1.3.2 Understanding the dielectric properties of the CuO ceramics as functions of frequency, temperature, dc-bias voltage and uniaxial compressive stress.

1.3.3 Better understanding about the origin of the observed giant dielectric response in the CuO ceramics.

1.3.4 At least two papers carrying out in this work will be published in the international Journal.

CHAPTER II

REVIEW OF STRUCTURE AND GIANT DIELECTRIC PROPERTIES OF CuO

This chapter presents the reviews of structural and giant dielectric properties of CuO ceramics. The effect of the processing parameter on dielectric properties of CuO material is included together with the recent results on the effect of uniaxial compressive stress on the giant dielectric constant.

2.1 Structure and thermal analysis of CuO

The CuO belongs to the monoclinic crystal system, with a crystallographic point group of 2/m or C_{2h}. The space group of its unit cell is C2/c, and its lattice parameters are $a = 4.6837(5), b = 3.4226(5), c = 5.1288(6), \alpha = 90^\circ, \beta = 99.54(1)^\circ, \gamma = 90^\circ$ (http://en.wikipedia.org/wiki/CuO). The copper atom is coordinated by 4 oxygen atoms in an approximately square planar configuration. Collins and co-workers (1989) reported the preparation of CuO by oxidation of copper metal and decomposition of the nitrate. The structure (Figure 2.1) shows copper with essentially square planar coordination of oxygen atoms around the copper atoms. The apace group is also C2/c with unit cell dimensions $a = 4.6837(5)\mathring{A}$, $b = 3.4226(5)\mathring{A}$, $c = 5.1288(6)\mathring{A}$ and $\beta = 99.54(1)\mathring{A}$. Each copper atom has four oxygen neighbors at 1.96 .

A. Y. Obaid and co-worker (2000) reported the kinetic of thermal decomposition of the $Cu(CH_3COO)_2.H_2O$ powder which was studied in air and nitrogen

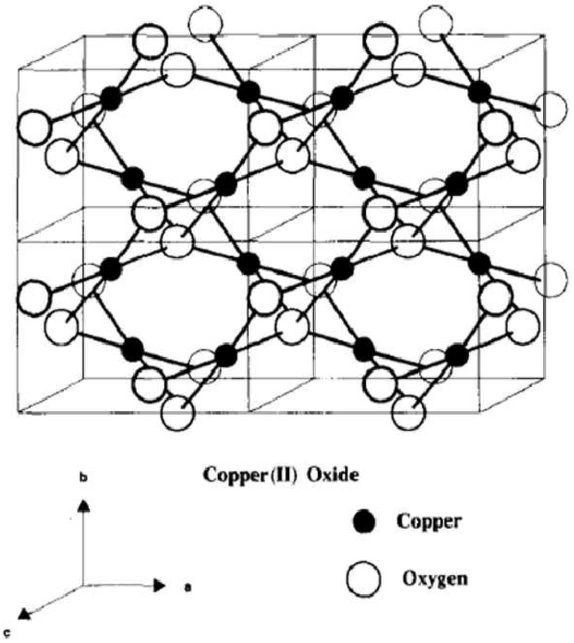

Figure 2.1 Structure of CuO (Collins et al., 1989).

atmospheres by means of DTA-TG (Figure 2.2) and SEM measurements (Figure 2.3). The kinetics of the thermal decomposition steps in air was studied using isothermal and non-isothermal thermo-gravimetric techniques. The results were discussed in terms of various reaction interface models and different techniques of computational analysis of non-isothermal data. The activation parameters, calculated by using a composite method of integral analysis of non-isothermal data, revealed not only their independence from the heating rate and fractional reaction, but also a better correlation and agreement with the results obtained under isothermal conditions.

2.2 Dielectric behavior of CuO ceramics

The dielectric properties of CuO material was first reported by (Sarkar et al., 2006). They first reported the giant dielectric response in pure copper (II) oxide (CuO) ceramics. The giant dielectric constant of this oxide was found to

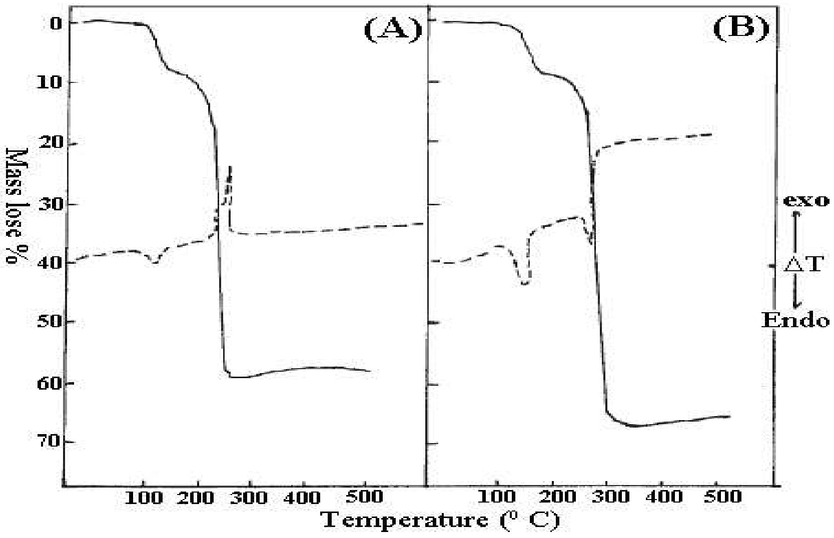

Figure 2.2 TG-DTA curves for the $Cu(CH_3COO)_2.H_2O$ powder in (A) air and (B) nitrogen at a heating rate of 15°C (Obaid et al., 2000).

be about $10^4 - 10^5$ at low frequencies. It is interesting that these high values of dielectric constant are not associated with any impurities of the dopants. Thus, the grain boundary effect on the electrical conductivity, which usually originates from a grain boundary potential barrier, did not relate to the impurity phase at the grain boundary. However, it was proposed that the different valence states of Cu^{2+} and Cu^{3+} were detected in the microstructure of the CuO ceramics; Cu^{3+} was found to be rich inside the grains, but indigent at the grain boundaries (Sarkar et al., 2008a).

The different electrical conductivities between the grains and grain boundaries of the CuO ceramics were attributed to the difference in the amount of Cu^{3+} between these two regions. Thus, the observed giant dielectric properties of CuO ceramics were suggested to the interfacial polarization at the interfaces of grain boundaries (Sarkar et al., 2006). Dielectric spectroscopy analysis revealed that the grain contribution played a major role for the giant dielectric constant value at low temperature, whereas grain boundary contribution dominated around room

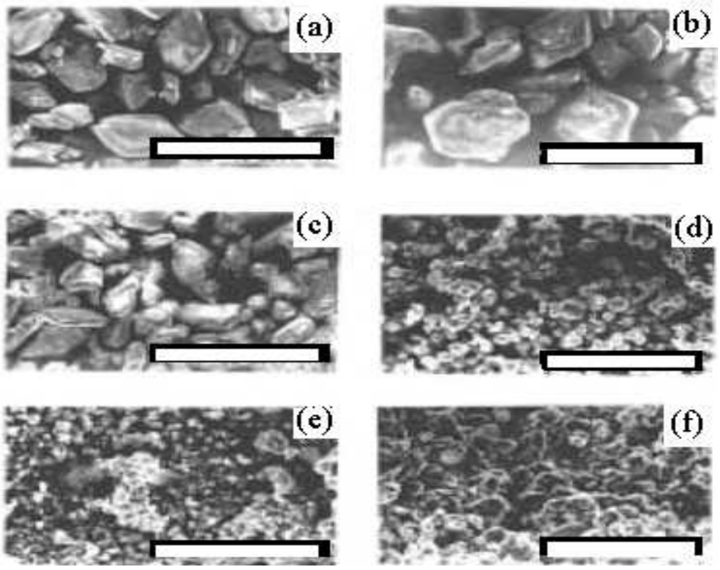

Figure 2.3 SEM micrograph revealed the changes in texture and morphology that accompany the thermal decomposition of $Cu(CH_3COO)_2.H_2O$ in air: (a) parent compound at room temperature, displaying relatively large crystals of different sizes, (b) parent compound after partial dehydration at 120°C, (c) sample calcined at 200°C after complete dehydration of the parent compound to the anhydrous salt, (d) sample calcined at 300°C, showing partial decomposition and fissioning of the anhydrous salt, (e) sample calcined at 500°C, showing complete decomposition of the anhydrous salt into small crystallites with a cubic crystal habit and some aggregation of particles and (f) sample calcined at 800°C, showing coalescence of the small crystallites into large aggregates accompanying the oxidation of Cu to CuO (scale bar: a, b and c . 100 mm; d, e and f . 10 mm) (Obaid et al., 2000).

temperature and above (Sarkar et al., 2008a). To date, only a few studies have investigated the electrical and dielectric properties of the CuO ceramics. The effects of ions doping and dc-bias on the dielectric and the related electrical properties of the CuO ceramics are still missing.

Other special features of CuO were also discovered by (Sarkar et al., 2006). They found that the dielectric constant is about 10^4, almost independent of temperature (above 230 K) and frequency in kilohertz region and suddenly decrease at the temperatures below 150 K (Figure 2.4). In addition to the fact that CuO holds a large dielectric constant that barely varies in the temperature range from 150 K to 350 K as shown in Figure 2.4. The reported dielectric loss, or $\tan\delta$

shows in Figure 2.5 is less than 10 when the temperature is higher than 300 K and a large peak occurs at around 200 K. Frequency dependence is also shown from 150 K to 350 K in a wide frequency range between 1 kHz to 1 MHz for both dielectric constant and loss. With the increasing frequency, the dielectric constant decreases in the entire temperature range and the dielectric loss peak shifts to higher temperatures with small increase in the maximum value of the peak. This behavior satisfies the relaxation excitation well. The origin of the giant dielectric constant in CuO comes from the excess hole, the conduction mechanism in CuO mainly governed by hole hopping between Cu^{2+} and Cu^{3+}. Hopping of holes produces Cu^{2+} around Cu^{3+} causing CuO grains to be enriched with Cu^{3+} (P-type conductance) which become semiconducting.

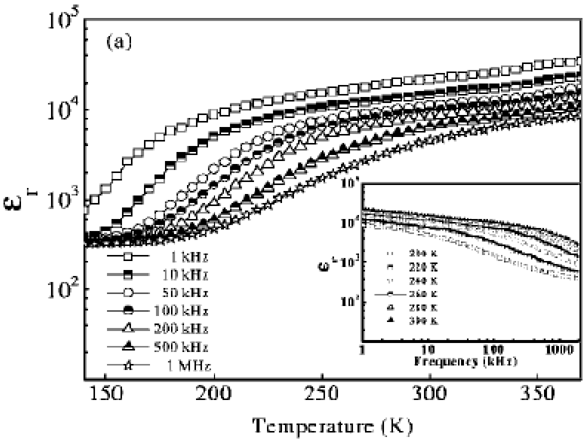

Figure 2.4 (a)Temperature-dependence of dielectric constant of CuO at selected frequencies. The inset displays frequency dependent dielectric constant of CuO at various fixed temperatures (Sarkar et al., 2006).

To support the earlier report (Sarkar et al., 2008a) presented the dielectric spectroscopy study elucidating the grains and grain boundary (GB) contributions to the total $\kappa \sim 10^4$ of CuO. Impedance spectroscopy (IS) analysis has also been carried out to interpret the electrical behavior of grains and grains boundary to show that the high κ response in the sample is associated with internal barrier

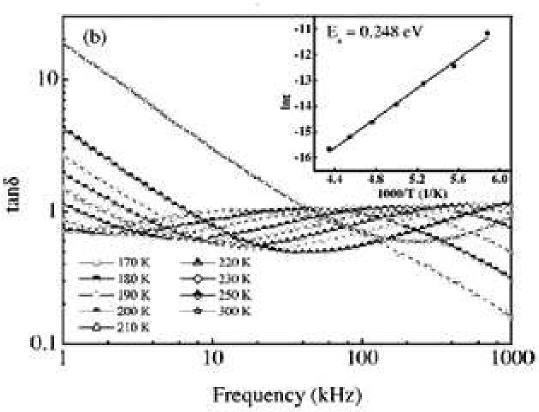

Figure 2.5 (b)Dielectric loss tangent, $\tan\delta$, of CuO at different fixed temperatures. The inset shows typical Arrhenius plot or the relaxation time τ with inverts temperature of CuO sample (Sarkar et al., 2006).

layer capacitance effect. Figure 2.6 shows the grains and GBs with average grain size of about 1.4 μm

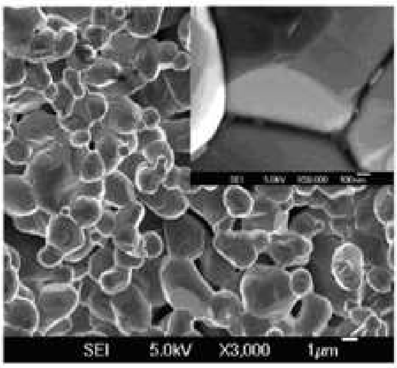

Figure 2.6 SEM micrograph of CuO presenting reasonably uniform microstructure of the ceramic with average grain size about 1.4 μm. The inset shows distinct GBs thickness about $\sim$ 15 - 20 μm surrounding CuO grains (Sarkar et al., 2008a).

The frequency dependent dielectric permittivity of CuO measured within the temperatures 160 - 320 K is shown in Figure 2.7. The dotted line separates the response of grains and grain boundary to the total dielectric permittivity. It is seen from Figure 2.7. (inset) that transition frequency (T_f) between grains and GBs response increases with increasing temperature.

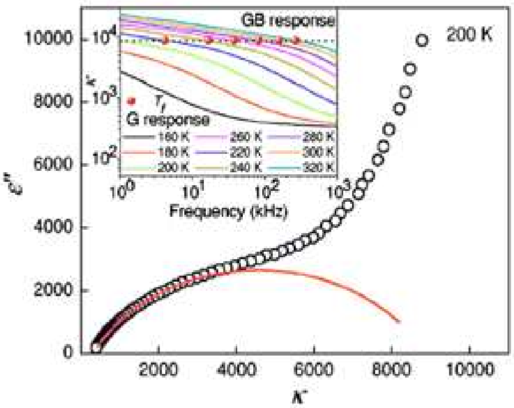

Figure 2.7 Cole-Cole plot of CuO at 170 K revealing the $\varepsilon_s \sim 8832$. The inset depicts the frequency dependence of dielectric permittivity of CuO at different fixed temperatures showing the contribution of grains and GB to the overall dielectric response of CuO ceramic (Sarkar et al., 2008a).

At 160 K, the dielectric constant is mainly due to grains while GB contribution starts at above 200 K. It is seen that at room temperature (RT ~ 300 K), the contribution of the grain effect is about 8800 out of the total dielectric constant of about 21000 (inset of Figure 2.7) which signifies that GB response dominates over grain contribution at room temperature and above.

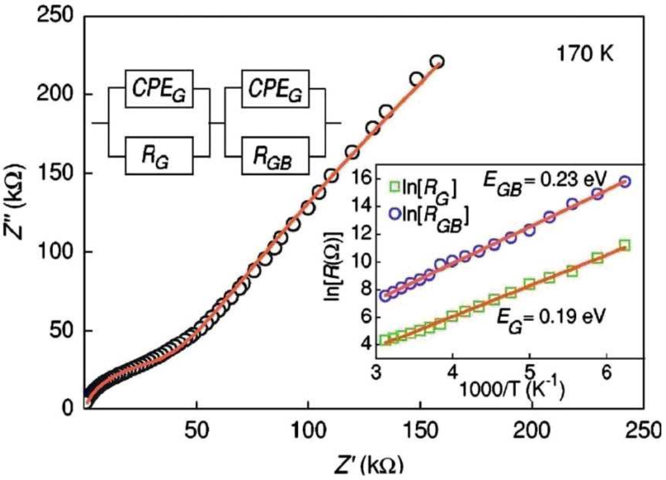

Figure 2.8 Impedance complex plane plots of polycrystalline CuO at 170 K (the equivalent circuit at 170 K is shown in the upper inset). The lower inset shows the Arrhenius plots of R_G and R_{GB} of the CuO sample (Sarkar et al., 2008a).

The study of impedance spectroscopy proves that there exists no phase transition in CuO material. Experimental data, simulated by an equivalent circuits, composed of two parallel RC elements connected in series, one representing semiconducting grains and the other insulating internal layers (as shown in inset of Figure 2.8). The complex impedance, Z^*, for this equivalent circuit could be easily obtained,

$$Z^* = \frac{R_g}{1 + i\omega C_g R_g} + \frac{R_{gb}}{1 + i\omega C_{gb} R_{gb}} \tag{2.1}$$

where R and C are respectively the resistance and capacitance, the subscripts g and gb refer to the grains and GB, respectively. Note that this model has been simplified by supposing that all of the grains and GB are uniformly distributed. In practice, the irregular distribution should be taken into consideration. Thus, Eq. (2.1) could be further modified as

$$Z^* = \frac{R_g}{1 + (i\omega C_g R_g)^\alpha} + \frac{R_{gb}}{1 + (i\omega C_{gb} R_{gb})^\gamma} \tag{2.2}$$

in which the parameters α and γ are used to express the relaxational time distributions.

The grain and GB responses can be identified by the impedance revealed in arcs. The plot for CuO ceramics at 170 K (as shown in Figure 2.8) has a large arc with a small arc at high frequencies. It is shown that the first component has a resistance of 28.34 kΩ with a comparatively lower capacitance. The second component, comparatively, has a resistance of 2.89 MΩ . Both R_G and R$_{GB}$ obtained from fitting Z^* plots obey the Arrhenius law (show in inset of Figure 2.9) provide the activation energies of the grain ($E_G = 0.19$ eV) and the grain boundary ($E_{GB} = 0.23$eV). Thus the impedance spectroscopy analysis (IS) clearly demonstrates that the grain boundaries are more resistive than grains in polycrystalline CuO. Therefore, the little difference between E_G and E_{GB} of CuO simply suggests that the composition of the GBs is slightly different from that of grains. This type of dissimilarity in composition between grains and grain boundaries of CuO arises due to the presence of minute about of Cu^{3+}. The scanning tunneling spectroscopy (STS) performed on grains and GBs regions shows that the concentration of Cu^{3+} is lesser in GBs than that in grains, and Schottky-type barrier might be present due to the space charge layer at GBs.

In general, the impedance spectroscopy (IS) analysis distinguishably proves much more conducting nature of the grains rather than GBs, primary criteria for becoming an internal barrier layer capacitance (IBLC). A small difference between activation energies of grains and GBs has also been observed, which suggests geometry as well as geometric structure of GBs are slightly different from those of grains. However, the IS technique itself is unable to provide information on the composition or electronic structure of the grains and GBs of CuO.

To support the earlier research Sarkar and co-worker (2008b) studied the origin of electrical heterogeneous microstructure in CuO from scanning tunneling spectroscopy. The result from the scanning electron microscopy shows that CuO ceramics exhibit uniform microstructures that grains are separated by discrete grain boundaries (GBs). Figure 2.9 shows grains (mark by the point X) and GBs (mark by the point Y) performed by scanning tunneling spectroscopy (STS). Figure 2.10 (a) shows the I-V plot measuring at point X in Figure 2.9. The value of the observed current for maximum applied STM tip bias voltage ($\sim$ 1.25 V) is about 100 nA. While the value of the observed current at position Y for a maximum applied bias voltage ($\sim$ 1.25 V) on the STM tip, is about 5 nA.

Figure 2.10 (b) shows the plot of the band profile at the point X of a

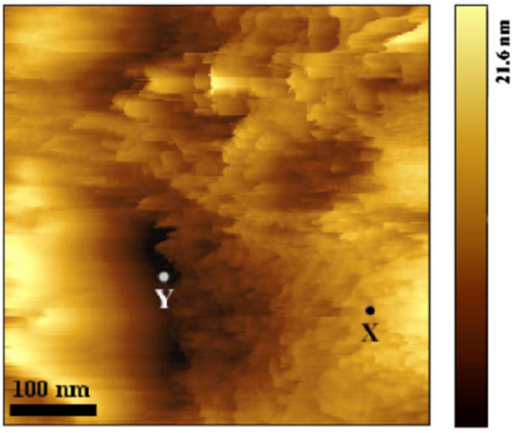

Figure 2.9 STM image of CuO sample showing GBs between the CuO grains. X and Y are the two points on grains and GBs, respectively (Sarkar et al., 2008b).

typical CuO grain. As can be seen in the Figure that the valence band (E_V) and conduction band (E_C) positions are clearly distinguished from local density of state (LDOS) spectra of the CuO grain. The LDOS profile on the grain reveal that the band gap of CuO is 1.32 eV. The zero value of the voltage corresponds to the E_F position in the CuO grain. The position of E_F on the LDOS profile confirms that the material is P-type.

The STS measurements directly exhibit that Cu^{3+} is mostly accumulated within the semiconducting grains, but the concentration of Cu^{3+} is negligible in insulating GBs. This type of electrically heterogeneous nature of CuO ceramics is, in turn, responsible for the formation of the barrier layer capacitance elements (BLCEs) in polycrystalline CuO.

Thongbai and his co-worker (2008a) reported the effects of grain, grain boundaries (GBs) and dc-bias electric field on giant dielectric in high purity CuO ceramics. The result of this study showed that the giant dielectric constant of $\sim (2.8 - 3.7) \times 10^4$ was observed in the high purity CuO (99.999%). It increases from $\sim 2.8 \times 10^4$ to $\sim 3.7 \times 10^4$ for the mean sizes of the CuO-1 and CuO-2

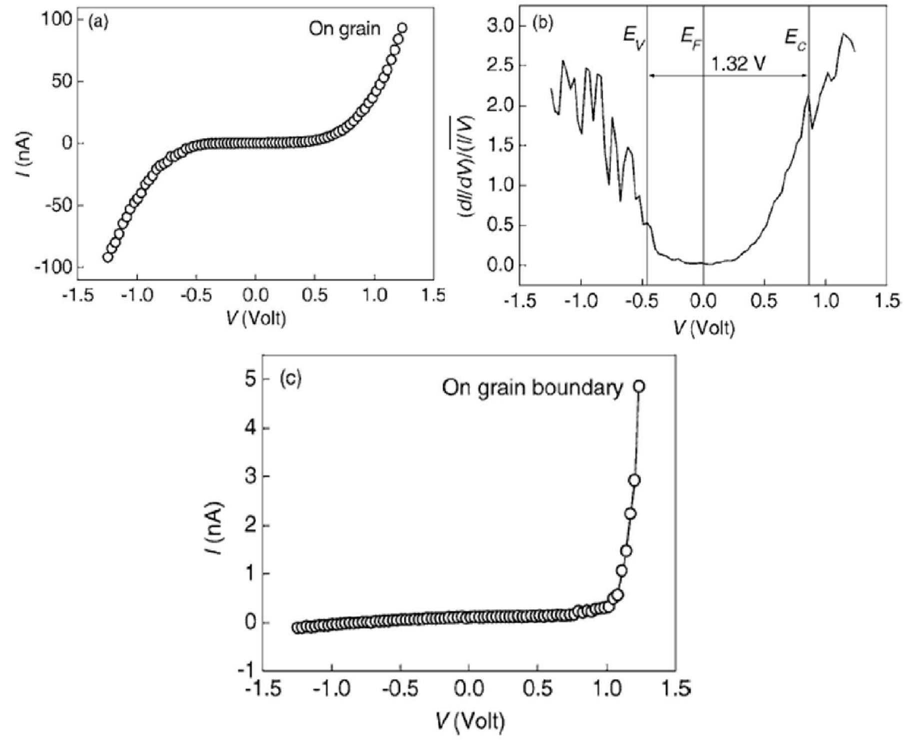

Figure 2.10 (a) Tunneling spectroscopic I-V characteristics on the CuO grain at point X (Figure 2.9) and (b) the [(dI/dV)/(I/V)-V] curve at point X, obtained from the $I - V$ data at that point. E_V, E_F, and E_C represent the positions of valance band, Fermi level, and conduction band, respectively. (c) Tunneling spectroscopic $I - V$ behavior on the GB of the CuO sample at point Y of Figure. 2.9 (Sarkar et al., 2008b).

grains increas from 4.75 ± 1.741 to 9.57 ± 3.01 μm. Figures 2.11 (a) and 2.11 (b) show the SEM micrographs of the CuO grains reported by Thongbai et al. They concluded that the giant dielectric respond in CuO ceramics is attributed to the internal barrier layer capacitance (IBLC) effect. According to the simple series model for the IBLC, the dielectric constant can simply be expressed as $\varepsilon' \approx \varepsilon_{\mathrm{gb}} d/t$, where $\varepsilon_{\mathrm{gb}}$ is the dielectric constant of the boundary layer, d is the grain size and t is the boundary layer thickness.

In addition, the activation energy (E_a) increases from 0.195 to 0.230 eV when the grain size increases from 4.57 ± 1.71 to 9.57 ± 3.01 μm. The increase in the Ea values with increasing grain size observed in this CuO samples may due

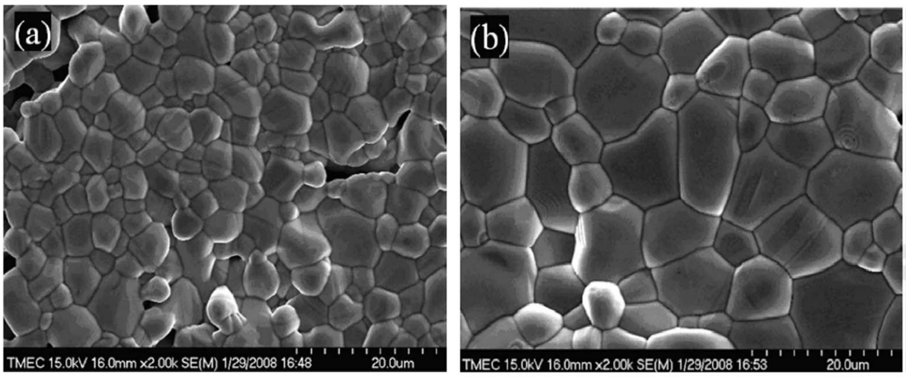

Figure 2.11 SEM micrograph of the CuO ceramics (a) CuO-1sintered at 920°C and (b) CuO-2 sintered at 980°C (Thongbai et al., 2008b).

perhaps to the domain boundaries (DBs) within the grain. DBs usually develop inside larger grains and influence mobility of charge carriers at different frequencies, i.e., the migration of charge carriers is restricted by DBs. The complex impedance (Z^*) plot containing a large semi circular arc at a low frequency corresponding to the resistance of GBs with the nonzero intercept on the Z' axis at a high frequency corresponding to grains. Figure 2.12 demonstrates the effect of dc-bias voltage. They found that the dielectric constant decrease with increasing the dc-bias voltage. While the resistance of GBs decreases, the resistance of grains remains constant.

Thongbai and his co-worker (Thongbai et al., 2008c) also reported the correlation between giant dielectric response and electrical conductivity of CuO ceramics. The dielectric dispersion was in good agreement with the Debye-like relaxation model at low temperature, but it deviated from the model at low frequencies as the temperature increased. High-ε' response in this CuO ceramic was attributed to the contributions of grain and GBs conductivity relaxations, respectively. The conductivity of GBs was found to increase with increasing dc bias.

Li and co-worker (Ming et al., 2009) studied the relaxer ferroelectric-like high effective permittivity in leaky dielectric/oxide semiconductor induced by elec-

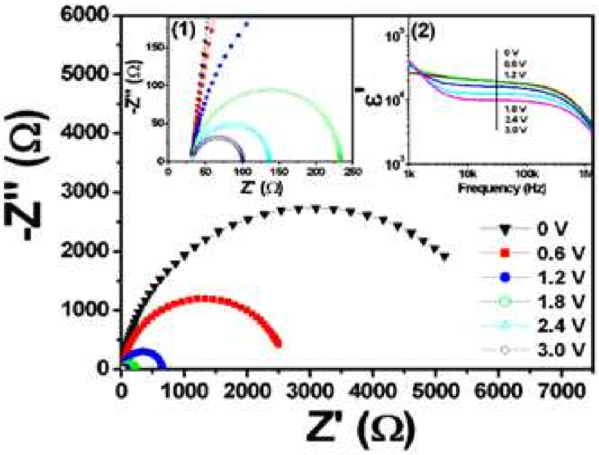

Figure 2.12 Impedance spectra as a function of dc bias for CuO-1 at room temperature: inset (1) displays the frequency dependent of the for CuO-1 under 0 - 3 V dc bias, and inset (2) shows and expended view of the high frequency data close to the origin (Thongbai et al., 2008b).

trode effect: A case study of CuO ceramics. In this study, the electrical behavior of copper oxide (CuO) ceramics sintered at 920°C was characterized by a combination of fixed, radio frequency (RF) capacitance measurements, and impedance spectroscopy (IS). Fixed RF capacitance measurements on ceramics with sputtered Au electrodes revealed a temperature- and frequency-dependent high effective permittivity of $\sim 10^4$ in the temperature range of 150 - 320 K. The response was similar to that observed for relaxor-ferroelectrics; however, the magnitude of the effect can be suppressed by thermal annealing of the ceramics with Au electrodes in air at 300°C or by changing the work function of the electrode material by using In-Ga as opposed to Au. IS data analysis revealed the ceramics to be electrically heterogeneous semiconductors with a room temperature dc resistivity ¡$10^4\Omega$·cm , consisting of semiconducting grains with relative permittivity, $\varepsilon_r < 10$ and slightly more resistive grain boundaries with “effective” permittivity, ε_{eff}, of ~ 110. Samples with Au electrodes exhibited an additional low frequency response with $\varepsilon_{eff} \sim 10^4$. A dc bias experiment showed the capacitance behavior of this additional response to obey the Mott-Schottky law and thus confirming it to be a non-Ohmic electrode contact. They concluded that an electrode rather than a grain boundary effect was the primary source for the high effective permittivity in CuO ceramics, although the latter was also present and did give additional effective permittivity. Their work demonstrated how an extrinsic effect associated with non-Ohmic electrode contacts can; (i) dominate the RF capacitance spectra of leaky dielectrics/oxide semiconductors over a wide temperature and frequency range; and, (ii) manifest a dielectric response more typically associated with relaxor-ferroelectrics.

2.3 Effect of uniaxial compressive stress on the giant dielectrics

Thongbai and his co-worker (Thongbai et al., 2007) studied the giant dielectric behavior of $CaCu_3Ti_4O_{12}$ ceramics subjected to post-sintering annealing and uniaxial stress. The $CaCu_3Ti_4O_{12}$ ceramics were sintered at 1100°C for 6 and 16 h in air and these subject to post-sintering annealing in argon. They found that the pre-sintered ceramic at 1100°C for 6 h (CCTO-6) exhibit lower dielectric constant (ε') than the pre-sintered ceramic at 100°C for 16 h (CCTO-16) by one order of magnitude. The dielectric behavior of both samples exhibit Debye-like relaxation, and can be explained based on Maxwell-Wagner model. The Debye-like relaxation and dielectric loss tangent ($\tan\delta$) for both samples are shown in Figure 2.13 a and b, respectively.

The ceramics post-sintering annealing in argon for 5 h leads to a significant increase in ε' for the CCTO-16 but a slightly decrease for CCTO-6. The dielectric constant, ε', of CCTO-16 ceramics after annealing in argon increase with increasing temperatures, and exhibits a peak at about -50°C (Figure 2.13), which is closely

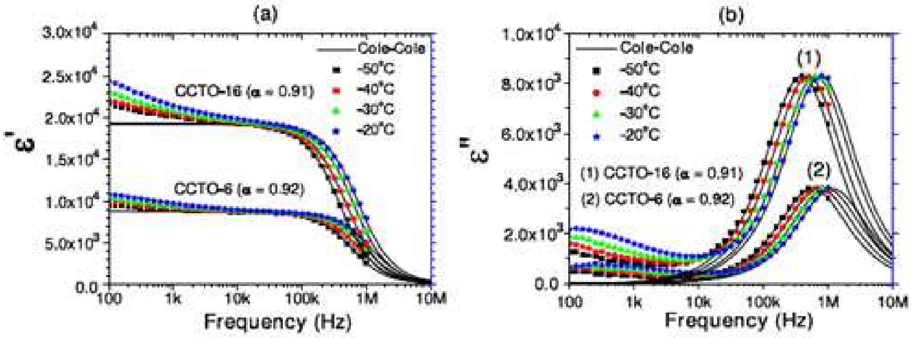

Figure 2.13 (a) Frequency dependence of the dielectric dispersion showing at several temperatures for the sintered materials of CCTO-6 and CCTO-16. (b) Frequency dependence of the dielectric dispersion showing at several temperatures for the sintered materials of CCTO-6 and CCTO-16 (Thongbai et al., 2007).

related to the oxygen vacancies.

They found also that the dielectric properties of the argon-annealed samples change significantly with the applied compressive stress the absolute change can reach 25% at maximum stress of 130 MPa, see in the Figure 2.14 (a) and (b).

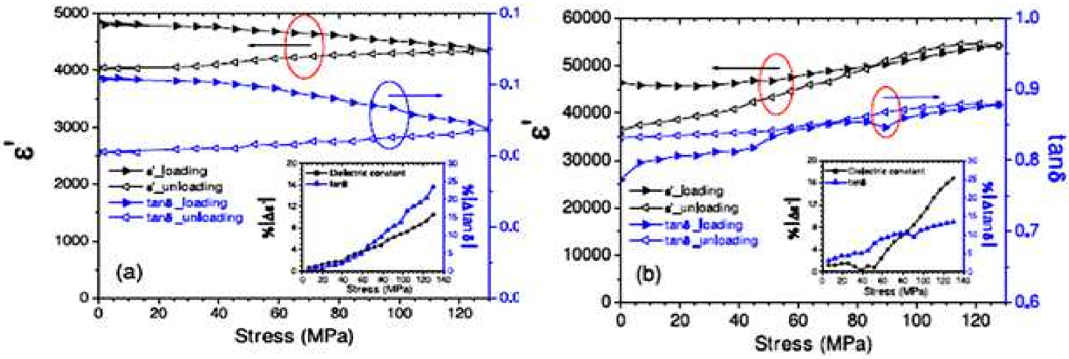

(a) (b)

Figure 2.14 Uniaxial stress dependent of ε' and $\tan\delta$ at a frequency of 100 Hz for the samples of (a) CCTO-6 and (b) CCTO-16 after annealing at 1000°C for 5 h under flowing argon (Thongbai et al., 2007).

Figure 2.14 (a) shows the dielectric constant (ε') and $\tan\delta$ decrease with increasing stress for the CCTO-6-Ar ceramic, and, interestingly, continue to decrease upon the reduction of applied stress. On the other hand, the dielectric properties of CCTO-16-Ar ceramic increase when the stress is increased and decreased when the stress gradually reduced, as shown in Figure 2.14 (b). They show that very high dielectric constant observed in CCTO ceramics is attributable to highly resistive grain boundaries. As mentioned that the CCTO-16-Ar ceramic, which has been subjected to longer sintering (16 h), possessed one order of magnitude higher dielectric constant, possibly due to higher concentration of the acceptor state (oxygen vacancies) available in the grain boundaries of the ceramic. With lower concentrations of acceptor states, the CCTO-6-Ar should contain more mobile dipoles that can easily be activated by the applied stress. Hence, this leads to a stress-induced ageing mechanism, as reported previously by Yimnirun and co-workers (Yimnirun, 2006; Yimnirun et al., 2006a; Yimnirun et al., 2006c), that results in the decrease in the dielectric constant and dielectric loss. This stress-induced ageing is irreversible, as the dielectric properties continue to decrease even upon reduction of the applied stress (Figure 14 (a)). On the other hand, in the case of the CCTO-16-Ar ceramic, with higher concentration of the acceptor states, there are competing mechanisms between the stress-induced ageing and the elastic deformation Initially, with the stress-induced ageing mechanism still dominating, most of the acceptor states come to rest at the grain boundaries and stabilize the stress influence, as it was observed that the dielectric properties were rather stable at lower stress level. A further increase in the compressive stress may result in a slight decrease in the grain boundary thickness. The effective dielectric properties of this ceramic, which can be regarded as the boundary layer capacitor (BLC), therefore increase, and the decrease in the effective dielectric properties follows with the reduction of the stress, as observed in Figure 2.14 (b).

CHAPTER III

DIELECTRIC PROPERTIES OF MATERIALS

This chapter provides theoretical background for electrical properties related to CuO materials including theories relating macroscopic measurements to microscopic quantities, sources of polarizability, dielectric relaxation, dielectric behaviors in alternating fields and theory of impedance spectroscopy.

3.1 Theories relating macroscopic measurements to microscopic quantities (Von Hippel, 1954)

The electrical engineer is most concerned with dielectric materials in relation to capacitor in an electrical circuit. The principal characteristic of a capacitor is that an electrical charge, Q , can be stored. The charge on a capacitor is

$$Q = CV \tag{3.1}$$

where V is the applied voltage and C is the capacitance. The voltage is directly proportional to the amount of charge stored and the current passing though the capacitor is given by

$$V = \frac{Q}{C} = \frac{\int I dt}{C} \Rightarrow I = C\frac{dV}{dt}. \tag{3.2}$$

The capacitance, C , contains both a geometrical and a material factor. For a large plate capacitor of area, A , and thickness, d , the geometrical capacitance in vacuum is given by

$$C_0 = \frac{A}{d}\varepsilon_0, \tag{3.3}$$

where ε_0 is the permittivity or dielectric constant of a vacuum. If a ceramic material of dielectric constant, ε , is inserted between the capacitor plates,

$$C = C_0\frac{\varepsilon}{\varepsilon_0} = C_0\varepsilon', \tag{3.4}$$

where ε' is the relative permittivity or relative dielectric constant. This is the material property determining the capacitance of a circuit element and is of principal concern to the ceramist.

A dielectric material reacts to an electric field differently from a free space because it contains charge carriers that can be displace and charge displacement within the dielectric can neutralize a part of the applied field. From Eq. (3.1) and (3.4), we can write for a capacitor containing a dielectric

$$V = \frac{Q/\varepsilon'}{C_0}. \tag{3.5}$$

That is, only a fraction of the total charge, the free charge, Q/ε' , set up an electric field and voltage toward the outside; the remainder, the bound charge, is neutralized by polarization of the dielectric. We can schematically represent (Figure 3.1) the total electric flux density, $\vec{D}$, as the sum of the electric field, $\vec{E}$, and dipole charge,$\vec{P}$:

$$\vec{D} = \varepsilon_0\vec{E} + \vec{P} = \varepsilon\vec{E}. \tag{3.6}$$

Where the polarization is the surface charge density of the bound charge, equal to the dipole moment per unit volume of material:

$$\vec{P} = N\vec{\mu} \tag{3.7}$$

where N is the number of dipoles per unit volume and $\vec{\mu}$ is the average dipole moment. The electric dipole moment corresponds to two electric charges of opposite polarity, $\pm Q$, separated by the distance, $\vec{d}$:

$$\vec{\mu} = Q\vec{d}. \tag{3.8}$$

Thus polarization can equivalently designate either the bound charge density or the dipole moment per unit volume. From Eq. (3.6),

$$\vec{P} = \varepsilon\vec{E} - \varepsilon_0\vec{E} = \varepsilon_0(\varepsilon' - 1)\vec{E}. \tag{3.9}$$

Another measure of the ratio of polarization to applied field is the electric susceptibility:

$$\chi = \varepsilon' - 1 = \frac{\left|\vec{P}\right|}{\varepsilon_0\left|\vec{E}\right|}. \tag{3.10}$$

The susceptibility is the ratio of the bound charge density to the free charge density.

The average dipole moment, $\langle\vec{\mu}\rangle$, of the elementary particle is proportional to the local electric field, $\vec{E}_L$, which acts on the particle:

$$\langle\vec{\mu}\rangle = \alpha\vec{E}_L. \tag{3.11}$$

The proportionality factor, α, the polarizability, is a measure of the average dipole

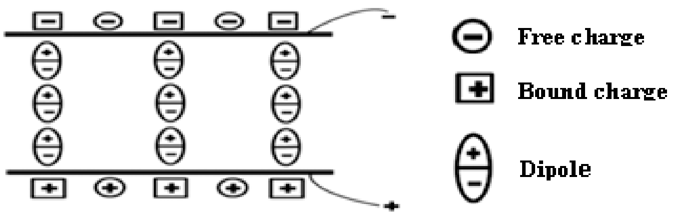

Figure 3.1 Schematic representation of polarization by dipole chains and bound charge (Von Hippel, 1954).

moment per unit of local field strength. An alternate expression for the polarization then is

$$\vec{P} = N\alpha\vec{E}_L. \tag{3.12}$$

In condensed phases, there are always strong interactions between dipoles. A simple and valuable approach is to consider a point dipole as contained in an empty sphere, which is surrounded by bulk material (see Figure 3.2). The idea is to isolate a single dipole, and to distribute charges around the cavity such that the bulk field lines are not affected by the presence of the cavity.

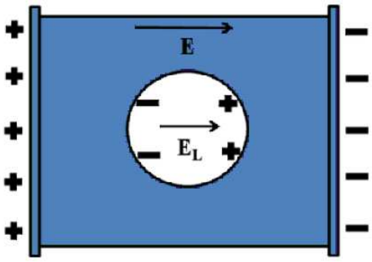

Figure 3.2 Cavity model used to construct physical representation of a single dipole moving with an electric field. The cavity and distribution of charges on the inside of the cavity, which neutralize the dipole, are constructed such that the bulk electric field lines are unaffected by the presence of the cavity (Blythe, 1979).

The local field is a sum of the field due to charges on the electrodes and the field from the sample outside the cavity ($\vec{E}_L = \vec{E}_C + \vec{E}_P$). After integrating the fields around the cavity and adding the electrode field $\vec{E} + \vec{P}/\varepsilon_0$, where $\vec{E}$ is the external field, $\vec{E}_L = \vec{E} + \frac{\vec{P}}{3\varepsilon_0}$. From Eq. 3.12 the Clausius-Mossotti (Lorentz) relation emerges

$$\frac{N\alpha}{3\varepsilon_0} = \frac{\varepsilon' - 1}{\varepsilon' + 2}. \tag{3.13}$$

This relates the dielectric constant to the electronic polarizability.

3.2 Sources of polarizability

Basically, polarizability is a consequence of the fact that the molecules, which are the building blocks of all substances, are composed of both positive charges (nuclei) and negative charges (electrons). When a field acts on a molecule, the positive charges are displaced along the field, while the negative charges are displaced in a direction opposite to that of the field. The effect is therefore to pull the opposite charge apart, i.e., to polarize the molecule. There are different types of polarization processes, depending on the structure of molecules which constitute the solid.

There are various possible mechanisms for polarization in a dielectric material. One process common to all materials is electron polarization (Figure 3.3 (a)), or the shift of the center of gravity of the negative electron cloud in relation to the positive atom nucleus in an electric field. A second mechanism is the displacement of positive and negative ions in relation to one another, called ionic or atomic polarization (Figure 3.3(b)). A third kind of polarization, uncommon in ceramics, is associated with the presence of permanent electric dipoles which exist even in the absence of an electric field. An unequal charge distribution between partners in a molecule or complex ion is not uncommon; when a field is applied, these tend

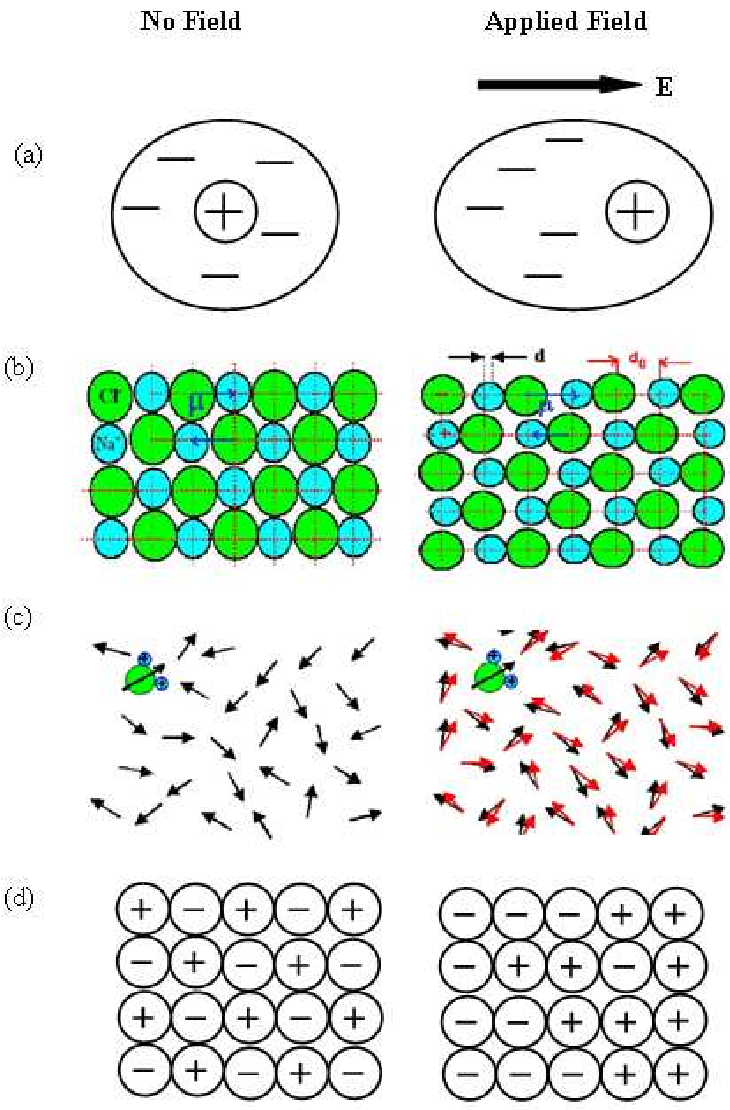

Figure 3.3 Schematic representation of different mechanisms of polarization: (a) electronic polarization, (b) atomic or ionic polarization, (c) orientation or dipolar polarization and (d) space charge polarization (Von Hippel, 1954).

to line up with the electric dipoles in the direction of the field, giving rise to an orientation polarization (Figure 3.3 (c)). A final source of polarization is mobile charges which are present because they are impeded by interfaces, because they are trapped in the material. Space charges resulting from these phenomena appear as an increase in capacitance as far as the exterior circuit is concerned (Figure 3.3 (d)).

In general, therefore, the total polarizability of the dielectric can be represented as the sum of these:

$$\alpha = \alpha_e + \alpha_i + \alpha_d + \alpha_s, \tag{3.14}$$

where α_e is the electronic, α_i the ionic, α_d the orientation or dipolar and α_s the space charge polarizability.

The typical dependence of the polarizability on frequency over a wide range is shown in Figure 3.4. In the range from $10^0 - 10^3$ Hz is the radio wave section of the spectrum, the interfacial or space charge polarizability responses. It can be seen that in the range from $10^3 - 10^7$ Hz, some frequency usually in the microwave region, the polarizability is essentially constant. In the neighborhood of this frequency range, however, the polarizability decreases by a substantial amount. This amount corresponds precisely, in fact, to the dipolar contribution, α_d. The reason for the disappearance of α_d in the frequency range $\omega > \omega_d$ is that the field now oscillates too rapidly for the dipole to follow, and so the dipoles remain essentially stationary. The polarizability remains similarly unchanged in the frequency range from $\omega_d - \omega_i$ and then drops down at the higher frequency. The frequency ω_i lies in the infrared region, and corresponds to the frequency of the transverse optical phonon in the crystal. For the frequency range $\omega > \omega_i$ the ions with their heavy masses are no longer able to follow the very rapidly oscillating field, and consequently the ionic polarizibility, α_i, vanishes. Thus in the frequency range above the infrared, only the electronic polarizability remains effective, because the electrons, being very light, are still able to follow the field even at the high frequency. This range includes both the visible and ultraviolet regions. At still higher frequencies (above the electronic frequency, ω_e) however, the electronic contribution vanishes because even the electrons are too heavy to follow the field with its very rapid oscillations. The frequencies ω_d and ω_i, characterizing the dipolar and ionic polarizabilities, respectively, depend on the substance considered, and vary from one substance to another. However, their orders of magnitude remain in the regions indicated above, i.e., in the microwave and infrared, respectively. The various polarizabilities may thus be determined by measuring the substance at various appropriate frequencies.

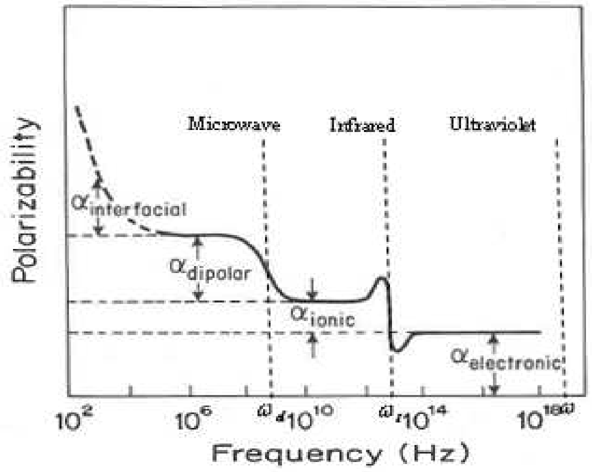

Figure 3.4 Frequency dependence of several contributions to the polarizability (Lasaga and Cygan, 1982).

3.3 Dielectric relaxation

It is important to clarify the meaning of relaxation. Time and temperature are linked: higher frequencies correspond to shorter times for the response of a material to a stimulus, which is also equivalent to lowering the temperature. Every dipolar motion will have a particular point below or above which it freezes out; i.e., at sufficiently low temperature or high frequency, thermally-activated motions cannot overcome steric barriers (Figure 3.5). At the transition from the mobile to the immobile state, the simplest representation assumes that change in polarization is proportional to the current value. The corresponding correlation function decays exponentially in time ($e^{-t/\tau}$) and results in a broad peak in the frequency-dependent energy loss (Schonhals and Kremer, 2003).

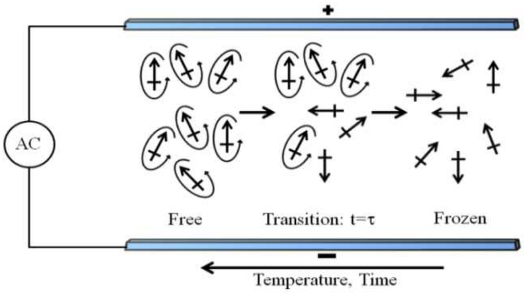

Figure 3.5 Schematic illustration of the dipolar transition from a mobile to immobile state under an ac field. At high temperatures and long switching times of the field, dipoles are free to move with the field. As the temperature decreases or the switching time decreases, the ions no longer have sufficient energy to remain in phase with the field. At some intermediate time, the time constant of the process is equal to the switching time and the correlation function is maximized (Klein, 2007).

In dielectric spectrum, this transition-related peak is termed a relaxation. Most real relaxations are broadened more than predicted by this simple, but the behavior is still dominated by the characteristic correlation function and relaxation time.

An ideal relaxation is illustrated in a combined plot of ε' and ε'' (see Figure 3.6). These two quantities represent the real and imaginary parts of the dielectric constant, respectively. (The terms dielectric constant and dielectric permittivity are interchangeable). They also constitute the in-phase and out-of phase components of the complex dielectric constant ε^* :

$$\varepsilon^* = \varepsilon' - i\varepsilon'', \tag{3.15}$$

where $i = \sqrt{-1}$. At temperatures above and frequencies below the freezing point, the real part of the dielectric constant, ε', is larger because of the ability of the dipoles to respond to the applied field.

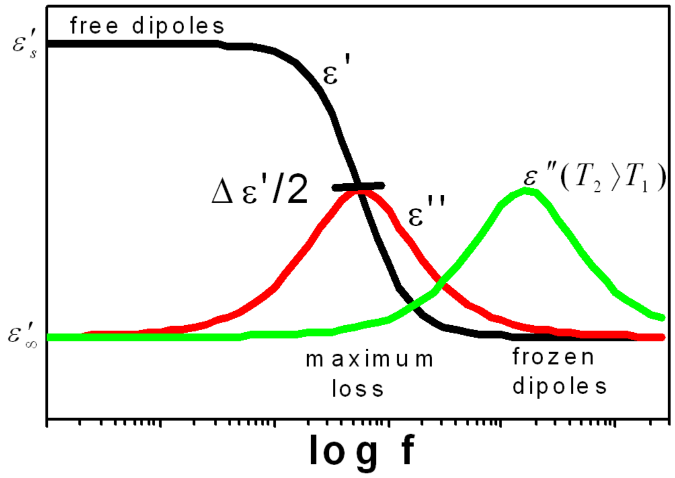

Figure 3.6 Appearance of ε' and ε'' for a Debye relaxation. ε'_s is the low-frequency, or relaxed, dielectric constant, and ε'_∞ is the high-frequency, or unrelaxed, dielectric constant. The value of ε'' at its maximum is half the relaxation strength. The dotted curve indicates the shift in the dielectric loss due to increased temperature (Moulson and Herbert, 2003).

3.4 The dielectric behavior in alternating fields

In the solid state, dipolar alignment can take considerable time and hence the polarization takes time to develop when a static field is applied. If an alternating field is applied then the polarization may fully develop at sufficiently low applied frequencies but if the frequency of the applied field is too high then the field is reversed before the polarization has responded and the net effect is no response. The magnitude of the polarization thus drops off as the frequency is increased. The phase of the response also changes. At low frequencies the polarization and the field are in phase but at high frequencies the polarization lags by 90°C . This characteristic drop off in response is known as a relaxation.

To capture both the magnitude and phase of the response a complex relative dielectric constant, ε^*, can be defined:

$$\varepsilon^* = \varepsilon' - i\varepsilon'', \tag{3.16}$$

where $i = \sqrt{-1}$, ε' is the real part of the relative dielectric constant which expresses the maximum stored electrical energy and ε'' is the imaginary part of the relative dielectric constant, commonly known as the dielectric loss, which represents the energy dissipated per cycle (in the form of heat). Both ε' and ε'' are experimentally measurable quantities which may be used to characterize the dielectric dispersion over a range of frequencies and temperatures.

The ratio $\varepsilon''/\varepsilon'$, is known as the dielectric loss tangent or dissipation factor and is expressed as:

$$\tan\delta = \frac{\varepsilon''}{\varepsilon'}, \tag{3.17}$$

where 90-δ is the phase angle between current and voltage.

Experimentally, in order to measure the permittivity of a ceramic sample, the alternating voltage given by the real part of $V = V_0 e^{i\omega t}$ (where V_0 is the amplitude, ω is the angular frequency and t is the time) is applied across the ceramic sample which is sandwiched between two electrodes (as shown in Figure 3.7) at a temperature T. The measured current is the real part of a complex current, I^*, given by:

$$I^* = C^* \frac{d\mathrm{V}}{dt} = \varepsilon^* C_o \frac{d\mathrm{V}}{dt} = i\omega\varepsilon^* C_o \mathrm{V} \tag{3.18}$$

where C^* is the complex capacitance of the sample and C_0 is the vacuum capacitance between the two electrodes (the distance between two electrodes is equal to the thickness of the sample, d_s). Inserting Eq. (3.16) into Equation (3.18) gives

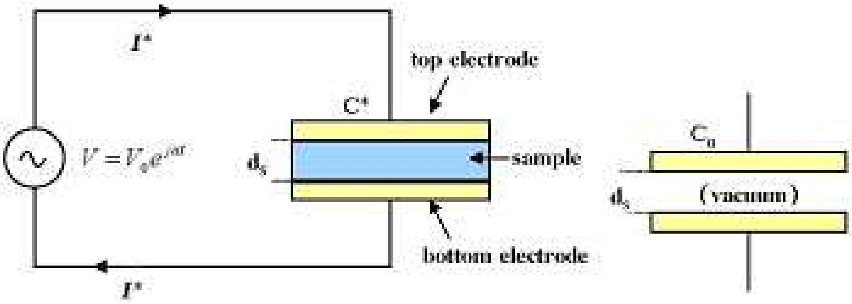

Figure 3.7 A circuit diagram of dielectric measurement (Moulson and Herbert, 2003).

$$I^* = \omega C_o(\varepsilon'' + i\varepsilon')\mathrm{V}. \tag{3.19}$$

The dielectric sample can be considered as an equivalent parallel circuit (Von Hippel, 1954) as shown in Figure 3.8. The admittance, Y^*, (reciprocal of the impedance) of this circuit can be expressed as:

$$Y^* = \frac{1}{R_p} + i\omega C_p, \tag{3.20}$$

where R_p and C_p are the parallel resistance and capacitance of ceramic dielectric respectively. The current, I^*, passing through the circuit can be represented as:

$$I^* = VY^* = (\frac{1}{R_p} + i\omega C_p)\mathrm{V} = I_R + iI_C, \tag{3.21}$$

where I_p and I_C is the real and imaginary part of the current, I^*, respectively. Equating Eq. (3.19) and (3.21) yields:

$$(\omega C_o\varepsilon'' + i\omega C_o\varepsilon')V = (\frac{1}{R_p} + i\omega C_p)V = I_R + iI_C. \tag{3.22}$$

From Eq. (3.22) ε' and ε'' can, then, be calculated as follows:

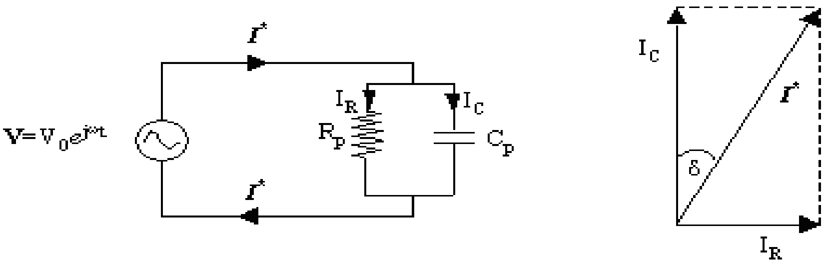

(a) (b)

Figure 3.8 The equivalent parallel circuit of a dielectric ceramics (a) and corresponding phase diagram (b). (R_P and C_P are the parallel resistance and capacitance of polymer dielectric respectively (Von Hippel, 1954).

$$\varepsilon' = \frac{I_C}{\omega C_o V} = \frac{C_p}{C_o}, \tag{3.23}$$

$$\varepsilon'' = \frac{I_R}{\omega C_o V} = \frac{1}{\omega C_o R_p}, \tag{3.24}$$

and

$$\tan\delta = \frac{\varepsilon''}{\varepsilon'} = \frac{I_R}{I_C}. \tag{3.25}$$

Eq. (3.24) can be rewritten as:

$$\varepsilon'' = \frac{1}{\omega C_o R_p} = \frac{G_p}{\omega C_o}, \tag{3.26}$$

where $G_p = \frac{1}{R_p}$ is the *AC* conductance, which in general is a combination of genuine conductivity (i.e. the motion of charges) and the conductance due to any time dependent polarization processes (i.e. the motion of dipoles). If the electrode plates have area A and separation, d_s (sample thickness), G_p and C_0 can be presented as:

$$G_p = \frac{\sigma A}{d_S}, \tag{3.27}$$

and

$$C_o = \frac{\varepsilon_o A}{d_S}, \tag{3.28}$$

hence,

$$\varepsilon'' = \frac{\sigma}{\varepsilon_o \omega}, \tag{3.29}$$

where σ is the conductivity. In general, σ will include both the time dependent polarization effects and genuine conduction (σ_{dc}) arising from free charges, and is assumed to be frequency independent at these low frequencies.

3.5 Theory of impedance spectroscopy

AC impedance spectroscopy (Sinclair and West, 1989) is a powerful technique that gives information on the electrical properties of polycrystalline materials over a wide range of frequency. Not only electrode capacitance but also grain, grain boundary and domain boundary resistances and capacitances can be obtained by this method. The complex plane method is frequently used to analyze impedance data. In the complex plane, Z^*, method, imaginary part (Z'': capacitive) of the impedance is plotted against the real part (Z': resistive). To extract resistances and capacitances of the sample, an equivalent circuit is used to model the electrical response. For example, in case of CCTO three parallel resistor-capacitor,RC, elements in series were used to describe the contributions from grain, grain boundary and domain regions.

The detailed data processing is illustrated by two examples (West, 1989). The relationship between the current, I, and the resistor, R, under an applied voltage, V, is defined by Ohm's Law:

$$I = \frac{V}{R}. \tag{3.30}$$

A pure capacitor allows the passage of a frequency dependent AC current given by,

$$I = i\omega CV, \tag{3.31}$$

where ω is the angular frequency ($= 2\pi f$, with the applied frequency, f, in Hz) and $i = \sqrt{-1}$. These equations can be expressed in terms of the impedance, Z,

$$I = \frac{V}{Z}. \tag{3.32}$$

Example I. If a resistance and capacitance were combined in series as shown in Figure 3.9 (a), the total voltage drop, V, and the total impedance, Z, will be expressed as,

$$V = V_1 + V_2 = IR + \frac{I}{i\omega C} = I\left(R + \frac{1}{i\omega C}\right), \tag{3.33}$$

$$Z = R + \frac{1}{i\omega C} = R - \frac{i}{\omega C}. \tag{3.34}$$

This impedance equation contains the real and imaginary parts. Therefore, the complex impedance, Z^*, is given by,

$$Z^* = Z' - iZ'', \tag{3.35}$$

$$Z' = R,\ Z'' = \frac{1}{\omega C}. \tag{3.36}$$

Example II. When the R and C are arranged in parallel in the circuit (Figure 3.9 (b)), the reciprocal complex impedance can be used for analysis.

$$A^* = \frac{1}{Z^*} = \frac{1}{R} + i\omega C, \tag{3.37}$$

where A^* is the complex admittance. Therefore the following equations are derived.

$$A^* = A' + iA'' \tag{3.38}$$

$$A' = \frac{1}{R},\ A'' = \omega C \tag{3.39}$$

The complex impedance can be determined by the complex admittance,

$$\begin{aligned} Z^* &= \frac{1}{A^*} = \left(\frac{1}{R} + i\omega C\right)^{-1} = \frac{R}{1 + i\omega RC} \\ &= \frac{R(1 - i\omega RC)}{(1 + i\omega RC)(1 - i\omega RC)} = \frac{R - Ri\omega RC}{1 + (\omega RC)^2} \\ &= \frac{R}{1 + (\omega RC)^2} - R\frac{i\omega RC}{1 + (\omega RC)^2}. \end{aligned} \tag{3.40}$$

Therefore,

$$Z' = \frac{R}{1 + (\omega RC)^2} \text{ and } \mathrm{Z}'' = \mathrm{R}\frac{\omega \mathrm{RC}}{1 + (\omega \mathrm{RC})^2}. \tag{3.41}$$

In summary, the impedance data can be described by three different complex formalisms: the complex impedance, Z^*, the complex admittance, A^*, and

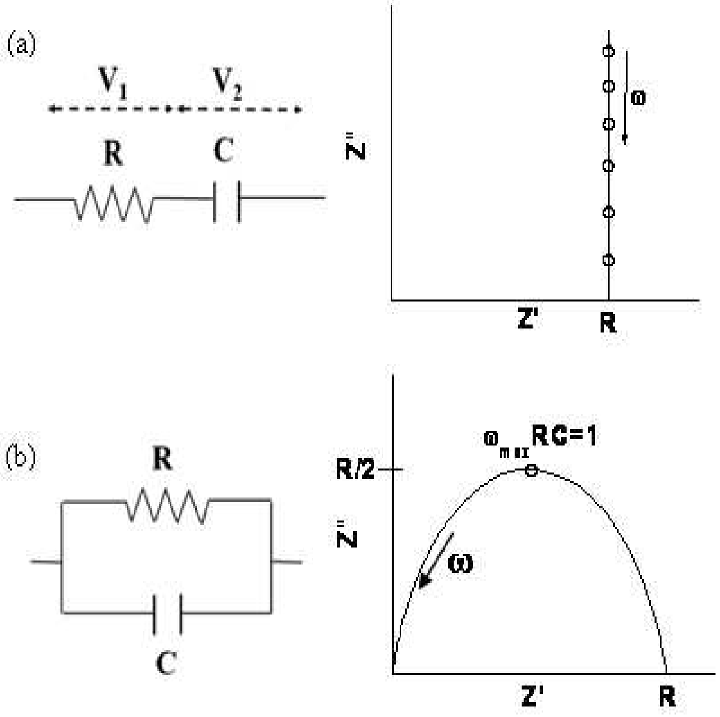

Figure 3.9 An illustration of the simplest combinations of a resistor and capacitor, along with the impedance behavior shown to the right of the electrical analog. R and C are the magnitudes of the resistor's resistance and capacitor's capacitance, respectively. (a) Series combination and (b) parallel combination of resistance and capacitance. The lines in the impedance plots are derived from the locus of points evaluated at different radial frequencies, ω (Bruce, 1987).

complex permittivity, ε^* as follows (West, 1989). i.Complex impedance:

$$Z^* = R_s - \frac{i}{\omega C_s} \tag{3.42}$$

(s = series)

ii.Complex admittance:

$$A^*(or\ Y^*) = (Z^*)^{-1} = \frac{1}{R_p} + i\omega C_p \tag{3.43}$$

(p = parallel)

iii.Complex permittivity:

$$\varepsilon^* = \frac{A^*}{i\omega\varepsilon_0} = \varepsilon' - i\varepsilon'' \tag{3.44}$$

This chapter provides theoretical background for electrical properties related to CuO materials including theories relating macroscopic measurements to microscopic quantities, sources of polarizability, dielectric relaxation, dielectric behaviors in alternating fields, and theory of impedance spectroscopy.

CHAPTER IV

EXPERIMENTAL DETIALS

This chapter is concerned with the experimental details carrying out in this work. Two novel methods for synthesizing copper oxide (CuO) powder are introduced. The synthesized powders together with a commercial CuO powder are used to prepare CuO ceramic samples. Finally, characterization methods and details of the dielectric measurements of the CuO ceramic samples are explained.

4.1 Preparation of CuO powder

Apart from the commercial powders obtained from the Aldrich Co. Ltd., with 99.99% purity, we were successfully synthesized CuO powders using two simple methods namely direct thermal decomposition method (DT method) and polymer pyrolysis solution method (PR method).

4.1.1 Direct thermal decomposition method

The starting material for this method is $Cu(CH_3COO)_2.H_2O$ powder. The powder was put into an alumina crucible and then calcined separately at different temperatures of 500, 600 and 700°C in air for 6 h. The calcined powder was then ball milled ($\sim$ 80 rpm) in a sealed alumina vial using zirconia balls under ambient condition for 5 h. The final product obtained was black crystalline powder.

4.1.2 Polymer Pyrolysis solution method

The chemical reagents used in this method are copper nitrate ($Cu(NH_3)_2$ $.3H_2O$), ammonium per sulfate ($(NH_4)_2S_2O_4$) and acrylic acid. The experimental procedure started by dissolving copper nitrate 241.6 g in 300 g acrylic acid aqueous solution (Acrylic:H_2O = 70:30 wt%) under stirring. The molar fraction of nitrate:solution was fixed at 1:2; then a small amount (about 0.5 g) of 5% $(NH_4)_2S_2O_4$ aqueous solution was added to the mixed acrylic acid solution to promote the polymerization. Under heating at 60 - 70°C for 5 h the mixed solution was dried at 100°C for 24 h to form the well-distributed polyacrylate salt. The polyacrylate salt was then ball milled ($\sim$ 80 rpm) in the sealed alumina vial using zirconia balls under ambient condition for 5 h. Finally, the powder was calcined at 500, 600 and 700°C for 6 h in air. The final product obtained was black crystalline powder.

4.2 Preparation of CuO ceramic

For preparation of the CuO ceramic samples, the commercial and the synthesized CuO powders were separately pressed at 150 MPa into pellets of 15 mm in diameter and about 1 to 2 mm thick using a uniaxial pressing machine. Finally, these pellets were sintered at 900 and 950°C for 10 h in air in a box furnace with the heating and cooling rates of 5°C/min.

4.3 Samples annealing

The obtained CuO ceramic samples were then annealed in an atmosphere of flowing argon gas (99.995% purity) at 700°C for 2 h and some of the samples were then re-annealing in the atmosphere of flowing oxygen gas at 700°C for 2 h.

The flowing rate of the gases was about 5 lit./min.

4.4 Samples characterization

The $Cu(CH_3COO)_2.H_2O$ powder and the dried powder precursors prepared as solution method were characterized by TG-DTA (Pyris Diamond TG/DTA, Perkin Elmer Instrument, USA). This technique was used to determine the decomposition and crystallization temperatures (or phase changes) of the powder. The analyses were performed with a heating rate of 15°C/min in static air up to 1000°C. The phase of the CuO powders and ceramics was characterized by X-ray diffraction (XRD) (PW3040 Philips X-Pert MPD Multi Purpose CuKα radiation with $\lambda = 0.15406$ nm). The results of the X-ray diffraction were also used to estimate of the crystallite size of the CuO powder. From the line broadening of corresponding X-ray diffraction peaks, the crystallite size (D) was estimated using the Scherrer formula (Cullity and Stock, 2001):$D = \frac{K\lambda}{\beta \cos\theta}$, where λ is the wavelength of the X-ray radiation, K is a constant taken as 0.75, θ is the diffraction angle. β is the full width at half maximum ($FWHM$) and is given by $\beta = \sqrt{\beta_0^2 - \beta_i^2}$, where β_0 and β_i are the widths from the observed X-ray peaks and the width due to instrumental effects respectively.

The microstructures of the CuO ceramics were characterized using a scanning electron microscopy or SEM (LEO SEM 1450VP, UK). The grain size of each CuO ceramic sample was measured using a standard line intercept technique from the SEM micrographs of the CuO ceramic surface. Average grain size was obtained by measuring at least 200 intercepts for each micrograph.

Throughout this work, symbols were assigned for the CuO ceramic samples obtained from each stage of the preparations beginning with the sintered CuO ceramics fabricated from commercial and the three CuO powders calcined at 500, 600 and 700°C following by the annealing under the flowing argon and then re-annealing in the flowing oxygen as summarized in Table 4.1.

Table 4.1 Symbols for the CuO ceramics fabricated using the CuO powder prepared from different methods. Methods Symbols Detail of samples.

Methods	Symbols	Detail of samples
Commercial CuO powder with 99.99% purity	as-CuO-99.99a	The CuO sintered at 900°C in air for 10 h
	as-CuO-99.99b	The CuO sintered at 950°C in air for 10 h
	Ar-CuO-99.99a	The CuO-99.99a annealing under flowing argon at 700°C for 2 h
	Ar-CuO-99.99b	The CuO-99.99b annealing under flowing argon at 700°C for 2 h
	O_2-CuO-99.99a	The Ar-CuO-99.99a annealing under flowing oxygen at 700°C for 2 h
	O_2-CuO-99.99b	The Ar-CuO-99.99b annealing under flowing oxygen at 700°C for 2 h

4.5 Dielectric property measurement

The dielectric properties of the sintered CuO ceramic samples before and after the annealing were measured. These properties are important in considering for the practical application of high dielectric materials. The dielectric response (capacitance, C_p, and loss tangent, $\tan\delta$) of the as-sintered ceramics, the ceramics after annealing in argon and the ceramics after re-annealing in oxygen were measured using a Hewlett Packard 4194A Impedance Gain Phase Analyzer over a frequency range from 100 Hz to 1 MHz and at an oscillation voltage of 1 V. Silver paint was coated on both surfaces of the samples and learn these to dry over night. The measurements were performed in the temperature range from -50°C to 130°C

Table 4.1 Symbols for the CuO ceramics fabricated using the CuO powder prepared from different methods (Continue).

Methods	Symbols	Detail of samples
Direct thermal decomposition method	as-CuO5-DTa	The CuO calcined at 500°C and sintered at 900°C in air for 10 h
	as-CuO6-DTa	The CuO calcined at 600°C and sintered at 900°C in air for 10 h
	as-CuO7-DTa	The CuO calcined at 700°C and sintered at 900°C in air for 10 h
	as-CuO5-DTb	The CuO calcined at 500°C and sintered at 950°C in air for 10 h
	as-CuO6-DTb	The CuO calcined at 600°C and sintered at 950°C in air for 10 h
	as-CuO7-DTb	The CuO calcined at 700°C and sintered at 950°C in air for 10 h
	as-CuO5-DTa	The CuO5-DTa annealing under flowing argon at 700°C for 2 h
	Ar-CuO6-DTa	The CuO6-DTa annealing under flowing argon at 700°C for 2 h
	Ar-CuO7-DTa	The CuO7-DTa annealing under flowing argon at 700°C for 2 h

using an inbuilt cooling-heating system. Each measured temperature was kept constant with an accuracy of ±1°C. The complex permittivity,ε^* , was calculated as follows:

$$\varepsilon^* = \varepsilon' - i\varepsilon, \tag{4.1}$$

where

$$\varepsilon' = \frac{Cd}{\varepsilon_0 A}, \tag{4.2}$$

and

$$\varepsilon = \varepsilon' \tan\delta. \tag{4.3}$$

Table 4.1 Symbols for the CuO ceramics fabricated using the CuO powder prepared from different methods (Continue).

Methods	Symbols	Detail of samples
Direct thermal decomposition method	Ar-CuO5-DTb	The CuO5-DTb annealing under flowing argon at 700°C for 2 h
	Ar-CuO6-DTb	The CuO6-DTb annealing under flowing argon at 700°C for 2 h
	Ar-CuO7-DTb	The CuO7-DTb annealing under flowing argon at 700°C for 2 h
	O_2-CuO5-DTa	The Ar-CuO5-DTa annealing under flowing oxygen at 700°C for 2 h
	O_2-CuO6-DTa	The Ar-CuO6-DTa annealing under flowing oxygen at 700°C for 2 h
	O_2-CuO7-DTa	The Ar-CuO7-DTa annealing under flowing oxygen at 700°C for 2 h
	O_2-CuO5-DTb	The Ar-CuO5-DTb annealing under flowing oxygen at 700°C for 2 h
	O_2-CuO6-DTb	The Ar-CuO6-DTb annealing under flowing oxygen at 700°C for 2 h
	O_2-CuO7-DTb	The Ar-CuO7-DTb annealing under flowing oxygen at 700°C for 2 h

ε_0 is the permittivity in free space, A is the sample area and d is the sample thickness.

The complex impedance, Z^*, was calculated as follows:

$$Z^* = \frac{1}{i\omega C_0 \varepsilon^*}, \tag{4.4}$$

where ω is the angular frequency $\omega = 2\pi f$. $C_0 = \varepsilon_0 A/d$ is the empty cell capacitance.

The values of the impedance were obtained by a complex plane method, known as Cole-Cole plot (Sinclair and West, 1989), which plots between the real part, Z', and the imaginary part, Z'', according to the x and y axis, respectively. The data usually takes the form of semi-circles. The Cole-Cole plot is especially

Table 4.1 Symbols for the CuO ceramics fabricated using the CuO powder prepared from different methods (Continue).

Methods	Symbols	Detail of samples
Polymer Pyrolysis solution method	as-CuO5-PRa	The CuO calcined at 500°C and sintered at 900°C in air for 10 h
	as-CuO6-PRa	The CuO calcined at 600°C and sintered at 900°C in air for 10 h
	as-CuO7-PRa	The CuO calcined at 700°C and sintered at 900°C in air for 10 h
	as-CuO5-PRb	The CuO calcined at 500°C and sintered at 950°C in air for 10 h
	as-CuO6-PRb	The CuO calcined at 600°C and sintered at 950°C in air for 10 h
	as-CuO7-PRb	The CuO calcined at 700°C and sintered at 950°C in air for 10 h
	Ar-CuO5-PRa	The CuO5-PRa annealing under flowing argon at 700°C for 2 h
	Ar-CuO6-PRa	The CuO6-PRa annealing under flowing argon at 700°C for 2 h
	Ar-CuO7-PRa	The CuO7-PRa annealing under flowing argon at 700°C for 2 h

useful to estimate the electrical properties of polycrystalline sample since it can estimate the electrical property of grain and grain boundary separately. Therefore, the complex impedance plots were used to investigate the electrical properties of polycrystalline CuO pellets in the temperature range of -50°C to 130°C.

The dielectric properties and dielectric loss tangent ($\tan\delta$) under uniaxial compressive stress were measured by LCR-meter (Instrek LCR-821). The uniaxial compressive stress machine used in this study was designed and described by Yimnirun and co-workers (Yimnirun et al., 2003; Yimnirun et al., 2005; Yimnirun, 2006). The room temperature ($\sim$ 27°C) capacitance and the dielectric loss tangent were obtained at frequency range 1 to 200 kHz under uniaxial compressive prestress levels up to 65 MPa. The dielectric constant was then calculated from a parallel-plate capacitor equation, e.g. $\varepsilon_r = Cd/\varepsilon_0 A$, where C is the capacitance

Table 4.1 Symbols for the CuO ceramics fabricated using the CuO powder prepared from different methods (Continue).

Methods	Symbols	Detail of samples
Polymer Pyrolysis solution method	Ar-CuO5-PRb	The CuO5-PRb annealing under flowing argon at 700°C for 2 h
	Ar-CuO6-PRb	The CuO6-PRb annealing under flowing argon at 700°C for 2 h
	Ar-CuO7-PRb	The CuO7-PRb annealing under flowing argon at 700°C for 2 h
	O_2-CuO5-PRa	The Ar-CuO5-PRa annealing under flowing oxygen at 700°C for 2 h
	O_2-CuO6-PRa	The Ar-CuO6-PRa annealing under flowing oxygen at 700°C for 2 h
	O_2-CuO7-PRa	The CuO7-PRa-Ar annealing under flowing oxygen at 700°C for 2 h
	O_2-CuO5-PRb	The Ar-CuO5-PRb annealing under flowing oxygen at 700°C for 2 h
	O_2-CuO6-PRb	The Ar-CuO6-PRb annealing under flowing oxygen at 700°C for 2 h
	O_2-CuO7-PRb	The Ar-CuO7-PRb annealing under flowing oxygen at 700°C for 2 h

of the specimens, d and A are, respectively, the thickness and the area of the electrode, and ε_0 is the dielectric permittivity of vacuum (8.854×10^{12} F/m).

CHAPTER V

CHARECTERIZATION OF CuO

In this chapter, the basic characteristics such as thermal behavior, phase composition, microstructure and morphology of the dried precursors and calcined powders are shown and discussed in section 5.1. Phase composition and microstructure of the sintered samples are presented in section 5.2.

5.1 Characterization of CuO powder

5.1.1 The thermal behavior of the as-prepared powder

The thermal behavior of the as-prepared CuO precursor powder was investigated by TG-DTA analysis at a heating rate of 15°C in static air from room temperature to 1000°C. The results of TG-DTA measurements of the as-prepared CuO precursor powders prepared by DT method are shown in Figure 5.1. In Figure 5.1 the TG curve contained two steps decrease of weight loss due to dehydration and decomposition of the anhydrous salt. The first step was endothermic took place in the temperature range of 110 - 150°C, involving the loss of one molecule of water with a mass loss of about 10%. The second step started at about 200°C and was completed at about 300°C; it was exothermic, due to oxidation and reduction corresponded to a mass loss of about 58%, giving rise to decomposition of the anhydrous salt to copper metal. Above 300°C, a slightly increase of mass was observed in the TG curve and a corresponding broad exothermic peak in the DTA curve, due to the partial oxidation of Cu to CuO. In addition, the clear plateau formed at 400°C on the TG curve indicates the formation of CuO as a decomposition product. It is noted that the TG-DTA curves of the as-prepared precursor powder of the PR method cannot be measured as the sample composes of the pure phase of CuO only.

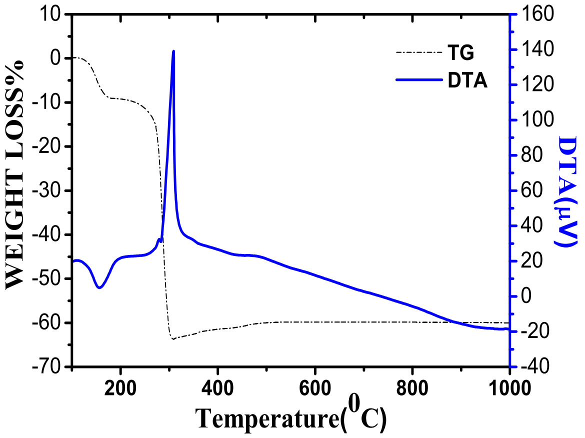

Figure 5.1 TG-DTA curves of the as-prepared precursor powder of CuO prepared by using DT method.

5.1.2 X-rays diffraction of the calcined powder

The XRD patterns of commercial CuO powder (99.99%, purity, Aldrich) is shown in Figure 5.2. It is clearly seen from this figure that the commercial CuO powder shows a single phase of CuO (JCPDS card No.05-0661). The crystalline size of this powder (by using Sheerer formula) is obtained to be 43.39 ± 9 nm. The monoclinic lattice parameters a, b and c calculated from the XRD spectra by using the Rietveld method (Ahmed Farag et al., 2001) are obtained to be 4.6950(2), 3.4391(2) and 5.1492(3)$\mathring{A}$ respectively. These values are comparable to those of the lattice constants $a = 4.684$, $b = 3.425$ and $c = 5.129\mathring{A}$ for the standard data.

Figure 5.3 shows the XRD patterns of dried precursor and calcined powders prepared by the DT method at various calcined temperatures. The main peaks

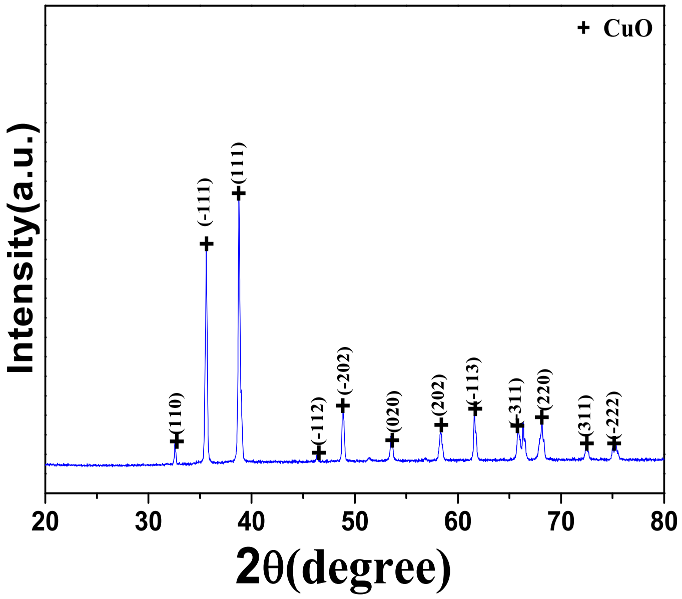

Figure 5.2 XRD patterns of the commercial CuO powder (Aldrich, 99.99%).

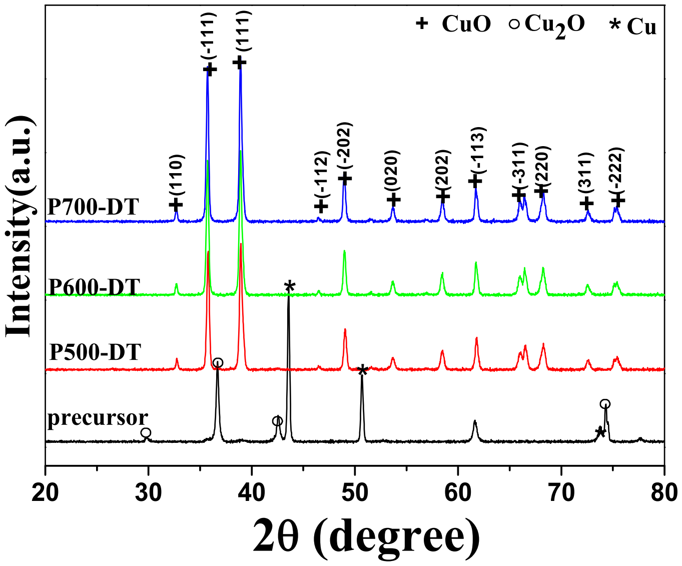

Figure 5.3 XRD patterns of the as-prepared precursor and the powders calcined at 500, 600 and 700°C in air for the DT method.

of all calcined powders display a main phase of CuO. However, the second phases of Cu_2O (JCPDS card No.75-1571) and Cu (JCPDS card No.85-1326) can be observed in the dried precursor. From the line broadening of the main peaks, the crystallite size was estimated using the Scherrer's formula (Cullity and Stock, 2001) and Stock, 2001). The crystalline sizes of the powders calcined at 500, 600 and 700°C are obtained to be 32.83 ± 7, 35.32 ± 8 and 39.18 ± 10 nm respectively. The lattice parameters a, b and c calculated from the XRD spectra (by using Rietveld method) are 4.6862(4), 3.4250(3) and 5.1322(4), 4.6868(5), 3.4263(4) and 5.1334(5), 4.6862(4), 3.4250(3) and 5.1322(4)$\mathring{A}$ for the CuO powders calcined at 500, 600 and 700°C, respectively.

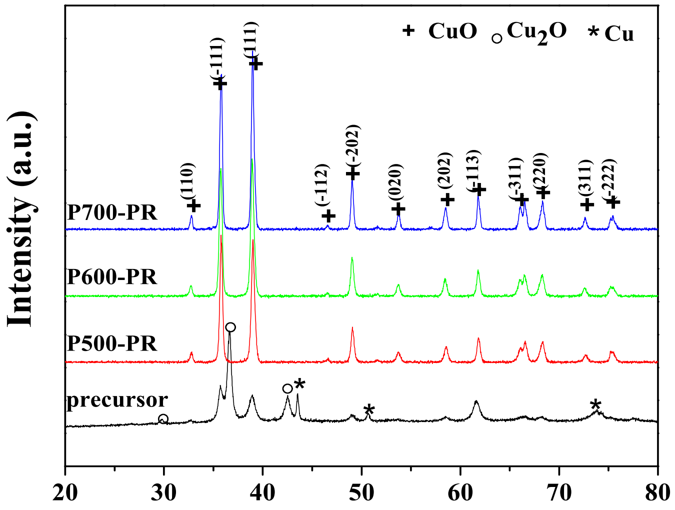

Figure 5.4 XRD patterns of the as-prepared precursor and the powders calcined at 500, 600 and 700°C in air for the PR method.

Figure 5.4 shows the XRD patterns of dried precursor and calcined powders prepared by the PR method at various calcined temperatures. The main peaks of all calcined powders display a main phase of CuO. However, the second phases of Cu_2O (JCPDS card No.75-1571) and Cu (JCPDS card No.85-1326) can be observed in the dried precursor as also found for the DT method. From the line broadening of the main peaks, the crystallite size was again estimated using the Scherrer formula (Cullity and Stock, 2001) and found to be 25.87 ± 4, 28.05 ± 8 and 34.44 ± 7 nm for the powders calcined at 500, 600 and 700°C, respectively. The lattice parameters a, b and c calculated from the XRD spectra (by using Rythwell method) are 4.6840(3), 3.4269(3) and 5.1315(4), 4.6839(3), 3.4246(3) and 5.1306(3), 4.6862(3), 3.4238(2) and 5.1317(3)$\mathring{A}$ for powders calcined at 500, 600, and 700°C, respectively.

The crystalline size and lattice parameter of the commercial CuO, DT and PR powders are summarized in Table 5.1. The crystalline size of all CuO powders is in the order of nanometer scale. The crystalline size of the commercial CuO powder is 43.39 ± 9 nm. The crystalline sizes of DT and PR powders increase from 32.83 nm to 39.18 nm and 25.87 nm to 34.44 nm as the calcination temperature is increased from 500°C to 700°C, respectively. The crystalline sizes of the CuO powders prepared by the PR method is smaller than those prepared by the DT method at the same calcination temperature, since in the PR method, a soluable synthesis technique can afford an intimate and homogeneous mixing of metal ions at the atomic scale, thus reducing the diffusion path length required. Shorter diffusion lengths require shorter reaction times and lower temperature. The lattice parameters $a, b$and c of the powders calculated from the XRD spectra are close to those of lattice constants quoted in the standard data.

The XRD patterns of the precursor prepared by the PR method (shown in Figure 5.4) show that the precursor contains crystalline Cu_2O and Cu metal. This indicates that the metal nitrates form oxides in the first step of the process or during the heat treatment. From the XRD results the phase composition of the prepared CuO powders calcined in the range of 500 - 700°C consists of the main phase of CuO.

Table 5.1 The crystallite size and lattice parameter of the commercial CuO, DT and PR powders.

powders	Material	Particle size (nm)	Lattice parameter $a(\mathring{A})$	$b(\mathring{A})$	$c(\mathring{A})$
standard	JCPDS(05-0661)	-	4.684	3.425	5.129
Commercial	CuO-99.99P	43.39 ± 9	4.695	3.439	5.149
DT method	P500-DT	32.83 ± 7	4.6862(4)	3.4250(3)	5.1322(4)
	P600-DT	35.32 ± 7	4.6868(5)	3.4263(4)	5.1334(5)
	P700-DT	39.18 ± 10	4.6862(4)	3.4250(3)	5.1322(4)
PR method	P500-PR	25.87 ± 4	4.6840(3)	3.4269(3)	5.1315(4)
	P600-PR	28.05 ± 8	4.6839(3)	3.4246(3)	5.1306(3)
	P700-PR	34.44 ± 7	4.6862(3)	3.4238(2)	5.1317(3)

5.1.3 SEM analysis of the CuO powder

Morphology of the commercial CuO, DT and PR powders revealed by SEM are shown in Figures 5.5 - 5.7. Figure 5.5 shows CuO particles with the average size of about 43 nm for the commercial CuO powders. Figure 5.6 shows CuO particles with the average sizes of about 32, 35 and 39 nm for the DT-prepared CuO powders, calcined at 500, 600 and 700°C, respectively. Figure 5.7 shows CuO particles with the average sizes of about 26, 28 and 34 nm for the PR-prepared CuO powders calcined at 500, 600 and 700°C, respectively. It is seen from Figures 5.5 - 5.7 that some agglomerates are observed in all of the calcined powders, and the particle size of the powders increases with increasing the calcination temperature.

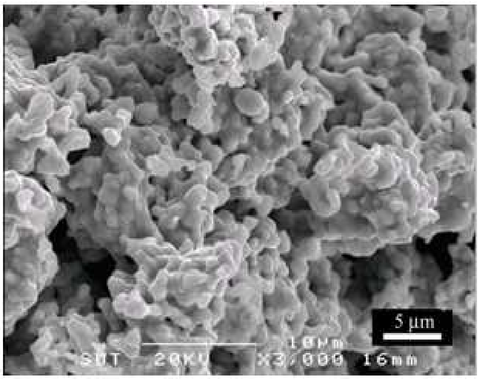

Figure 5.5 SEM micrographs of the commercial CuO powders.

5.2 Characterization of CuO ceramics

5.2.1 X-ray diffraction analysis

In this section, the X-ray diffraction technique has been used to carry out phase analysis and study the effect of sintering temperature on the CuO ceramics' structure.

5.2.1.1 X-ray diffraction analysis of the commercial CuO ceramics

The XRD patterns of CuO ceramics prepared from commercial powder, and sintered at 900°C and 950°C for 10 h in air, are shown in the Figures 5.8 (a) and (b) respectively. Figure 5.8 (a) shows the XRD patterns of the CuO ceramics before surface polishing. Apparently, all of these specimens reveal similar diffraction patterns. Therefore, there is no significant change of crystalline phase intensity at these two sintering temperatures. The different phase is related to the structure of space group C2/c according to JCPDS No.05-0661. It is also observed that all the CuO ceramics show distinct (110), (-111), (111), (-112), (-202), (020), (202), (-113), (-311), (220), (311) and (-222) planes, thus demonstrating a polycrystalline characteristic. This indicates that all of the ceramic samples prepared in the present study have a good polycrystalline structure in spite of their differ-

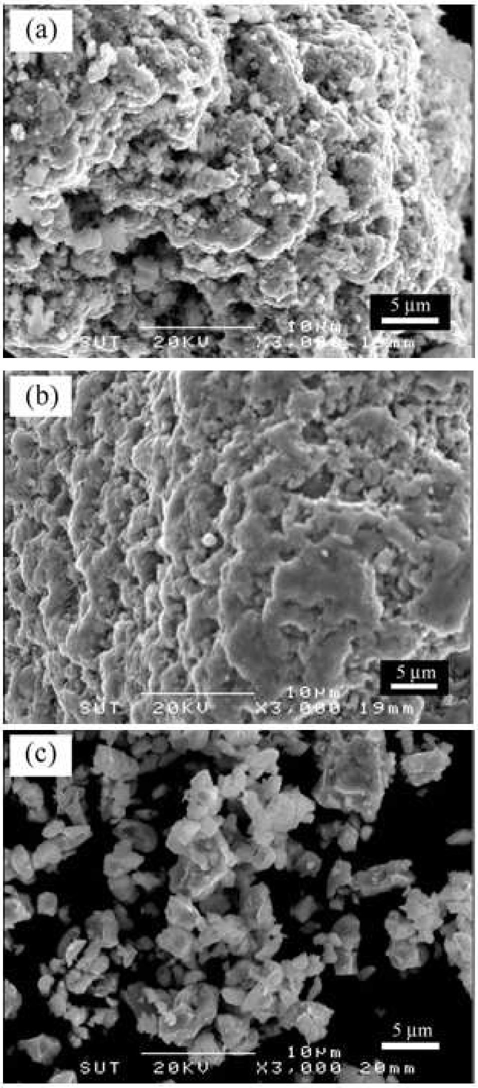

Figure 5.6 SEM micrographs of the DT-prepared CuO powders calcined at (a) 500°C, (b) 600°C and (c) 700°C for 6 h in air, respectively.

ent microstructures. The monoclinic lattice parameters a, b and c calculated from the XRD spectra are 4.6869(2), 3.4224(2) and 5.1294(2), 4.6879(4), 3.4224(3) and 5.1305(4)$\mathring{A}$ for CuO-99.99a and CuO-99.99b respectively. These values are close to those of the lattice constants $a = 4.684$, $b = 3.425$ and $c = 5.129$ in the standard data. Figure 5.8 (b) shows the XRD patterns of CuO ceramics after 1/3 of the pellets were polished off. The results show the decrease of the peaks intensities in (111) plane and the increase of that with small amount in (-111) plane of

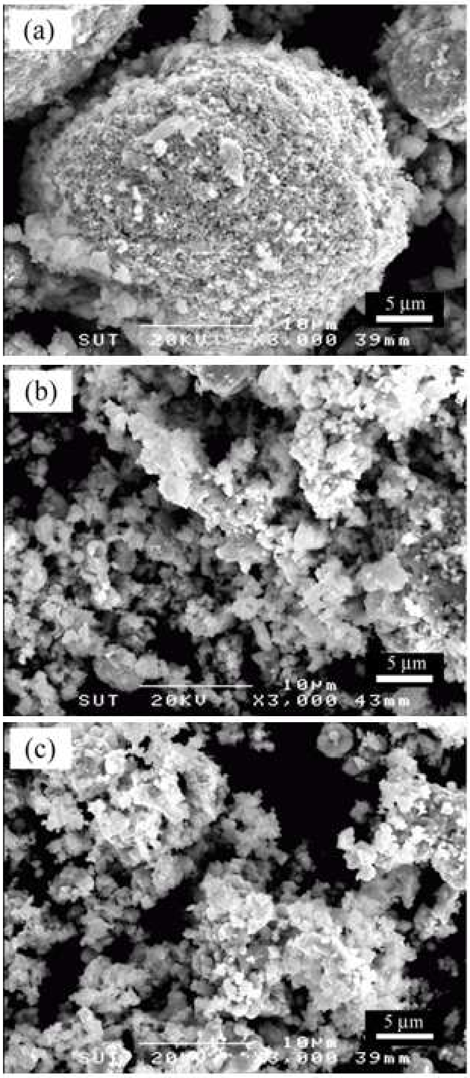

Figure 5.7 SEM micrographs of the PR-prepared CuO powders calcined at (a) 500°C, (b) 600°C and (c) 700°C for 6 h in air, respectively.

CuO-99.99b ceramic, while the peaks intensities of the other planes do not change.

5.2.1.2 X-rays diffraction analysis of CuO ceramics prepared by DT method

The XRD patterns of the DT-prepared CuO ceramics sintered at 900°C for 10 h in air before and after surface polishing are shown in Figures 5.9 (a) and 5.9 (b) respectively. This confirms the main phase of CuO in all samples although a small amount of intensities are presented in all polished ceramic surface. Moreover,

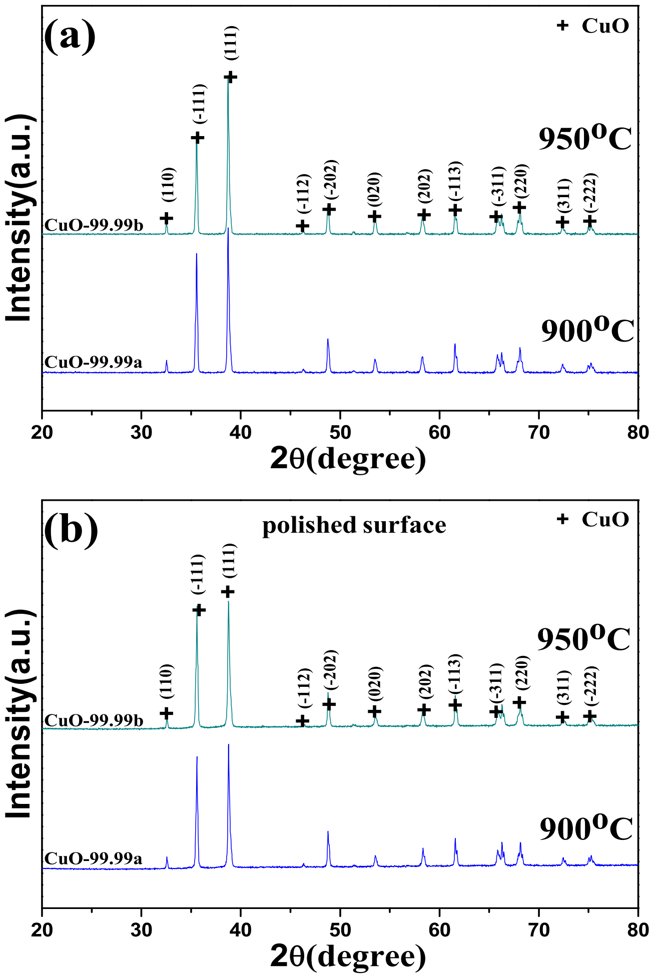

Figure 5.8 XRD patterns of CuO ceramic prepared from commercial CuO powders (a) before polishing (CuO-99.99a) and (b) after polishing (CuO-99.99b).

it is observed that all the CuO ceramics show distinct (110), (-111), (111), (-112), (-202), (020), (202), (-113), (-311), (220), (311) and (-222) planes thus demonstrating a polycrystalline characteristic. Similar patterns are also observed for the CuO ceramics sintered at 950°C for 10 h in air before and after surface polishing as shown in Figures 5.9 (c) and 5.9 (d) respectively. The monoclinic lattice parameters a, b and c of unpolished samples calculated from the XRD spectra are respectively 4.6874(3), 3.4237(3) and 5.1315(3)$\mathring{A}$ for CuO5-DTa; 4.6870(3), 3.4226(2) and 5.1310(3) for CuO6-DTb; 4.6876(3), 3.4227(3) and 5.1312(4)$\mathring{A}$ for CuO7-

DTa; 4.6874(4), 3.4228(3) and 5.1315(4)$\mathring{A}$ for CuO5-DTb; 4.6882(3), 3.4227(3) and 5.1319(4) for CuO6-DTb; 4.6874(2), 3.4222(1) and 5.1313(2)$\mathring{A}$ for CuO7-DTb. These values are close to those of the lattice constants a = 4.684, b = 3.425 and c = 5.129$\mathring{A}$ in the standard data. The monoclinic lattice parameters a, b and c of polished samples are also similar to these values.

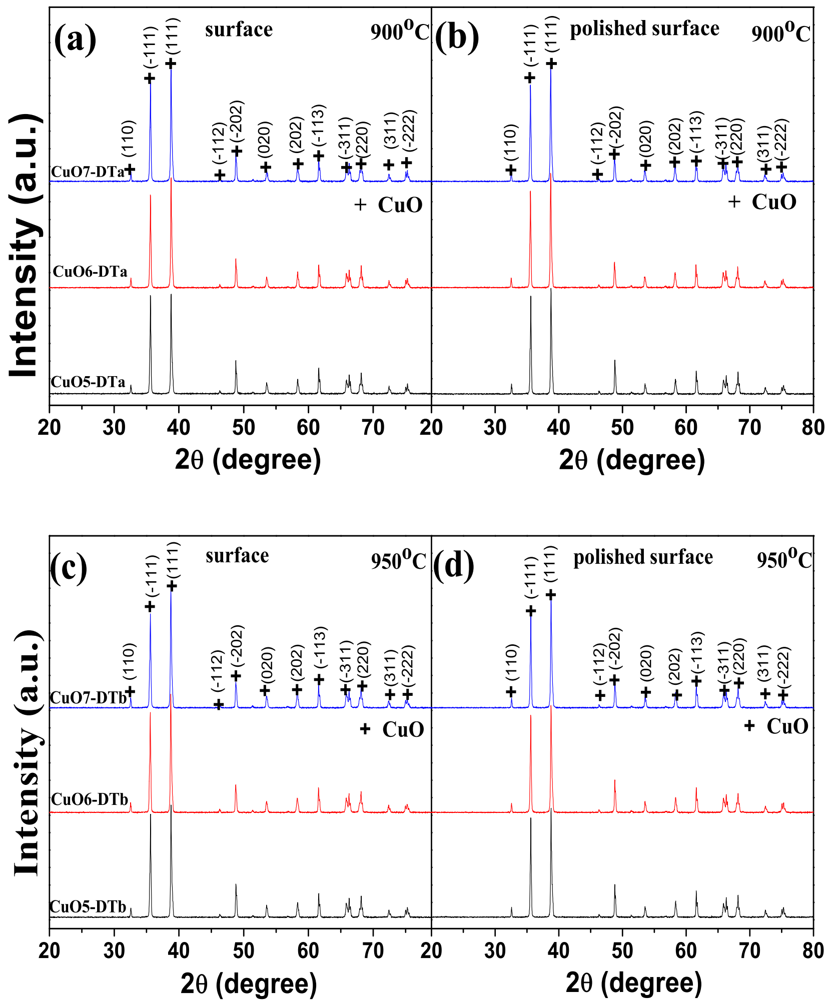

Figure 5.9 XRD patterns of DT-prepared CuO, sintered at 900°C for 10 h in air (a) before polishing and (b) after polishing (CuO5-DTa, CuO6-DTa and CuO7-DTa) and the samples sintered at 950°C for 10 h in air (c) before polishing and (d) after polishing (CuO5-DTb, CuO6-DTb and CuO7-DTb).

5.2.1.3 X-ray diffraction analysis of CuO ceramics prepared by PR method

The XRD patterns of the PR-prepared CuO ceramics sintered at 900°C for 10 h in air before and after surface polishing are shown in Figures 5.10 (a) and 5.10 (b) respectively. This confirms again the main phase of CuO in all samples and the distinct (110), (-111), (111), (-112), (-202), (020), (202), (-113), (-311), (220), (311) and (-222) planes demonstrate a polycrystalline characteristic. Similar patterns are also observed for the CuO ceramics sintered at 950°C for 10 h in air before and after surface polishing as shown in Figures 5.10 (c) and 5.10 (d) respectively. The monoclinic lattice parameters a, b and c of the unpolished samples calculated from the XRD spectra are respectively 4.6866(3), 3.4233(2) and 5.1309(3)$\mathring{A}$ for CuO5-PRa; 4.6875(3), 3.4210(3) and 5.1303(4) for CuO6-PRb; 4.6899(4), 3.4206(3) and 5.1313(4)$\mathring{A}$ for CuO7-PRa; 4.6869(3), 3.4222(2) and 5.1307(3)$\mathring{A}$ for CuO5-PRb; 4.6899(2), 3.4196(1) and 5.1314(2) for CuO6-PRb; 4.6875(2), 3.4231(2) and 5.1312(2)$\mathring{A}$ for CuO7-PRb. These values are close to those of the lattice constants $a = 4.684$, $b = 3.425$ and $c = 5.129\mathring{A}$ in the standard data. The monoclinic lattice parameters a, b and c of polished samples are similar to these values. It is obvious that the peaks' intensities of (-111) and (111) planes in the polished samples of CuO6-PRb and CuO7-PRb ceramics are decreased.

5.2.2 SEM analysis

5.2.2.1 SEM analysis of the commercial powder-prepared CuO ceramics

It is well known that many physical properties such as mechanical property, electrical property of polycrystalline CuO are very sensitive to the microstructure (Sarkar et al., 2008a; Thongbai et al., 2008b). Thus, the information associated with the physical parameters of each component that constitutes the

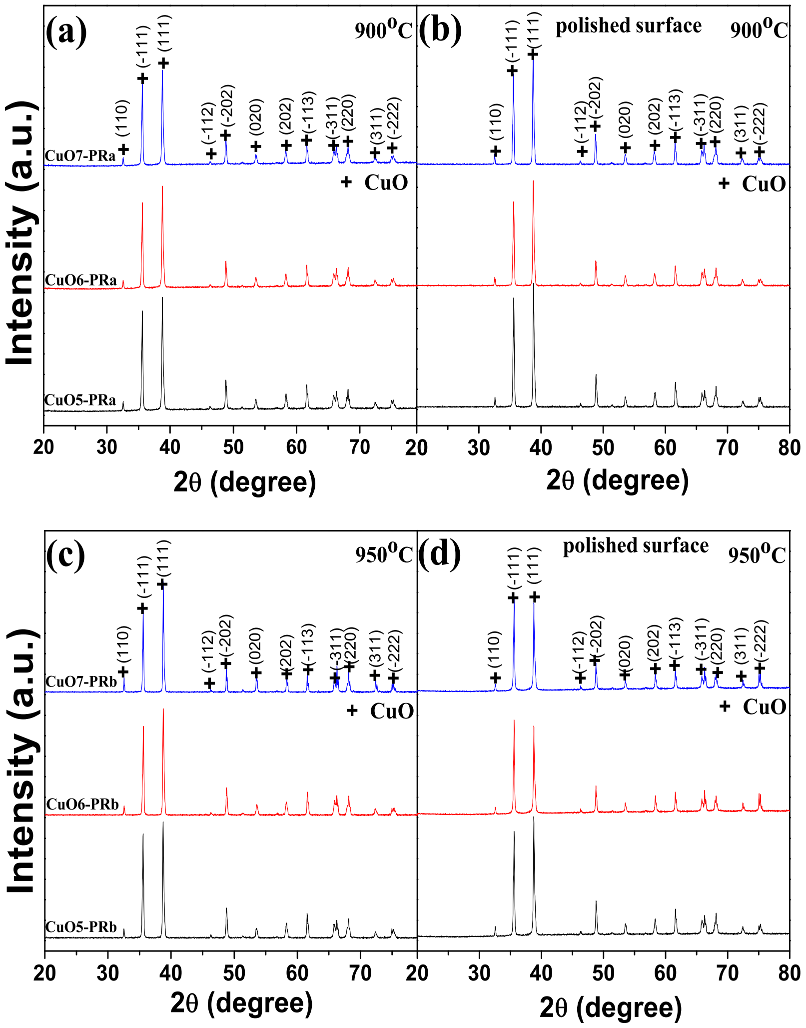

Figure 5.10 XRD patterns of PR-pprepared CuO ceramics, sintered at 900°C for 10 h in air (a) before polishing (b) after polishing (CuO5-PRa, CuO6-PRa and CuO7-PRa) and the samples sintered at 950°C for 10 h in air (c) before polishing and (d) after polishing (CuO5-PRb, CuO6-PRb and CuO7-PRb).

microstructure is very important in comprehension of the materials' properties. In this topic the microstructure of the commercial powder-prepared CuO ceramics with different sintering temperatures was studied by SEM. Figures 5.11 (a) and (b) show the surface morphology of the CuO-99.99a and CuO-99.99b with the mean grain size of 3.9 ± 1.5 and 6.5 ± 2.3 m respectively. From these results, all grains have larger dimensions as temperature increases. This suggests that the morphologies increase with increasing the sintering temperature. In addition, with an increase of sintering temperature, the grain boundary is significantly reduced. A similar phenomenon was observed by Thongbai and Sarkar (Thongbai et al., 2008b; Sarkar et al., 2008a). Significantly, stoichiometry of the grain and the grain boundary of CuO ceramics are also found to be strongly dependent on the sintering temperature, which is confirmed to be insensitive to the processing conditions. These microstructural and stoichiometric differences are likely to have substantial influence on their dielectric properties. The details of which are elucidated in chapter 6 section 6.1.

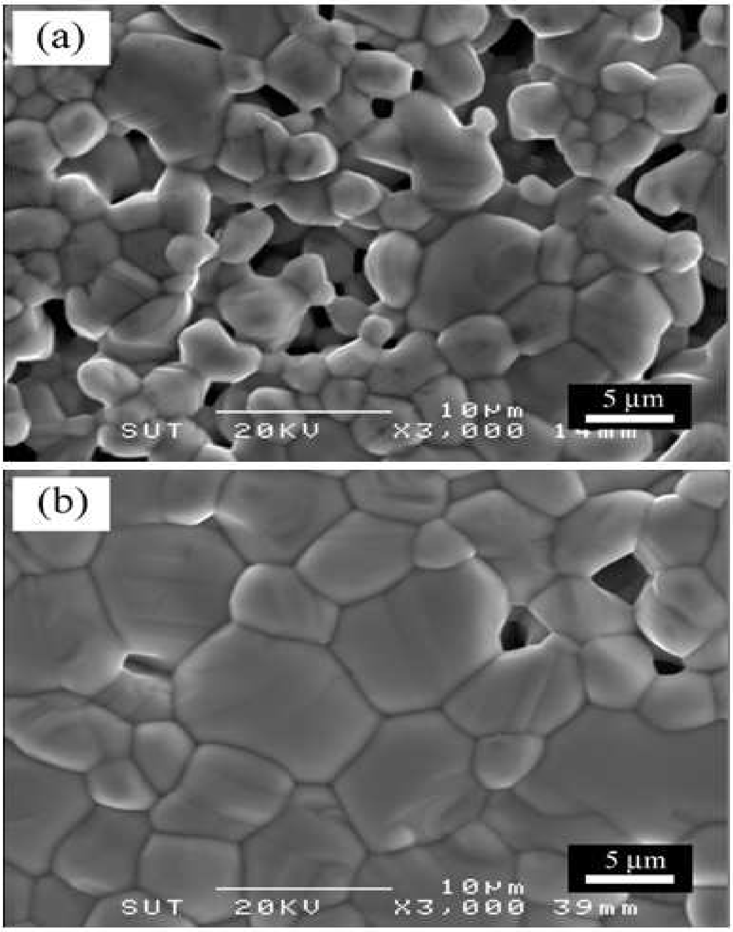

Figure 5.11 SEM micrographs of the commercial powder-prepared CuO ceramics after (a) sintered at 900°C for 10 h in air (CuO-99.99a), (b) sintered at 950°C for 10 h in air (CuO-99.99a), respectively.

5.2.2.2 SEM analysis of the CuO ceramics prepared by the DT method

The microstructures of all the DT-prepared CuO ceramics sintered at 900°C (CuO5-99.99a, CuO6-99.99a and CuO7-99.99a) and at 9550°C (CuO5-99.99b, CuO6-99.99b and CuO7-99.99b) as revealed by SEM are shown in Figures 5.12 (a), (b) and (c) and Figures 5.12 (d), (e) and (f), respectively. The mean grain sizes are obtained to be 4.82 ± 1.07, 4.46 ± 1.55 and 3.57 ± 1.21 μm for ceramics sintered at 900°C whereas those of the ceramics sintered at 950°C are 5.41 ± 2.24, 6.20 ± 2.16 and 5.00 ± 1.33 μm for the samples prepared from the powders calcined at 500, 600 and 700°C respectively. Similarly to the results obtained for the commercial powder-prepared CuO ceramics (section 5.2.2.1), all grains have the larger dimensions as the sintering temperature is increased. This suggests that the morphologies of the ceramics are changed with extending the sintering temperature.

5.2.2.3 SEM analysis of the CuO ceramics prepared by the PR method

The microstructures of the PR-prepared CuO ceramics sintered at 900°C (CuO5-PRa, CuO6-PRa and CuO7-PRa) and at 950°C (CuO5-PRb, CuO6-PRb and CuO7-PRb) as revealed by SEM are shown in Figures 5.13 (a), (b) and (c) and Figures 5.13 (d), (e) and (f), respectively. The mean grain sizes are obtained to be 1.89 ± 0.46, 1.62 ± 0.39 and 2.47 ± 0.47 μm for CuO5-PRa, CuO6-PRa and CuO7-PRa, respectively, whereas the ceramics sintered at 950°C are obtained to be 4.61 ± 1.83, 2.54 ± 0.86 and 15.62 ± 5.64 μm for CuO5-PRb, CuO6-PRb and CuO7-PRb respectively. The grains have larger dimensions as the temperature is increased. This suggests that the morphologies are changed with increasing the sintering temperature as in the case of the DT-prepared ceramics.

As mentioned previously, the grain sizes of all the CuO ceramics, prepared by PR method are smaller than those of the samples prepared by the DT method

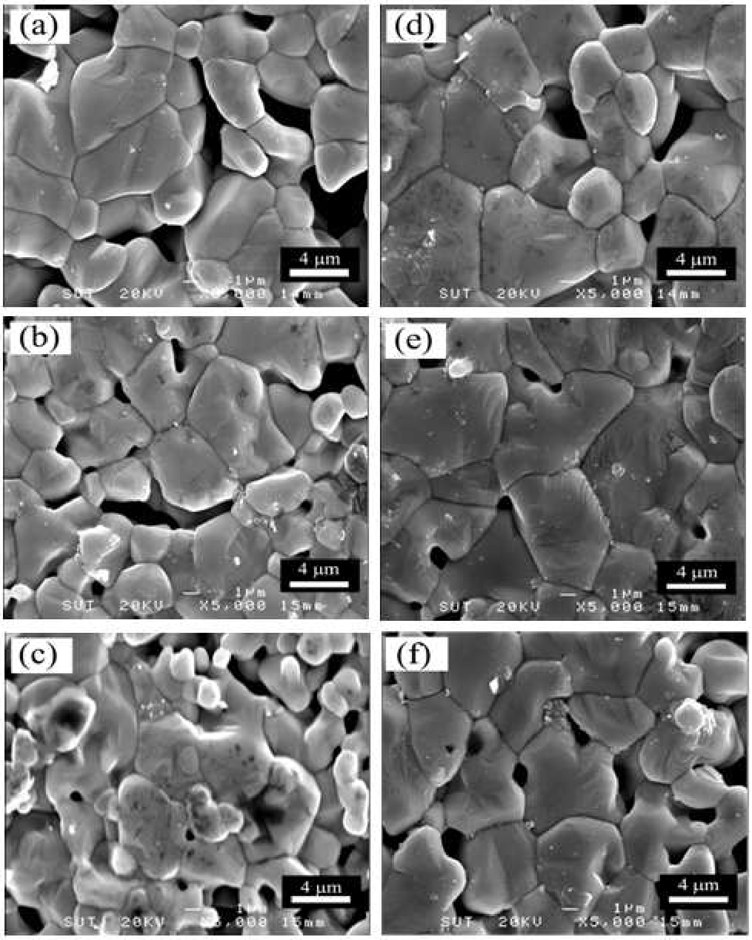

Figure 5.12 SEM micrographs of DT-prepared CuO ceramics, sintered at 900°C for 10 h in air after calcination at (a) 500°C (CuO5-DTa), (b) 600°C (CuO6-DTa) and (c) 700°C (CuO7-DTa) and the samples sintered at 950°C for 10 h in air after calcination at (d) 500°C (CuO5-DTb), (e) 600°C (CuO6-DTb) and (f) 700°C (CuO7-DTb) respectively.

and the commercial powder-prepared CuO ceramics. This implies that the PR-prepared CuO ceramics have a finer microstructure than that of the DT-prepared CuO ceramics. From SEM micrograph, CuO ceramics sintered at 900°C are obviously more porous than other samples. The porosity is decreased with the increase in the sintering temperature which is clearly seen in the SEM micrographs of these ceramic samples sintered at 950°C (Figure 5.10 (b), Figures 5.11 (d), (e) and (f) and Figures 5.12 (d), (e) and (f)). Moreover, the highest average grain size of

15.62 ± 5.64 m is obtained for the CuO7-PRb sample.

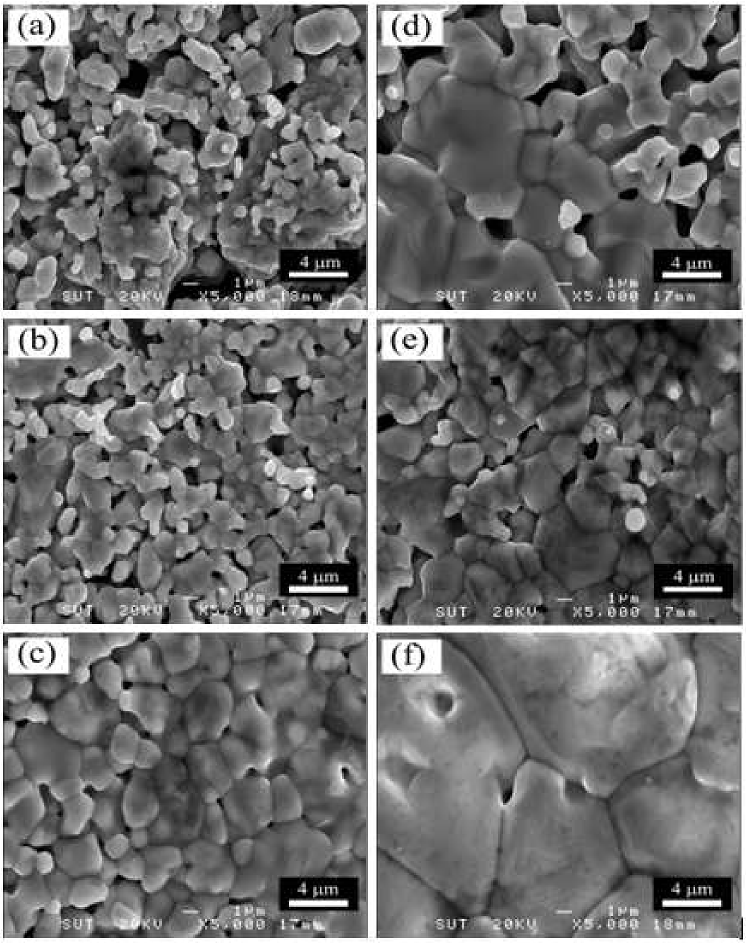

Figure 5.13 SEM micrographs of the PR-prepared CuO ceramics, sintered at 900°C for 10h in air after calcination at (a) 500°C (CuO5-PRa), (b) 600°C (CuO6-PRa) and (c) 700°C (CuO7-PRa) and the samples sintered at 950°C for 10 h in air after calcinations at (d) 500°C (CuO5-PRb), (e) 600°C (CuO6-PRb) and (f) 700°C (CuO7-PRb) respectively.

Table 5.2 Properties of the CuO ceramics sintered in air at 900°C and 950°C for 10 h. Monoclinic lattice parameters (a, b and c) obtained by the XRD patterns. Grain sizes are determined from the SEM image.

Materials	Grain size range(μm)	Average grain size(mm)	Lattice parameters		
			a (A°)	b (A°)	c (A°)
JCPDS (05-0661)	-	-	4.684	3.425	5.129
CuO- 99.99a	2 - 8	3.86 ± 1.5	4.6869(2)	3.4224(2)	5.1294(2)
CuO- 99.99b	3 - 12	6.45 ± 2.3	4.6879(4)	3.4224(3)	5.1305(4)
as-CuO5- DTa	2.5 - 9	4.82 ± 1.07	4.6874(3)	3.4237(3)	5.1315(3)
as-CuO6- DTa	2 - 9	4.46 ± 1.55	4.6870(3)	3.4226(2)	5.1310(3)
as-CuO7- DTa	2 - 6	3.57 ± 1.21	4.6876(3)	3.4227(3)	5.1312(4)
as-CuO5- DTb	2 - 10	5.41 ± 2.24	4.6874(4)	3.4228(3)	5.1315(4)
as-CuO6- DTb	3 - 11	6.20 ± 2.16	4.6882(3)	3.4227(3)	5.1319(4)
as-CuO7- DTb	2 - 7.5	5.00 ± 1.33	4.6874(2)	3.4222(1)	5.1313(2)
as-CuO5- PRa	1 - 3	1.89 ± 0.46	4.6866(3)	3.4233(2)	5.1309(3)
as-CuO6- PRa	1 - 2.5	1.62 ± 0.39	4.6875(3)	3.4210(3)	5.1303(4)
as-CuO7- PRa	1 - 5	2.47 ± 0.47	4.6899(4)	3.4206(3)	5.1313(4)
as-CuO5- PRb	2 - 10	4.61 ± 1.83	4.6869(3)	3.4222(2)	5.1307(3)
as-CuO6- PRb	1 - 6	2.54 ± 0.86	4.6899(2)	3.4196(1)	5.1314(2)
as-CuO7- PRb	4 - 36	15.62 ± 5.64	4.6875(2)	3.4231(2)	5.1312(2)

CHAPTER VI

DIELECTRIC PROPERTIES OF CuO

In this chapter, the electrical properties of the CuO ceramics such as dielectric properties as a function of frequency and temperature of the samples prepared by using commercial CuO powder, direct thermal decomposition and polymer pyrolysis solution methods, are examined. The dielectric behavior of the sintered CuO ceramics, pre- and post-annealing in argon at 700°C for 2 h and then re-annealing in oxygen at 700°C for 2 h are investigated. The dielectric properties of polycrystalline CuO ceramics are characterized by the impedance spectroscopy (IS) model and the correlation between the dielectric properties and the effect of annealing in argon, oxygen and sintered temperature are discussed. In the last section, the effects of dc bias voltage and uniaxial compressive stress on the dielectric behavior of the pre-annealing CuO ceramics are discussed. The notation of these samples is previously labeled in Table 4.1.

6.1 Electrical properties of the CuO ceramics prepared from the commercial CuO powder

6.1.1 Dielectric properties

In this section, the dielectric behavior of the as-, Ar-, O_2-CuO-99.99a and as-, Ar-, O_2-CuO-99.99b samples, are examined. The frequency dependence of dielectric constant (ε') and the dielectric loss tangent (tan δ) for these samples (as-, Ar-, O_2-CuO-99.99a and for as-, Ar-, O_2-CuO-99.99b) are shown in Figures

6.1 (a-f) on the left and right axis, respectively. In the temperatures ranging from -50°C to 30°C, the as-CuO-99.99a (Figure 6.1 (a)) and as-CuO-99.99b (Figure 6.1 (d)) show the values of the ε' of $(1.85 - 1.99) \times 10^4$ and $(2.12 - 2.22) \times 10^4$ and show the tanδ at 1 kHz of (1.85 - 26.30) and (5.45 - 34.39). However, after annealing in argon the ε' is reduced to $(2.12 - 2.23) \times 10^3$ and $(6.60 - 9.38) \times 10^3$ corresponding to the increase of the tanδ with the values in the range of (73.60-447.00) and (11.20-72.20) for the Ar-CuO-99.99a and Ar-CuO-99.99b (Figures 6.1 (b) and (e)) respectively. Moreover, the ε' is increased to the origin at the values of $(2.12 - 2.23) \times 10^4$ and $(1.50 - 1.38) \times 10^4$ after re-annealing in oxygen, whereas the tanδ is reduced to (4.05 - 34.30) and (15.60 - 127.00) (Figures 6.1 (c) and 6.1 (f)) for the O_2-CuO-99.99a and O_2-CuO-99.99b, respectively.

As previously seen, both samples (CuO-99.99a and CuO-99.99b) exhibit dielectric constant value $\sim$ $(1.2 - 2.2) \times 10^4$ and after annealing in argon the dielectric constant is reduced to $\sim$ $(2.1 - 9.4) \times 10^3$ and recovered to around the initial value of $\sim$ $(1.5 - 2.2) \times 10^4$ by re-annealing in oxygen. Most samples exhibit the Debye-like relaxation (Ramirez et al., 2000; Lunkenheimer et al., 2004; Sarkar et al., 2006; Thongbai et al., 2008b). The giant dielectric behavior of annealing process corresponds to the dielectric loss tangent. Namely, the increase in two or three orders of magnitude of the dielectric loss tangent after annealing in argon of both samples (Figures 6.1 (b) and 6.1 (c)) causes the reduction of the dielectric constant. The decrease in three or four orders of magnitude of the external resistance (R_{ext}) (Figures 6.4 (b) and (e)), is due to the oxygen vacancy in the external part (surface layer and electrode) which is increased, and causes the accumulation of the charges carrier at the external part (interfacial polarization) and the total polarization to decrease. However, the dielectric constant can be recovered around the initial value by annealing in oxygen resulting in the new surface layer and the total polarization to be increased. This process the new surface layer in the samples after re-annealing in oxygen causing the increase of the external resistance of both ceramics (Figures 6.4 (c) and (f)).

As observed in Figures 6.1 (a) - (f), after annealing in argon at 700°C for 2 h, the ε' and tanδ of the samples are respectively lower and higher than those of the as- samples. Moreover, at high temperature, both ε' and tanδ values of the post- annealing sintering samples (Ar-CuO-99.99a and Ar-CuO-99.99b) depend strongly on temperature and frequency than those of the as-samples. It is known that annealing of the samples in the reducing atmosphere at high temperature will increase the concentration of oxygen vacancies. This can be expressed by the following reaction (Wang and Zhang, 2006a):

$$\mathrm{O_0(oxygenionatitsnormalsite)} \rightarrow \mathrm{V_0^{2+}(oxygenvacancy)} + 2\mathrm{e}^- + \frac{1}{2}\mathrm{O_2} \qquad (6.1)$$

The decrease in ε' for the post-annealing samples is possibly associated with the decrease of charge carrier accumulated at the interface between surface layer and electrode. Meanwhile, the increase in tan for the post-annealing samples is associated with the increase of conducting electron. The ionization of the oxygen vacancies will create the conducting electron. This process follows the reaction as shown in Eq. (6.1).

The temperature dependence of dielectric constant and dielectric loss tangent over the temperature range of -50°C to 100°C and between 1 and 200 kHz for the as-, Ar-, O_2-CuO-99.99a and as-, Ar-, O_2-CuO-99.99b samples are shown in Figures 6.2 (a) - (c) and 6.2 (d) - (f) (left and right axis), respectively. It is clearly seen that these samples show giant dielectric constant and which are independent on temperature (above -50°C) at all frequency. The dielectric loss tangent for all of the samples shifts to the higher temperature side with increasing frequency. This indicates that thermally activated relaxation also occurs in the CuO-99.99 sample as priviously observed by (Sarkar et al., 2006; Thongbai et al., 2008b).

To make further understanding of the physical nature of the observed dielectric relaxation of the as-, Ar-, O_2-CuO-99.99a and as-, Ar-, O_2-CuO-99.99b samples, the data of the dielectric spectra were fitted with the Cole-Cole equation,

$$\varepsilon^* = \varepsilon' - j\varepsilon'' = \varepsilon_\infty + \frac{\varepsilon_s - \varepsilon_\infty}{1 + (j\omega\tau)}, \qquad (6.2)$$

where ε_s and ε_∞ are the static and high frequency limits of dielectric permittivity, respectively. τ is the relaxation time, and α is the distribution of the relaxation time. It is clearly seen from Figures 6.3 (a) - (c) and 6.3 (d) - (f) that the relaxation time can be well fitted with the Cole-Cole equation and it is the Debye-type relaxation. The values of α are obtained to be 0.82 - 0.86, 0.69 - 0.75, 0.7 - 0.78 (region 1) and 0.81 - 0.83 (region 2) for the as-, Ar- and O_2-CuO-99.99a ceramics (Figures 6.3 (a) - (c)), respectively; and 0.69 - 0.75, 0.73 - 0.82 and 0.70 - 0.79 (region 1), 0.83 - 0.92 (region 2) for the as-, Ar- and O_2-CuO-99.99b (Figures 6.3 (d) - (f)), respectively. The relaxation times of these samples are summarized in Table 1.

From the fitting results, we found that the fitted τ values at different temperatures (-50°C to 30°C) of the samples are shown in Table 6.1. It is clearly seen that the relaxation times of the as-CuO-99.99a (as-τ) samples are two or three orders of magnitude and four or five orders of magnitude higher than those of the Ar-CuO-99.99a (Ar-τ) and the O-CuO-99.99a (O_2-τ), respectively. The dielectric

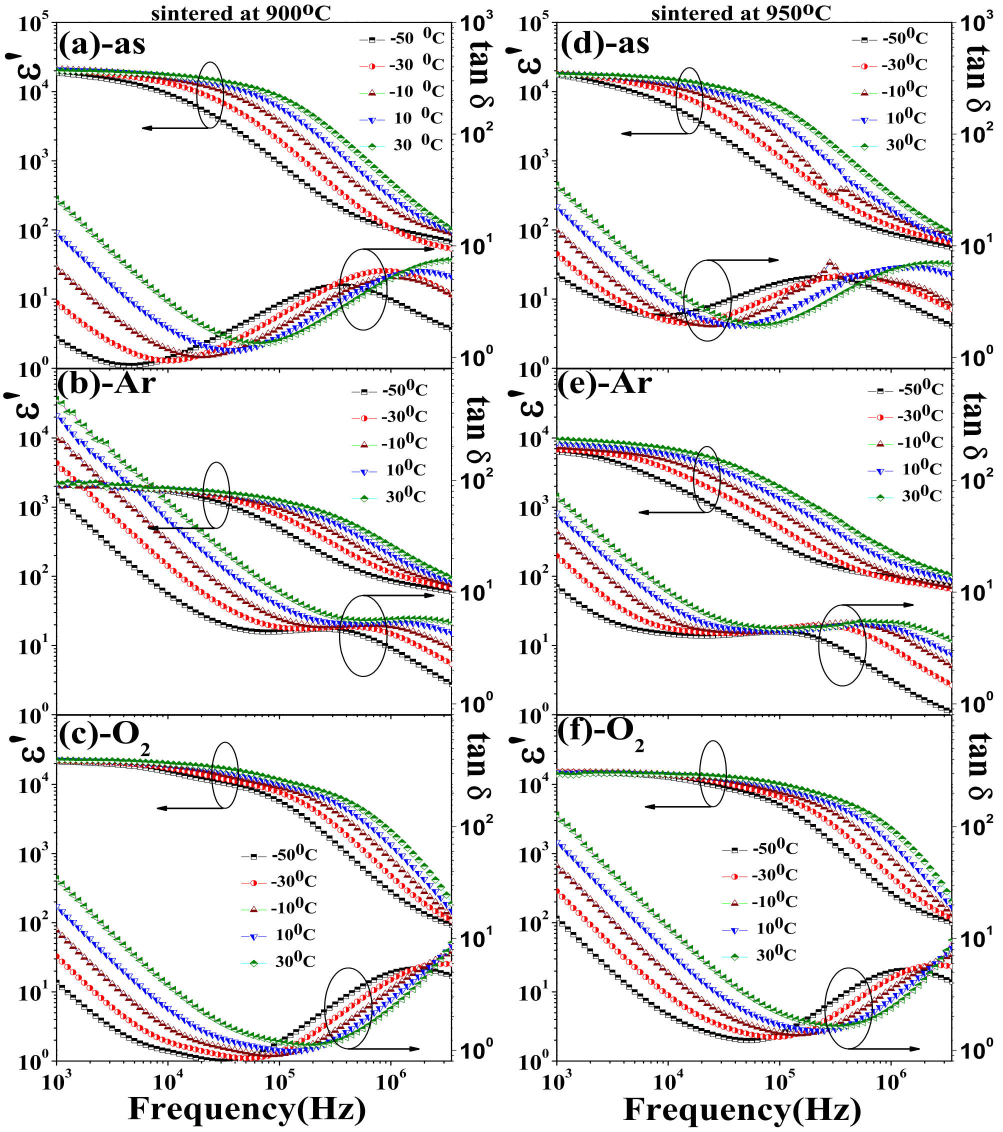

Figure 6.1 Frequency dependence of the dielectric constant (left axis) and the dielectric loss tangent (right axis) for the as-CuO-99.99a (a), Ar-CuO-99.99a (b), O_2-CuO-99.99a (c), as-CuO-99.99b (d), Ar-CuO-99.99b (e) and O_2-CuO-99.99b (f) samples, respectively.

relaxation time can be obtained by the Arrhenius law,

$$\tau = \tau_0 \exp(\frac{E_\tau}{k_B T}) \ , \tag{6.3}$$

where τ_0 is the prefator, E_τ is the activation energy required for the relaxation process, k_B is the Boltzmann constant, and T is the absolute temperature. The

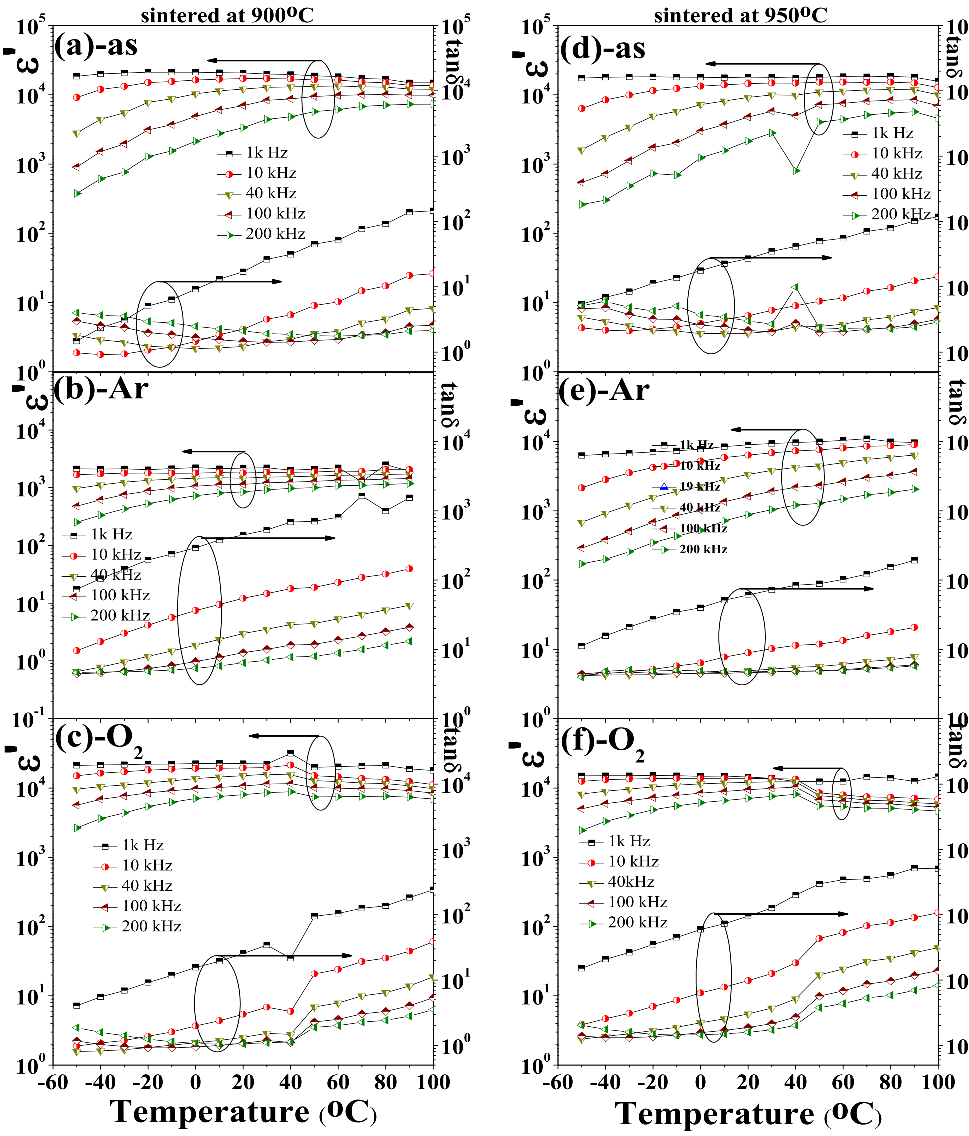

Figure 6.2 Temperature dependence of the dielectric constant (left axis) and the dielectric loss tangent (right axis) for the as-CuO-99.99a (a), Ar-CuO-99.99a (b), O_2-CuO-99.99a (c), as-CuO-99.99b (d), Ar-CuO-99.99b (e) and O_2-CuO-99.99b (f) samples, respectively.

fitted curves using Eq. (6.3) for the as-, Ar-, O_2-CuO-99.99a and the as-, Ar-, O_2-CuO-99.99b samples are shown in the inset of Figures 6.3 (a-1) to (c-1) and the inset of Figures. 6.3 (d-1) to (f-1), respectively. The values of activation energy (E_τ) are obtained to be 0.146, 0.118, 0.113 (1) and 0.106 (2) eV for the as-, Ar-, O_2-CuO-99.99a, respectively. Similarly, the E_τ values for the as-, Ar-, and O_2-

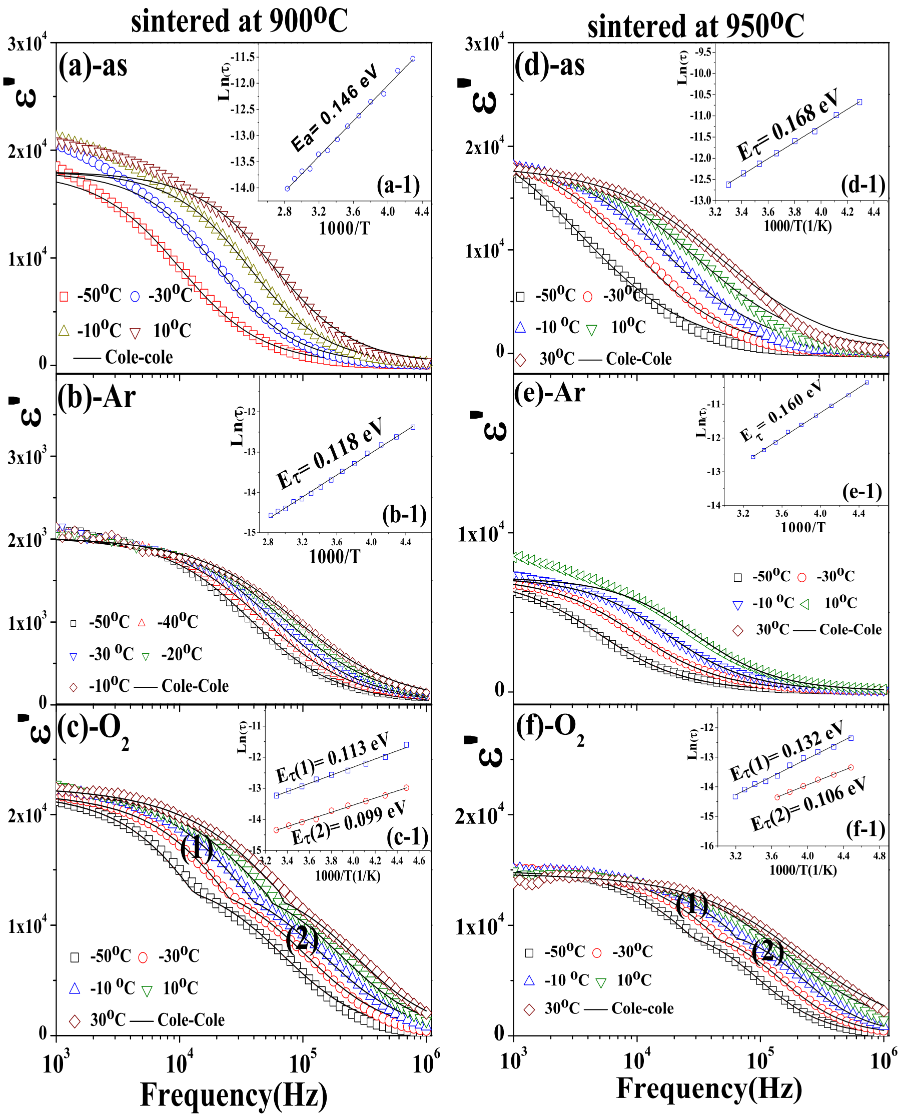

Figure 6.3 The frequency dependence of ε' at various temperatures (the solid lines represent calculated values of Cole-Cole equation) and the Arrhenius plots of dielectric relaxation time, the inset (a-1) to (f-1) for the as-CuO-99.99a (a), Ar-CuO-99.99a (b), O_2-CuO-99.99a (c), as-CuO-99.99b (d), Ar-CuO-99.99b (e) and O_2-CuO-99.99b (f) samples, respectively.

CuO-99.99b samples are obtained to be 0.168, 0.160, 0.132 (1) and 0.106 (2)eV, respectively. The estimated values of activation energy (E_τ) of these samples are summarized in column 7 and 8 of Table 6.2.

Table 6.1 Relaxation times of the as-, Ar-, O_2-CuO-99.99a and the as-, Ar-, O_2-CuO-99.99b samples in the range from -50°C to 30°C.

Temperature	CuO-99.99a				CuO-99.99b			
$(^\circ C)$	as-τ	Ar-τ	O_2-$\tau(\mu s)$		as-τ	Ar-τ	O_2-$\tau(ms)$	
	(μs)	(μs)	(1)	(2)	(μs)	(μs)	(1)	(2)
-50	15.8	5.2	9.2	2.3	46	32	4.3	1.6
-40	9.8	3.8	6.2	1.8	23	21.8	3.2	1.25
-30	7.78	3.2	5	1.5	17	16	2.7	1.06
-20	5	2.3	4	1.29	11.6	12	2.2	0.85
-10	4.3	1.8	3.5	1.1	9.2	9.1	1.73	0.7
0	3.3	1.4	3	0.84	6.9	7.4	1.2	0.58
10	2.7	1.4	2.4	0.76	5.4	5.4	1	-
20	2.1	0.95	2.1	0.68	4.3	4.3	0.91	-
30	1.7	0.81	1.8	0.59	3.3	3.5	0.76	-

6.1.2 The impedance analysis

In order to understand the responses of the dielectric dispersion for the CuO-99.99 samples, the complex impedance analysis was performed. The complex impedance analysis has been known to be able to distinguish the resistance between grain and GBs (Sinclair and West, 1989), by using the complex impedance analysis. Their experiment can be distinguished the resistance for the external (surface layer and electrode) at low frequency and the internal (grain and GBs) at high frequency. On the basis of the impedance spectroscopy (IS) model (Ming et al., 2009), the equivalent circuit is in series with the parallel RC element of the external and internal, and the position of the arc in the frequency spectrum depends on their relaxation time, τ, where $\tau = RC$ (R = resistance, C = capacitance), because at the arc maximum the relationship $\omega_{\max}\tau = 1$ holds, where ω is the angular frequency ($\omega = 2\pi f, f$ is the applied frequency).

For the CuO samples prepared from the commercial CuO powder, the complex impedance, Z^*, plots for the as-samples sintered at 900°C and 950°C (as-

CuO-99.99a and as-CuO-99.99b) are shown in Figures 6.4 (a) and (d). For the measuring temperature between -50°C to 30°C, both samples show a large semi-circular arc with a small semi-circular arc (Figures 6.4 a and 6.4 d). All data were interpreted using an equivalent circuit of two parallel RC elements connected in series, as examined previously. One element corresponds to the internal (RC)int at high frequency, whereas other elements correspond to the external (RC)ext at low frequency (Ming et al., 2009).

When the temperature is increased from -50°C to 30°C, the R_{int} and R_{ext} decrease from 5,700 Ω to 680Ω and 74,000Ω to 2,880Ω; from 6,500Ω to 890Ω and 14,000Ω to 2,120Ω for the as-CuO-99.99a and as-CuO-99.99b samples respectively.

Next, the complex impedance, Z^*, plane plots for the Ar-CuO-99.99a and Ar-CuO-99.99b at measuring temperature between -50°C to 0°C are shown in Figures 6.4 (b) and 6.4 (e), respectively. When the temperatures are increased from -50°C to 30°C, the R_{int} and R_{ext} are decreased from 7,100Ω to 1,860Ω and 4,500Ω to 900Ω for the as-CuO-99.99a; from 13,400Ω to 3,000Ω and 13,200Ω to 2,900Ω for the as-CuO-99.99b.

In the final part of Figure 6.4, we discuss the dielectric behavior of the CuO-99.99 after re-annealing in oxygen at 700°C for 2 h. The complex impedance, Z^*, plane plots for the O_2-CuO-99.99a and O_2-CuO-99.99b at measuring temperatures between -50°C to 0°C are shown in Figures 6.4 (c) and 6.4 (f), respectively. When the temperature is increased from -50°C to 0°C, the R_{int} and R_{ext} decrease from 1,300Ω to 432Ω and 20,700Ω to 4,586Ω for the as-CuO-99.99a; from 1,358Ω to 420Ω and 6,567Ω to 1,626Ω for the as-CuO-99.99b, respectively.

The complex impedance, Z^*, plane plot of the as-CuO-99.99a and as-CuO-99.99b shown in Figures 6.4 (a) and 6.4 (d), which reveal two semicircles intercept on the Z' axis at low and high frequencies correspond to external resistance (R_{ext})

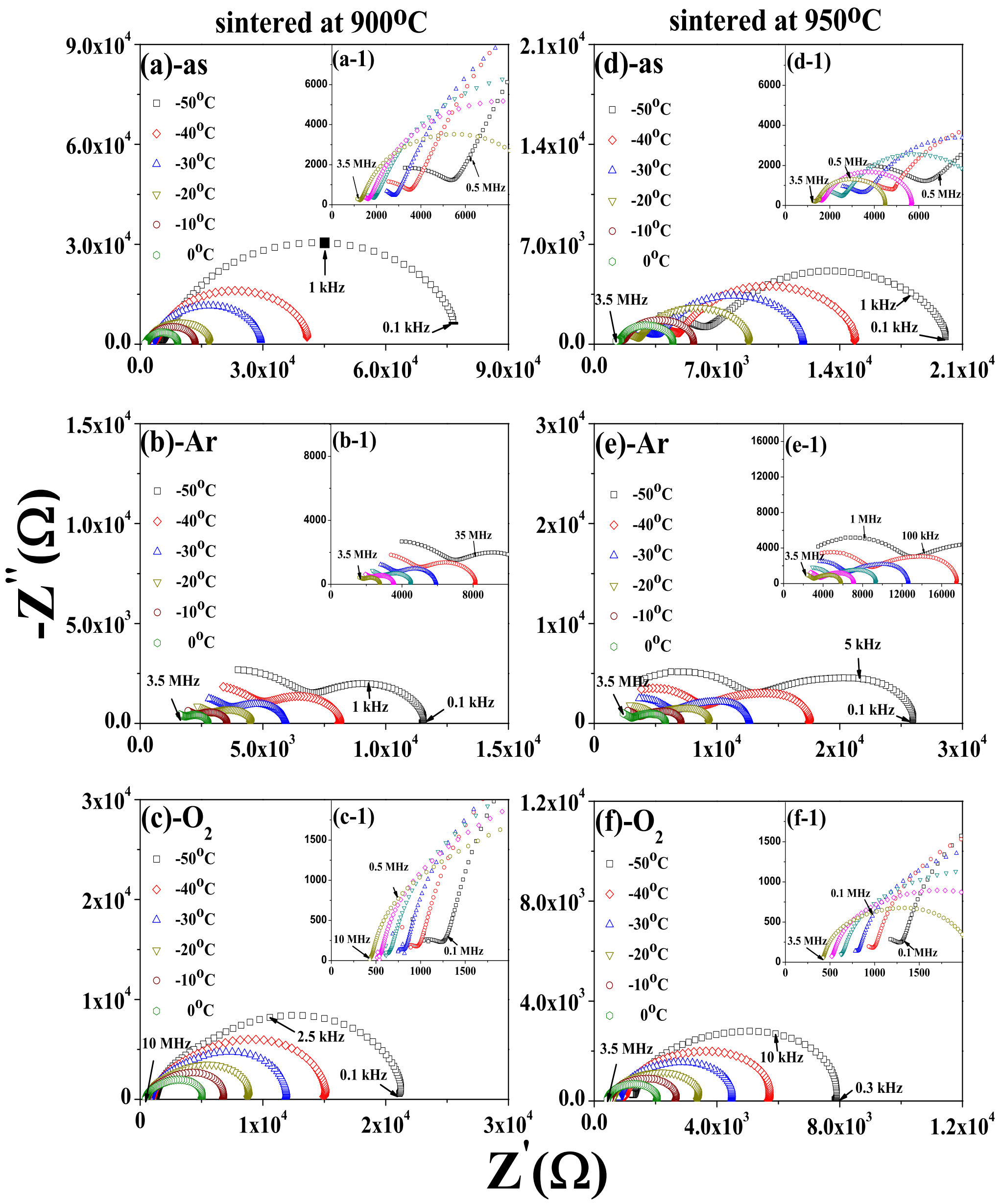

Figure 6.4 Complex impedance, Z^* plots and the expanding scale at a high frequency (inset) for the as-CuO-99.99a (a), Ar-CuO-99.99a (b), O_2-CuO-99.99a (c), as-CuO-99.99b (d), Ar-CuO-99.99b (e) and O_2-CuO-99.99b (f) ceramics, respectively.

and internal resistance (R_{int}). Then the external resistance of both samples decreases after annealed at 700°C for 2h in argon (Figures 6.4 (b) and 6.4 (e)). This may be due to the decrease of the charge carrier because of the increase in the

Table 6.2 The dielectric constant, dielectric loss tangent activation energy, capacitance and resistance of internal (R_{int}), external (R_{ext}) of the commercial powder-prepared CuO samples at 30°C and 1 kHz.

Samples	Dielectric (ε')	tanδ	Resistance (Ω)		Capacitance (nF)	Activation Energy (eV)	
			$R_{\rm ext}$	$R_{\rm int}$	$C_{\rm ext}(1)(2)$	$E_{\tau 1}$	$E_{\tau 2}$
as-CuO-99.99a	19,900	26.3	2,880	680	2.98	0.146	-
Ar-CuO-99.99a	2,220	529	490	1060	0.32	0.118	-
O_2-CuO-99.99a	22,300	34.3	1,995	296	3.39(1.52)	0.113	0.099
as-CuO-99.99b	17,800	34.9	2,120	890	2.61	0.168	-
Ar-CuO-99.99b	9,380	72.2	1,260	1450	1.5	0.16	-
O_2-CuO-99.99b	13,800	127	744	256	2.1(0.91)	0.132	0.106

oxygen vacancies and the reduction of the surface due to the polishing mechanism, corresponding to the reduction of the dielectric constant and the increase of the dielectric loss tangent (Figure 6.1 (b) for the CuO-99.99a and Figure 6.1 (e) for the CuO-99.99b samples, respectively). After re-annealing in oxygen, the complex impedance, Z^*, plane reveals one semicircle with a non-zero intercept on the Z' axis at high frequencies and one semicircle at low frequencies corresponding to the internal and external part, respectively. The semicircle at low frequency corresponding to the resistance of electrode collapses with the new surface layer (occuring by the polish surface samples and re-annealing in oxygen) as clearly seen in Figures 6.1 (c) and 6.1 (f). The insets (a-1) to (f-1) of the Figure 6.1 show the impedance, Z^*, plane plot at a high frequency of the samples.

Figures 6.5 (a) and 6.5 (b) show comparison of the dielectric constant for the as-, Ar-, O_2-CuO-99.99a and as-, Ar-, O_2-CuO-99 samples measured at room temperature over the frequency range of 1 kHz and 1 MHz. In Figure 6.5 (a), the ε' at 1 kHz is 19900 for the as-CuO-99.99a and is decreased to 2220 for the Ar-CuO-99.99a sample. However, the ε' can be recovered to around initial value of 22,300 for the O_2-CuO-99.99a sample. Similar result was observed for the samples sintered at 950°C (Figure 6.5 (b)). The ε' value at 1 kHz is 17800 for the as-CuO-

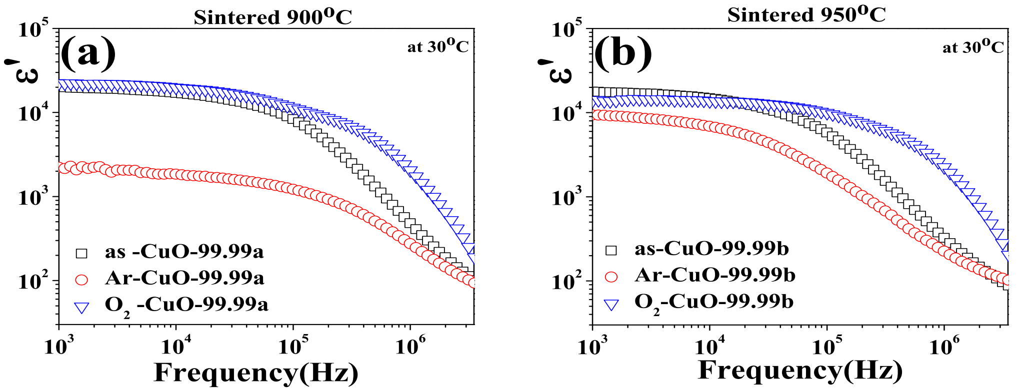

Figure 6.5 Comparison of frequency dependence of the dielectric constant at room temperature for the as-, Ar- and O_2-CuO-99.99a (a); as-, Ar- and O_2-CuO-99.99b (b), respectively.

99.99b and after that decreases to 9380 for the Ar-CuO-99.99b sample. However, the ε' can be recovered up to 13800 for the O_2-CuO-99.99b. This enhancement of the ε' of these sample is possibly due to the charge carrier in the sample, where the high dielectric constant in the as-samples is due to the exist of charge carrier in the samples during the sintering process. And, the ε' value is decreased due to the decrease of the charge carrier in the Ar-samples. Then, after re-annealing in oxygen the dielectric constant can be increased again due to the increasing of charge carrier.

Figure 6.6 shows the plots of the dielectric constant (ε'), dielectric loss tangent external resistance (R_{ext}) and internal resistant (R_{int}) as a function of sintering temperature for the as-, Ar- and O_2-CuO-99.99 samples. In Figure 6.6 (a) the dielectric constant, ε', of the as-samples sintered at 900°C is higher than that of the samples sintered at 950°C, whereas the tanδ values of both samples are not different (Figure 6.6 (b)). In Figure 6.6 (c), the R_{ext} of the as-sample sintered at 900°C is higher than that of the samples sintered at 950°C. Finally, the

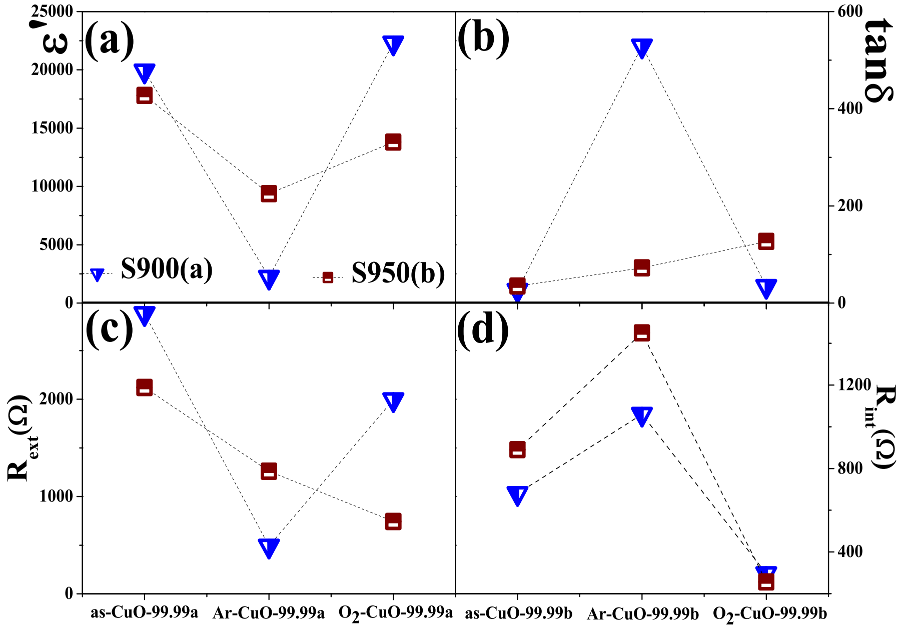

Figure 6.6 The plots of (a) the dielectric constant, (b) the dielectric loss tangent, (c) the external resistance (R_{ext}), and (d) the internal resistance (R_{int}) for the as-, Ar- and O_2-sample sintered 900°C (▽) and 950°C (□), respectively.

R_{int} of the as-samples sintered at 900°C is lower than that of the samples sintered at 950°C. Then, in Figure 6.6 (b) the tanδ values of both samples increase again corresponding to the decrease in dielectric constant, ε'. Clearly, the ε' decreases with decreasing in R_{ext} (due to, i. the charge carrier in the samples decreased after annealing in argon, ii. The surface layer decreased by the polishing as seen in Figures 6.6 (a) and 6.6 (c) (point Ar-CuO-99.99). After annealing in oxygen (point O_2-CuO-99.99), the ε' can be increased again in corresponding with the decrease in the tanδ, the increase in the R_{ext} and the decrease in the R_{int}, due to the decrease of the oxygen vacancies and the formation of the new surface layer which gives rise to smaller resistance value than the old surface layer.

6.1.3 Effect of dc-bias voltage

Figure 6.7 shows frequency dependence of the dielectric constant as a function of dc-bias voltage (0 - 3.6 V) for the as-samples sintered at 950°C (as-CuO-99.99a) (a) and the as-samples sintered at 900°C (as-CuO-99.99b) (b), respectively. The dielectric constants decrease from 23700 to 3090 and 21200 to 8830 at 1 kHz with increasing the dc-bias voltage (0 - 3.5 V) for the as-CuO-99.99a and as-CuO-99.99b, respectively. Figures 6.7 (c) and 6.7 (d) show the dc-bias voltage dependence of dielectric constant as a function of (1 kHz - 20 kHz) frequencies for the as-CuO-99.99a and as-CuO-99.99b, respectively. It is clearly seen in Figures 6.7 (c) and 6.7 (d) that the dielectric constant is slightly decreased when the dc- bias voltage is increased from 0 to 3.6 V. In addition, the capacitance of external response is decreased from 2.4 nF to 2.1 nF and 2.5 nF to 2.1 nF for the as-CuO-99.99a and as-CuO-99.99b, respectively. Whereas, the capacitance of internal response remains constant with the values of 2.0 pF and 2.1 pF for the as-CuO-99.99a and as-CuO-99.99b, respectively.

Figures 6.8 (a) and 6.8 (b) show the complex impedance, Z^*, plots, containing large semicircles corresponding to the external response at low frequencies from 2.8 kHz to 5.0 MHz for the as-CuO-99.99a and to 1.5 MHz for the as-CuO-99.99b, and small semicircles corresponding to the internal response at high frequencies. As can be seen that at room temperature, the R_{ext} and the dielectric constant are decreased with the increase of the dc-bias voltage from 0.3 to 6 V. The R_{ext} decreases from 5600 Ω to 510 Ω and 3200 Ω to 250 Ω for the as-samples sintered at 900°C and 950°C, respectively, when the dc-bias voltage is increased from 0 to 3 V, whereas the R_{int} remains constant at 911 Ω and 1066 Ω, respectively. In this study, the capacitance bridge is not balanced at voltages over 3.6 V due to the large leakage current. When the dc-bias is over the balancing limit, the charge carriers

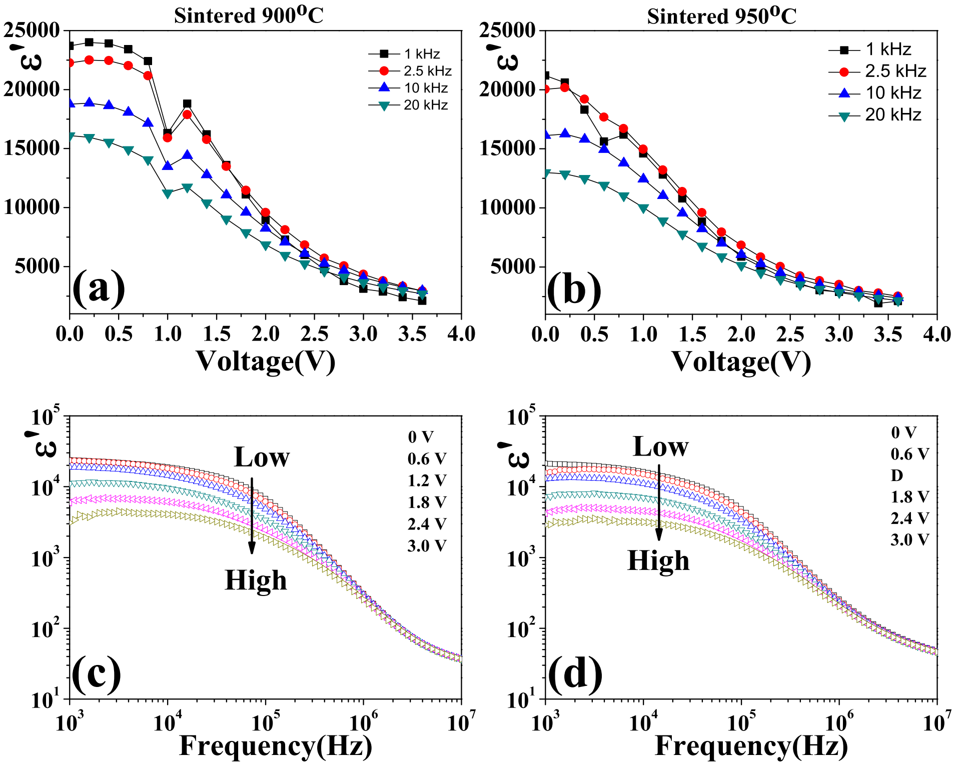

Figure 6.7 Frequency dependence of the dielectric constant as a function of dc-bias voltage (0 - 3.6) near room temperature at 1 kHz for the (a) as-CuO-99.99a and (b) as-CuO-99.99b sample, (c) and (d) show the plot of the dielectric constant versus frequencies for the as-CuO-99.99a and as-CuO-99.99b sample, respectively.

can be transported across potential wall of the external part, thus the free charges accumulated at the external part (interfacial polarization) are disappeared, and then the total polarization is only contributed by the internal part. Part of the decrement in ε' value due to the influence of the dc-bias is probably contributed by the external free charge, and the remaining value of ε' after the dc-bias voltage over the balancing limit is contributed by internal free charge. Therefore, the dc-bias voltage should have effect on the electrical properties of the external free charge, whereas it has no effect on the by internal free charge.

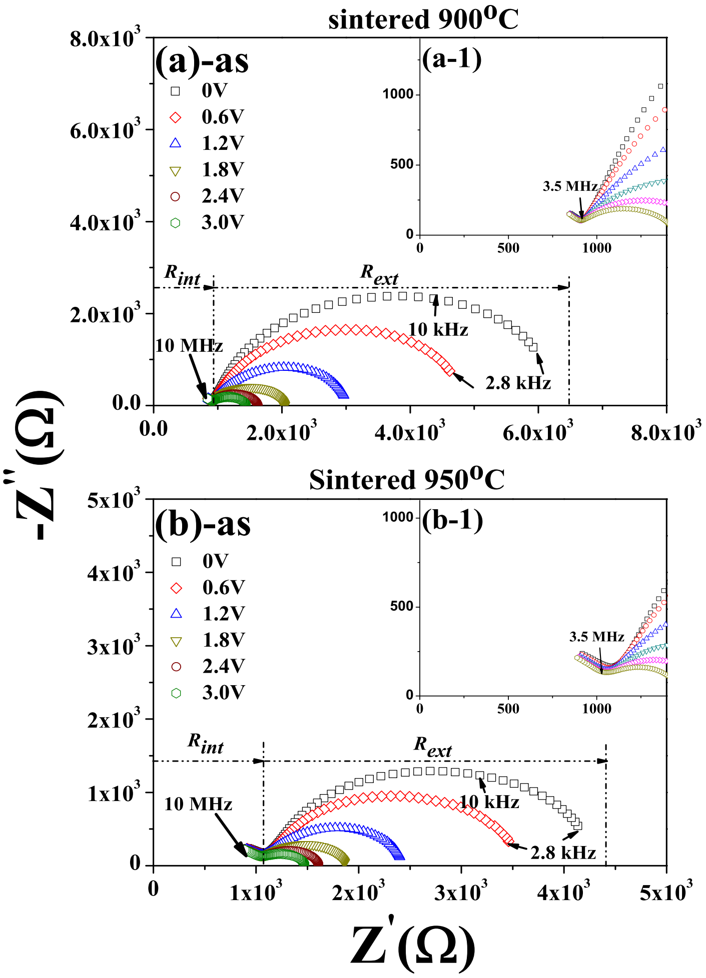

Figure 6.8 Complex impedance, Z^*, plots and the expanding scale at a high frequency (inset) at each dc-bias voltage (0 - 3 V.) at room temperature for the as-CuO-99.99a (a) and as-CuO-99.99b (b), respectively.

6.1.4 Effect of uniaxial compressive stress

For better understanding on the effect of the dc-bias voltage on the electrical properties (ε' and tanδ), the effect of uniaxial compressive stress on the ε' and tanδ of the as-samples was studied. Figure 6.9 (a) and (b) and Figure 6.9 (c) and (d) show the stress dependence of the dielectric constant (ε') and dielectric loss tangent (tanδ) at the frequencies of 1 - 10 kHz for the as-CuO-99.99a and as-CuO-99.99b, respectively. There is a significant change of both, the dielectric constant and dielectric loss tangent of these ceramics when applied uniaxial compressive stress. The changes in the dielectric constant of both samples with the applied stress can be divided into two regions. For the as-CuO-99.99a ceramics at 1 kHz (Figures 6.9 (a) and 6.9 (c)), the dielectric constant is increased with increasing the applied stress from 0 to 80 MPa (region 1) and has the maximum value of 2.5×10^5 at 80 MPa, and the dielectric loss tangent is also increased to the maximum value of 22 at 80 MPa. After reaching the maximum, both ε' and tanδ decrease to 1.8×10^5 and 14 at 110 MPa (region 2), respectively. Similarly, the ε' and tanδ of the as-CuO-99.99b, as shown in Figure 6.9 (b) and (d), are significantly increased to the maximum values of 3.6×10^5 and 43 at 45 MPa (region 1), respectively. They are then decreased to the minimum values of 5×10^4 and 20 at 100 MPa, respectively. After that the ε' and the tanδ seem to be independent of the stress up to 125 MPa. The large ε' of both samples, which occurs in region 1, causes a sudden change in the electrode capacitance due to the uniaxial compressive stress. Because of the elasticity of the thin electrodes, when the compressive stress is applied the ε' is easily increased to the maximum value and it is then decreased towards the end of the region 1 causing the change in the electrode's structure. For the same reason, the internal capacitance can be effected by the apply stress (region 2) and this can also be applied for the discussion on the dc-bias results (Figure 6.8) because the dc-bias effect is somewhat similar to compressive stress. However, the much difference between the two applied external forces (stress vs dc-bias) is the mechanical stress that causes the change in the electrode's structure. Hence a strong increase in the dielectric properties, whereas the dc-bias (in this case is very small (0 - 3.6 V) only causes the change within the internal capacitance (grain and GBs). As a result, the decrease in the properties is observed.

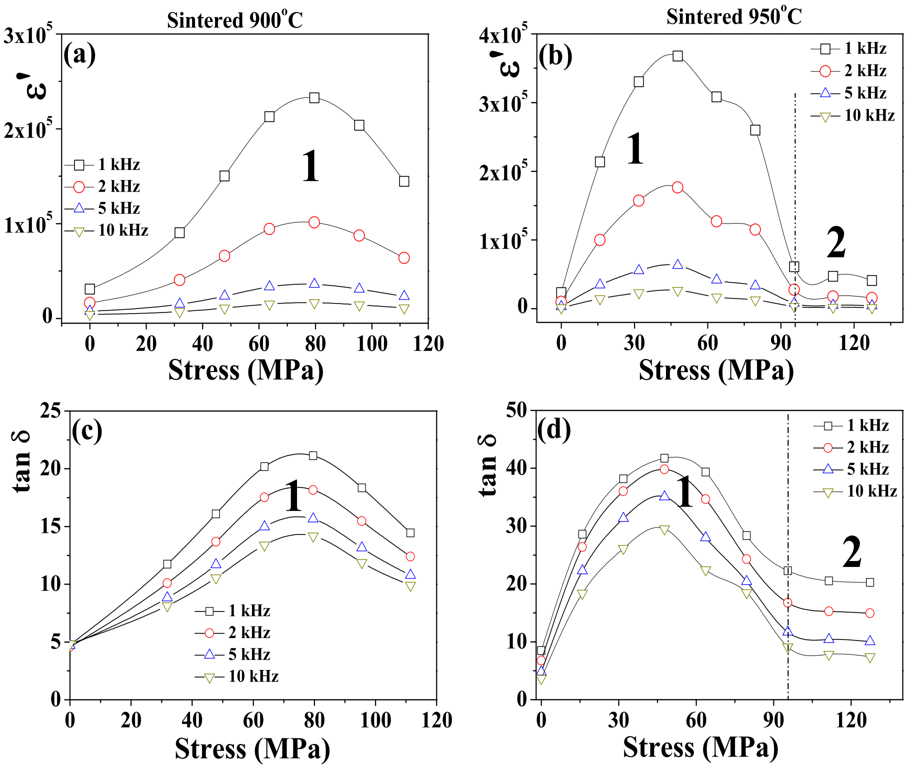

Figure 6.9 Effect of compressive stress on the dielectric constant ((a) and (b)) and dielectric loss tangent ((c) and (d)) at room temperature for the as-CuO-99.99a and as-CuO-99.99b.

6.2 Electrical properties of the CuO ceramics prepared by the DT method

The dielectric behavior as functions of frequency and temperature together with relaxation behavior for the as-, Ar- and O_2-sample sintered at 900°C and 950°C are examined in the first section. The next section is dealed with the impedance spectroscopy model (IS model) used to study the electrical properties of these samples. The effect of the dc-bias voltage and uniaxial compressive stress on the dielectric constant and tanδ are discussed in the last section.

6.2.1 Dielectric properties

Figure 6.10 demonstrates the frequency dependence of the dielectric constant (left axis) and the dielectric loss tangent (right axis) for the sample prepared from the powder calcined at 500°C and sintered at 900°C and 950°C (the as-samples ((a) and (d)), Ar-samples ((b) and (e)) and O_2-samples ((c) and (f))), respectively. Figures 6.10 (a) and 6.10 (d) show the giant dielectric of $(3.39 - 4.7) \times 10^4$ and $(3.38 - 4.6) \times 10^4$ with the tanδ values of $(8.9 - 46.5) \times 10^4$ and (8.8 - 4.6) for the as-CuO5-DTa and as-CuO5-DTb, respectively. The values of dielectric constant decreased to $(1.2 - 1.4) \times 10^4$ and $(1.8 - 1.9) \times 10^4$, whereas the values of tanδ are increased to (8.9 - 200) and (9 - 185) for the Ar-CuO5-DTa and Ar-CuO5-DTb (Figures 6.10 (b) and 6.10 (e)). However, the dielectric constant can be increased to the values of $(1.9 - 2.27) \times 10^4$ and $(2.45 - 3.09) \times 10^4$, whereas the tan$\delta$ is decreased to the values of (8.92 - 46.5) and (8.81 - 45.9) for the O_2-CuO5-DTa and O_2-CuO5-DTb samples, respectively (Figures 6.10 (c) and 6.10 (f)).

Figures 6.11 (a) - (f) show the frequency dependence of the dielectric constant (left axis) and dielectric loss tangent (right axis) for the samples prepared from the powder calcined at 600°C and sintered at 900°C and 950°C (the as-sample ((a) and (d)), Ar-sample ((b) and (e)) and O_2-sample ((c) and (f))), respectively . The ε' and tanδ values of the as-CuO6-DTa and as-CuO6-DTb as shown in Figures 6.11 (a) and (d) are $(1.77 - 6.89) \times 10^4$ and $(1.21 - 1.61) \times 10^4$ and (21.9 - 30.4) and (1.78 - 4.79), respectively. After that the ε' values decrease to $(1.43 - 1.57) \times 10^4$ and $(1.27 - 1.61) \times 10^4$, while the tan$\delta$ values increase to (5.78 - 13.9) and (5.54 - 10.7) for the Ar-CuO6-DTa and Ar-CuO6-DTb (Figures 6.10 (b) and 6.10 (e)), respectively. However, the giant dielectric constant can be increased to $(2.63 - 96.25) \times 10^4$ and $(1.74 - 2.17) \times 10^4$, whereas the tan$\delta$ values are (6.41 -

72.3) and (9.28 - 96.25) for the O_2-CuO6-DTa (Figure 6.10 (c)) and O_2-CuO6-DTb (Figure 6.10 (f)), respectively.

Figures 6.12 (a) - (f) show the frequency dependence on the ε' (left axis) and the tanδ (right axis) for the samples prepared from the powder calcined at 700°C and then sintered at 900°C and 950°C, respectively. Figures 6.12 (a) and 6.12 (d) show respectively that the values of ε' and tanδ are $(3.07 - 3.89) \times 10^4$ and $(4.61 - 5.08) \times 10^4$; (5.54 - 41.10) and (3.78 - 13.0) for the as-CuO7-DTa and as-CuO7-DTb. After that the ε' values decrease to $(1.68 - 1.94) \times 10^4$ and $(1.47 - 1.78) \times 10^4$, whereas the tan$\delta$ values increase to (4.08 - 8.29) and (11.3 - 287) for the Ar-CuO7-DTa and Ar-CuO7-DTb (Figures 6.12 (b) and 6.12 (e)), respectively. Then, the ε' and tanδ values can be increased for the O_2-CuO7-DTa and O_2-CuO7-DTb (Figures 6.12 (c) and 6.12 (f)). As observed in Figures 6.10 - 6.12 ((a) - (f)) the dielectric constant and the dielectric loss tangent behavior of the as-, Ar- and O_2-samples prepared from the powder with different calcined temperature and sintered at 900°C and 950°C are similar to those observed for the as-, Ar-, O_2-samples prepared from the commercial CuO powder as discussed in section 6.1.1.

The temperature dependence of the dielectric constant (left axis) and the dielectric loss tangent (right axis) over the temperature range -50°C to 100°C at each frequency of 1 kHz to 1 MHz for the samples prepared from the powder at 500, 600 and 700°C and sintered at 900°C and 950°C are shown in Figures 6.13, 6.14 and 6.15, respectively. The ε' is independent of the temperature above -50°C at 1 kHz frequency. The relaxation times of all samples shift to the higher temperature side with the increase of the frequency. This indicates that thermally activated relaxation also occurs in the samples similar to those observed in the samples prepared by commercial CuO powder (Sarkar et al., 2006; Thongbai et al., 2008b).

For further understanding on the physical nature of the observed dielectric relaxation behavior of the as-, Ar- and O_2-samples with different sintering temperatures of 900°C and 950°C (Figures 6.13 - 6.15), the data of the dielectric spectra are fitted with the Cole-Cole equation (Eq. 6.1). The results of the as-, Ar-, O_2-samples prepared from the powders calcined at 500, 600 and 700°C and then sintered at 900°C are shown in Figures 6.16 - 6.18 ((a) - (c)). Whereas, Figures 6.16 - 6.18 ((d) - (f)) show the results of the as-, Ar-, O_2-samples sintered at 950°C. Their relaxation times at the temperature between -50°C to 30°C are shown in Tables 6.3 - 6.5. It is clearly seen from Figures 6.16 - 6.18 ((a) - (f)) that the relaxation time can be well fitted with the Cole-Cole equation (Cole and Cole, 1941), indicating that the relaxation time of these samples are the Debye-type relaxation. The values of α (Eq. 6.2) are obtained to be 0.98, 0.91; 0.81(1), 0.88(2) and 0.89; 0.74(1), 0.91(2); 0.81(1), 0.88(2) for the as-, Ar-, O_2-CuO5-DTa (Figures 6.15 (a-c)) and as-, Ar-, O_2-CuO5-DTb (Figures 6.15 (d) - (f)), respectively. Whereas, Figures 6.16 (a) - (f) show that the α values are 0.91, 0.88, 0.92 and 0.94, 0.94, 0.88 for the as-, Ar-, O_2-CuO6-DTa (Figures 6.16 (a) - (c)) and as-, Ar-, O_2-CuO6-DTb (Figures 6.16 (d) - (f)), respectively. Similarly, the well fitted results of the as-, Ar-, O_2-CuO7-DTa (Figures 6.17 (a) - (c)) and as-, Ar-, O_2-CuO7-DTb (Figures 6.17 (a) - (c)) show that the α values are 0.94; 0.67(1), 0.89(2); 0.91 and 0.74(1), 0.88(2); 0.90; 0.89, respectively.

From the fitted results, the τ values at different temperatures (-50°C to 30°C) are obtained as shown in Tables 6.3 - 6.5 for the samples prepared from the powders calcined at 500, 600 and 700°C, respectively. It is clearly seen that the relaxation times of the as-CuO5-DTa, as-CuO6-DTa and as-CuO7-DTa samples are of the same value, while the relaxation times of the Ar-CuO6-DTa samples are

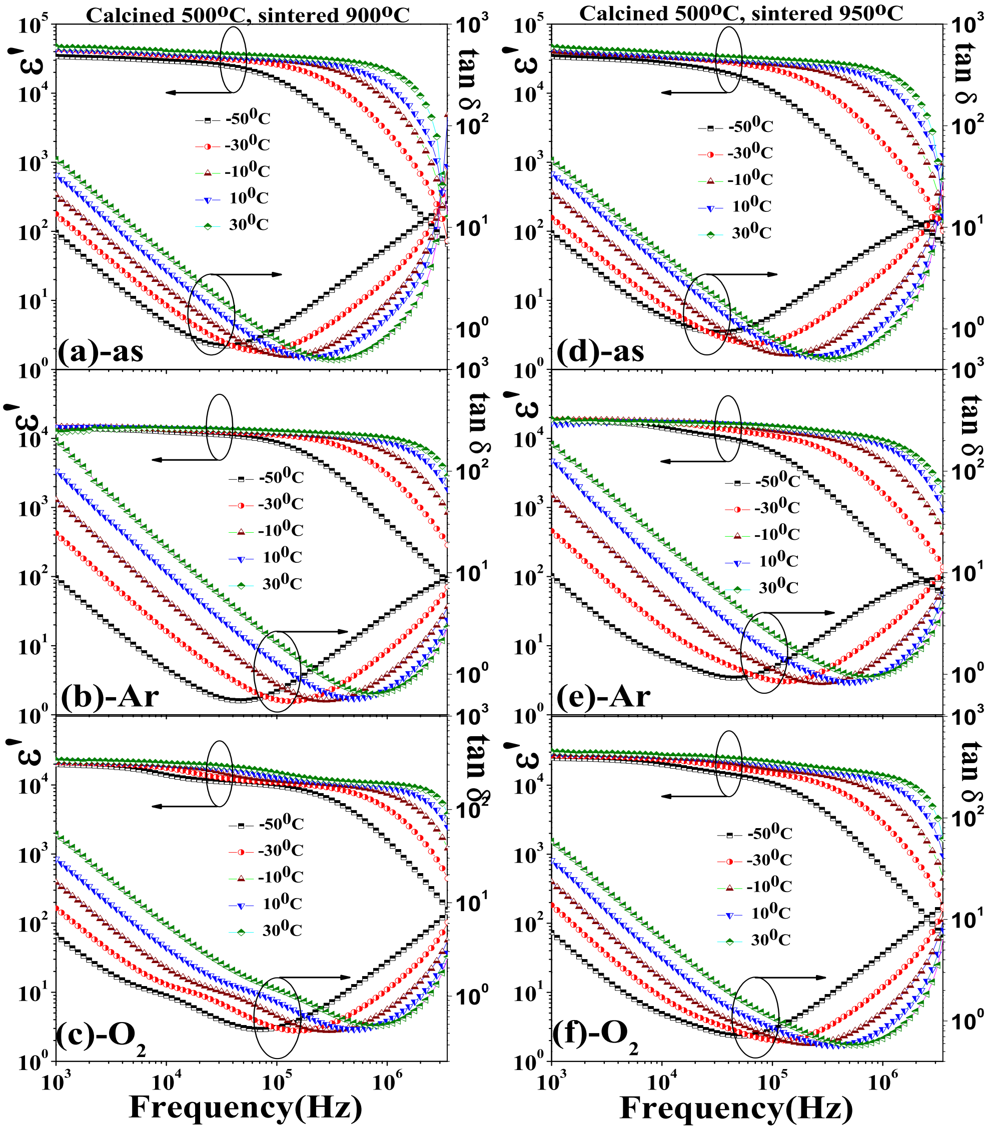

Figure 6.10 Frequency dependence of the dielectric constant (left axis) and dielectric loss tangent (right axis) for the as-CuO5-DTa (a), Ar-CuO5-DTa (b), O_2-CuO5-DTa (c), as-CuO5-DTb (d), Ar-CuO5-DTb (e) and O_2-CuO5-DTb (f) samples, respectively.

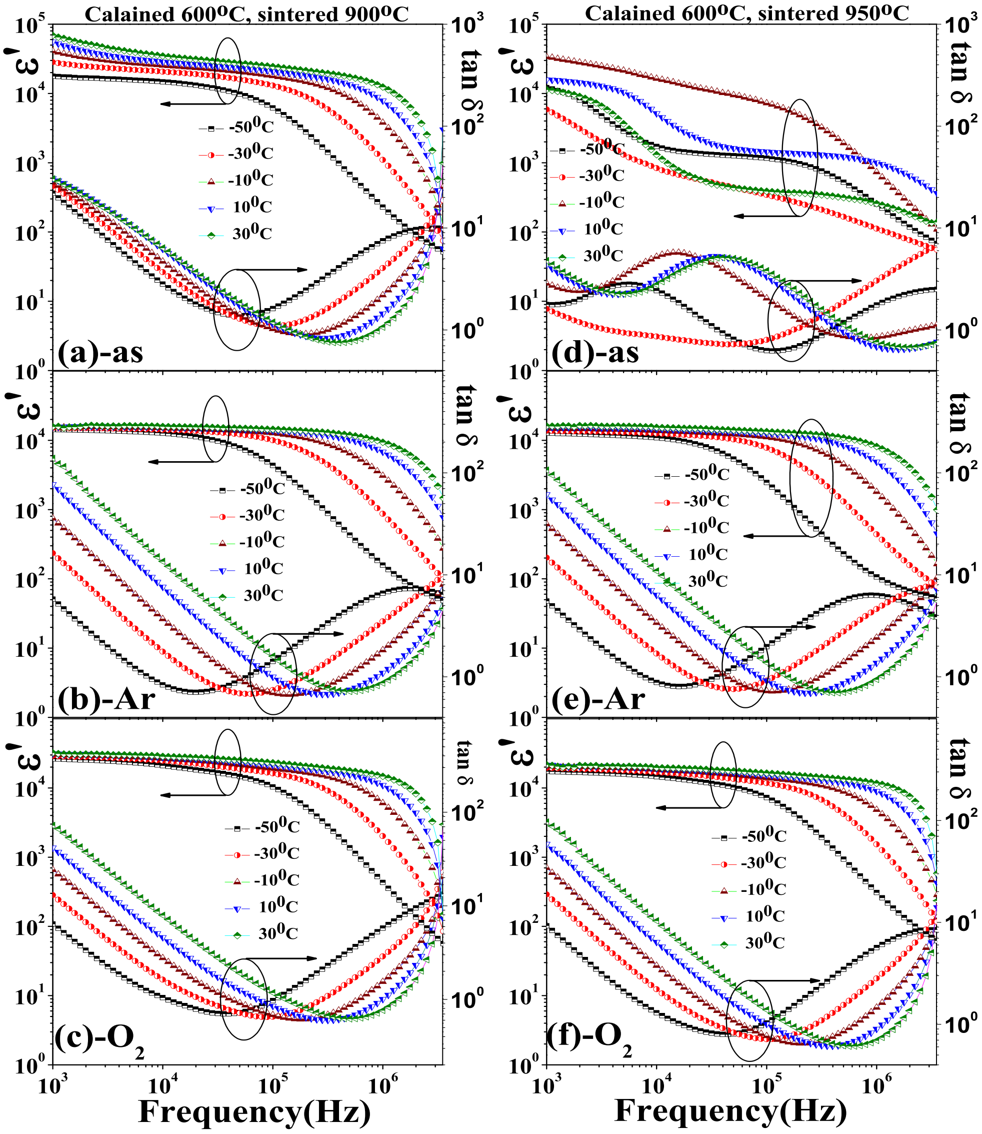

Figure 6.11 Frequency dependence of the dielectric constant (left axis) and dielectric loss tangent (right axis) for the as-CuO6-DTa (a), Ar-CuO6-DTa (b), O_2-CuO6-DTa (c), as-CuO6-DTb (d), Ar-CuO6-DTb (e) and O_2-CuO6-DTb (f) samples, respectively.

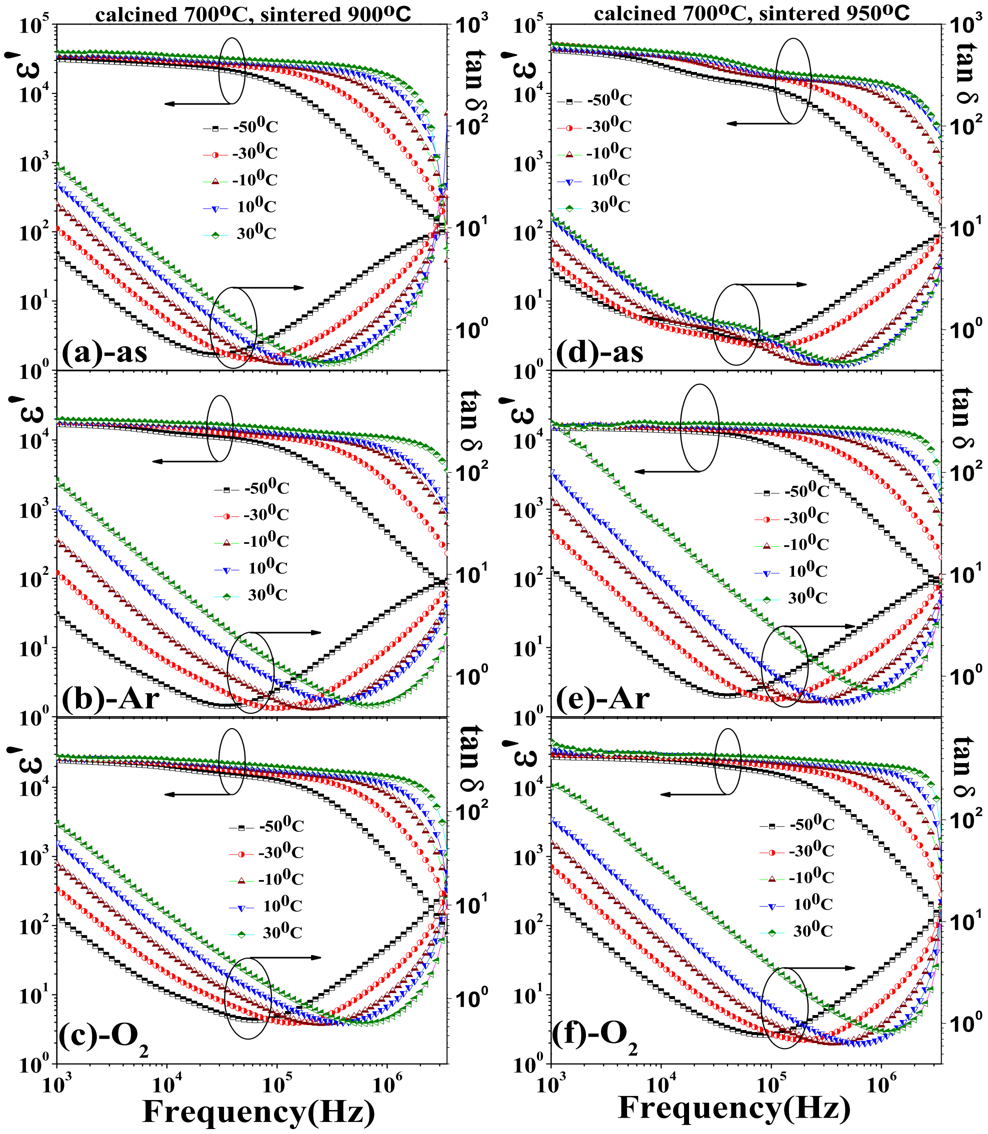

Figure 6.12 Frequency dependence of the dielectric constant (left axis) and dielectric loss tangent (right axis) for the as-CuO7-DTa (a), Ar-CuO7-DTa (b), O_2-CuO7-DTa (c), as-CuO7-DTb (d), Ar-CuO7-DTb (e) and O_2-CuO7-DTb (f) samples, respectively.

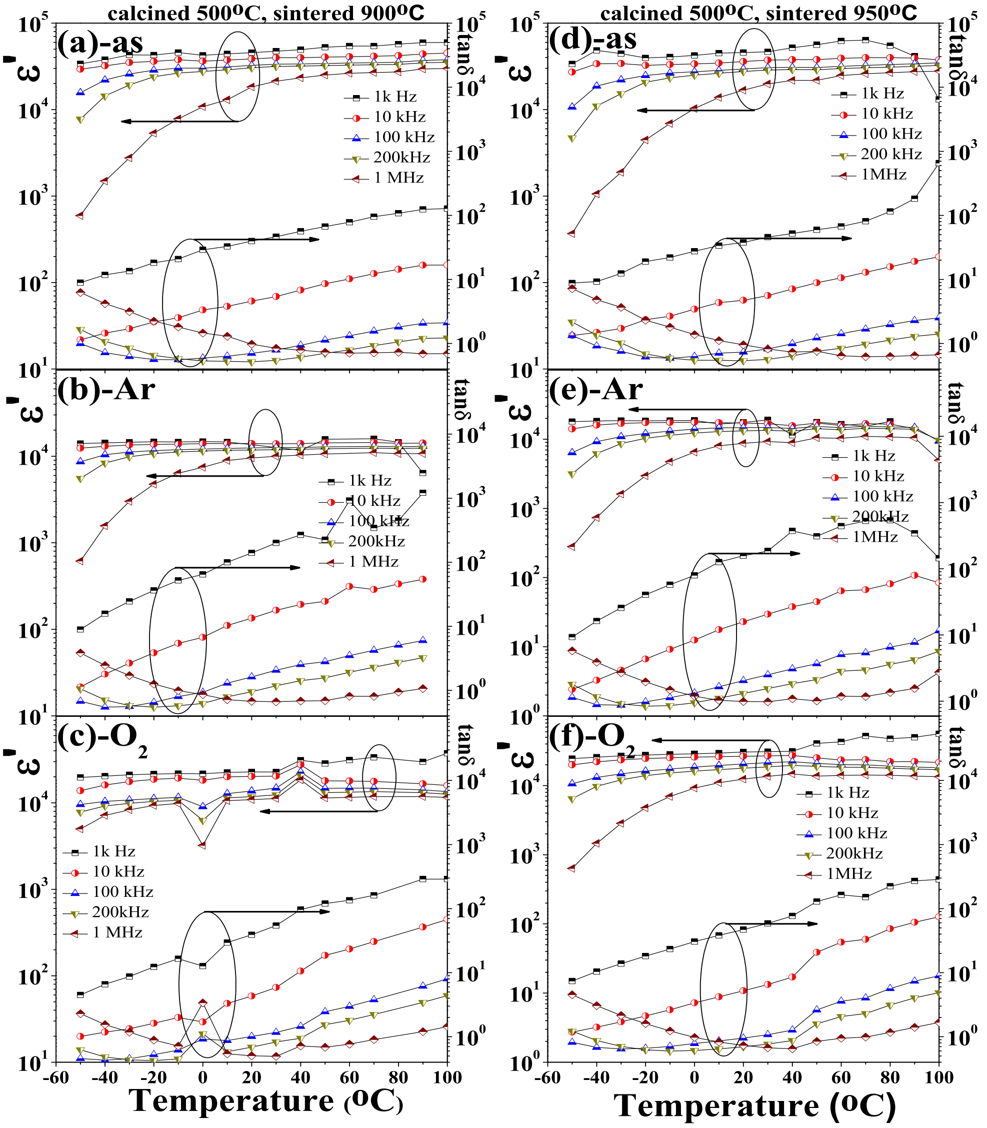

Figure 6.13 Temperature dependence of the dielectric constant (left axis) and dielectric loss tangent (right axis) for the as-CuO5-DTa (a), Ar-CuO5-DTa (b), O_2-CuO5-DTa (c), as-CuO5-DTb (d), Ar-CuO5-DTb (e) and O_2-CuO5-DTb (f) samples, respectively.

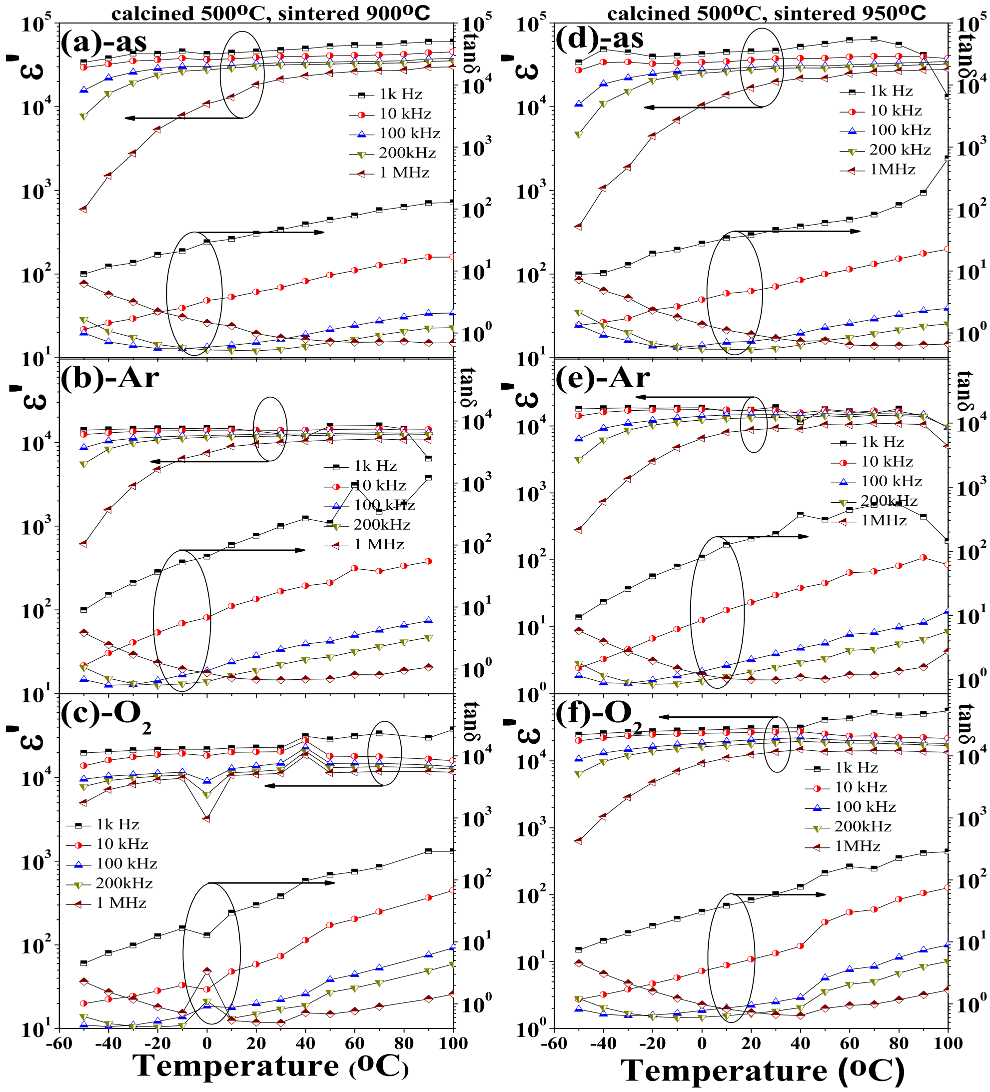

Figure 6.14 Temperature dependence of the dielectric constant (left axis) and dielectric loss tangent (right axis) for the as-CuO6-DTa (a), Ar-CuO6-DTa (b), O_2-CuO6-DTa (c), as-CuO6-DTb (d), Ar-CuO6-DTb (e) and O_2-CuO6-DTb (f) samples, respectively.

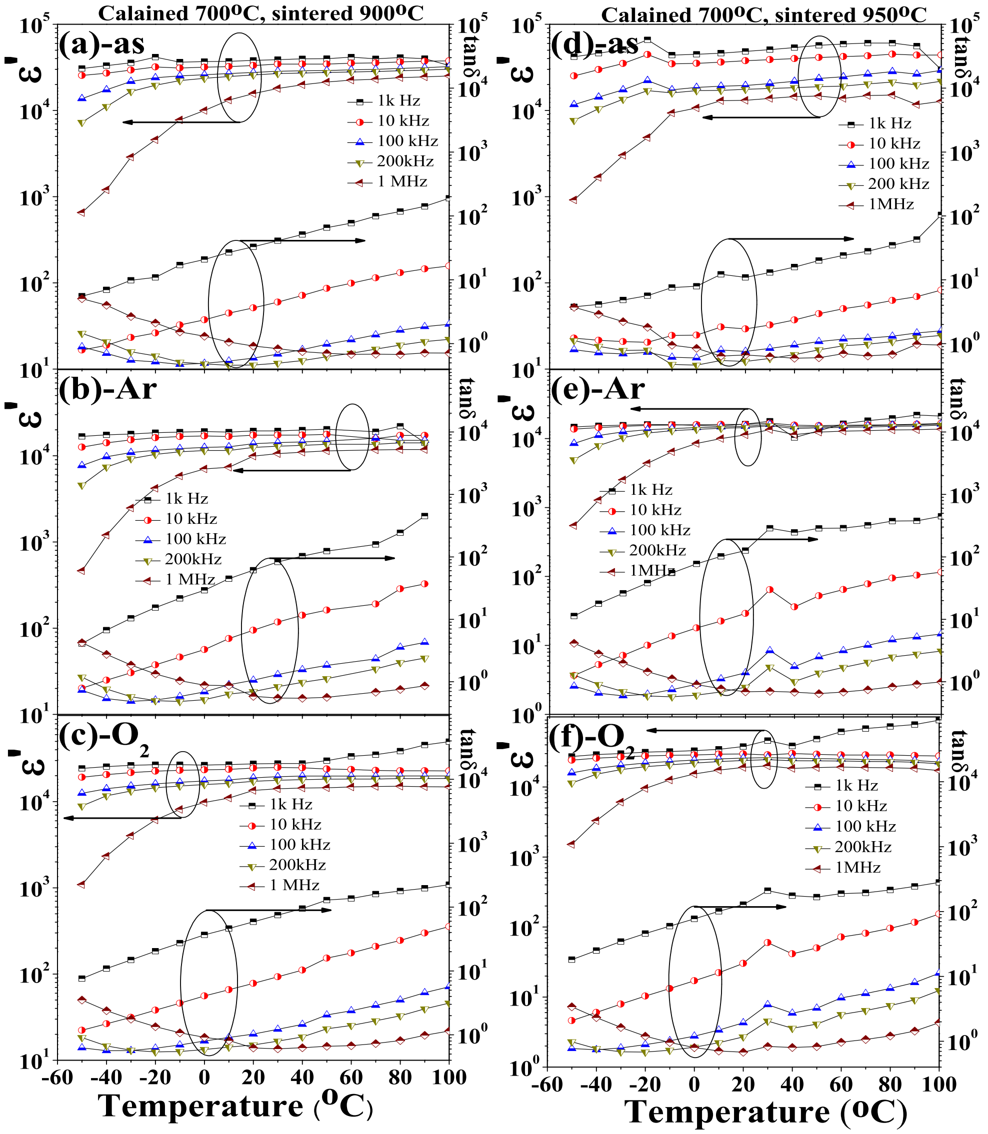

Figure 6.15 Temperature dependence of the dielectric constant (left axis) and dielectric loss tangent (right axis) for the as-CuO7-DTa (a), Ar-CuO7-DTa (b), O_2-CuO7-DTa (c), as-CuO7-DTb (d), Ar-CuO7-DTb (e) and O_2-CuO7-DTb (f) samples, respectively.

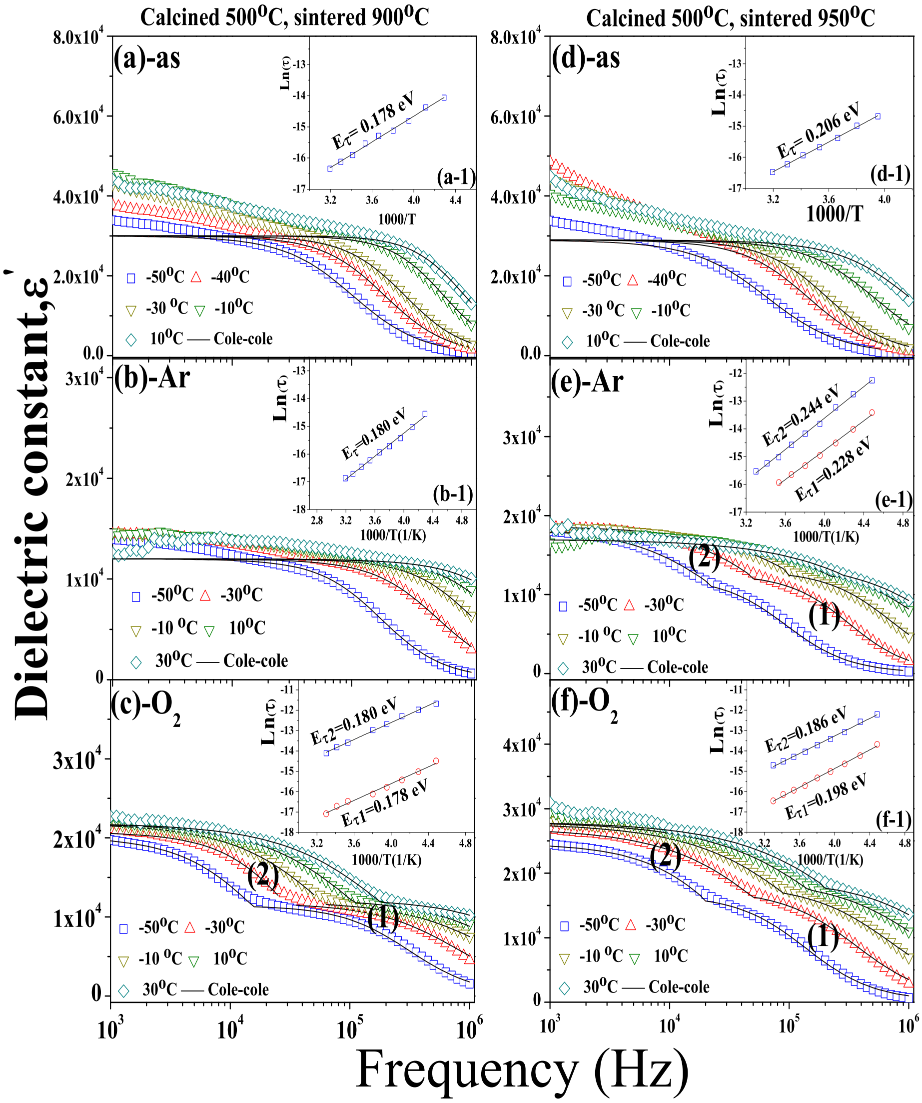

Figure 6.16 The frequency dependence of ε' at various temperatures (the solid lines represent calculated values of Cole-Cole equation) and Arrhenius plots of the dielectric relaxation time (inset (a-1) to (f-1)) for the as-CuO5-DTa (a), Ar-CuO5-DTa (b), O_2-CuO5-DTa (c), as-CuO5-DTb (d), Ar-CuO5-DTb (e) and O_2-CuO5-DTb (f) samples, respectively.

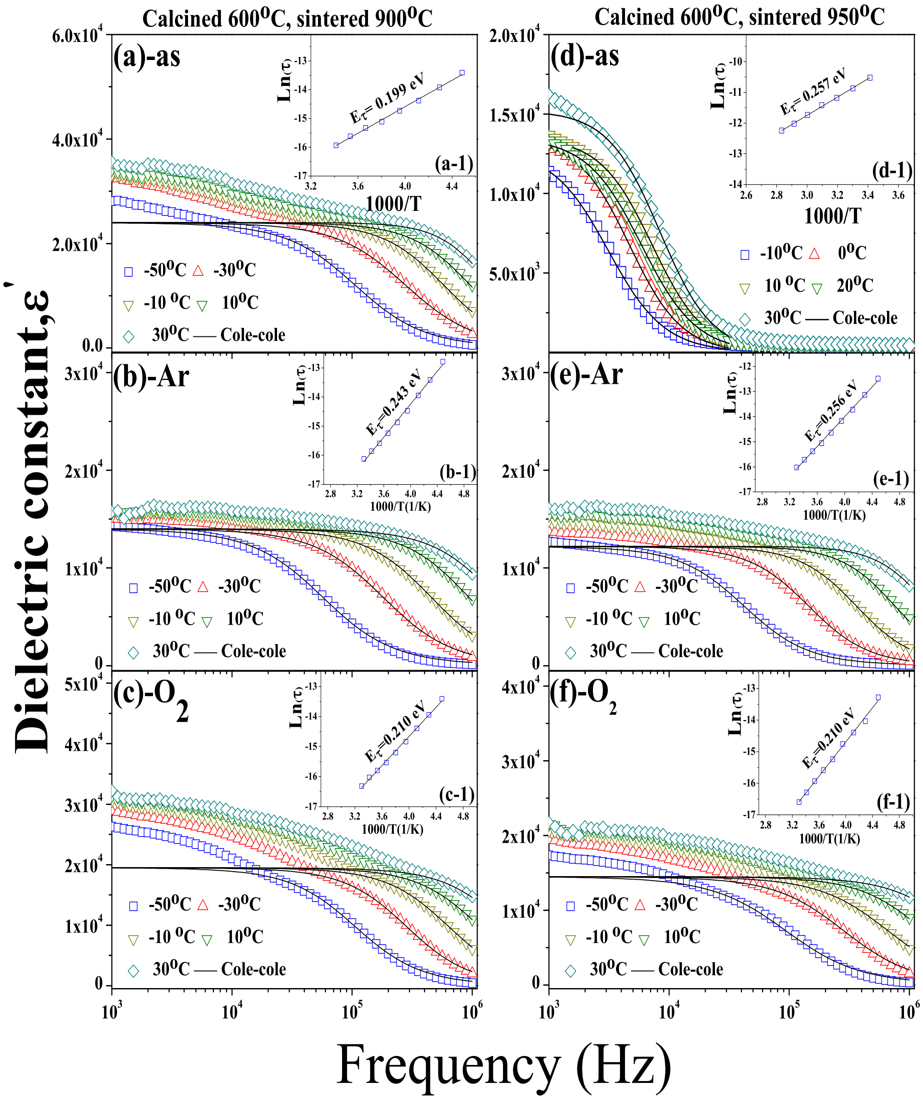

Figure 6.17 The frequency dependence of ε' at various temperatures (the solid lines represent calculated values of Cole-Cole equation) and Arrhenius plots of the dielectric relaxation (inset (a-1) to (f-1)) for the as-CuO6-DTa (a), Ar-CuO6-DTa (b), O$_2$-CuO6-DTa (c), as-CuO6-DTb (d), Ar-CuO6-DTb (e) and O$_2$-CuO6-DTb (f) samples, respectively.

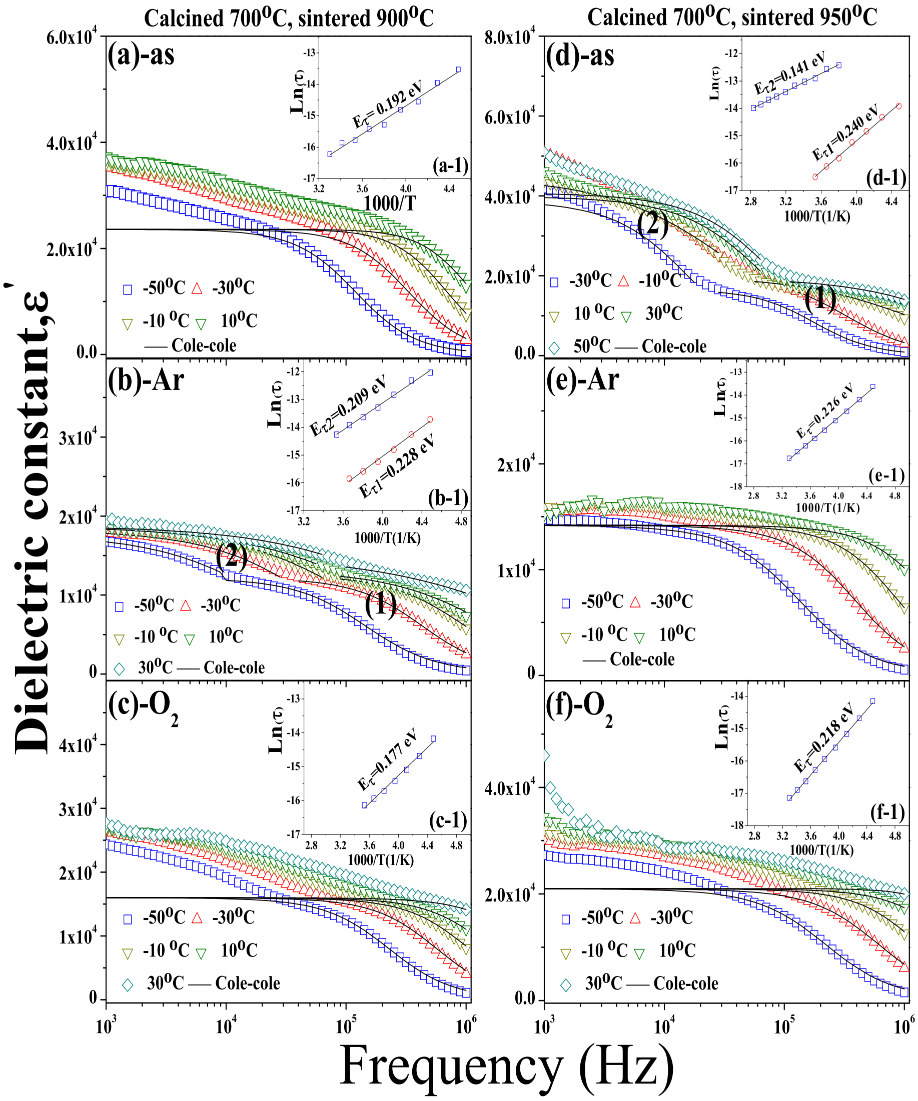

Figure 6.18 The frequency dependence of ε' at various temperatures (the solid lines represent calculated values of Cole-Cole equation) and Arrhenius plots of the dielectric relaxation time (inset (a-1) to (f-1)) for the as-CuO7-DTa (a), Ar-CuO7-DTa (b), O_2-CuO7-DTa (c), as-CuO7-DTb (d), Ar-CuO7-DTb (e) and O_2-CuO7-DTb (f) samples, respectively.

Table 6.3 Relaxation times of the as-, Ar-, O_2-CuO5-DTa and as-, Ar-, O_2-CuO5-DTb samples in the temperature range from -50°C to 30°C.

Temperature	CuO5-DTa				CuO5-DTb				
($°C$)	as-τ	Ar-τ	O_2-$\tau(\mu s)$		as-τ	Ar-$\tau(\mu s)$		O_2-$\tau(ms)$	
	(μs)	(μs)	(1)	(2)	(μs)	(1)	(2)	(1)	(2)
-50	1.56	0.9	8.5	0.51	2.42	4.8	1.5	5	1.15
-40	0.84	0.48	6.3	0.3	1.1	2.9	0.82	3.5	0.66
-30	0.57	0.3	4.6	0.2	0.76	1.8	0.5	2.1	0.44
-20	0.36	0.2	3.1	0.14	0.42	1	0.32	1.5	0.3
-10	0.27	0.15	2.3	0.1	0.31	0.7	0.22	1.1	0.22
0	0.215	0.12	-	-	0.21	0.47	0.16	0.8	0.15
10	0.18	0.09	1.25	0.07	0.155	0.3	0.12	0.62	0.12
20	0.124	0.071	1	0.06	0.12	0.24	0.1	0.5	0.09
30	0.1	0.055	0.74	0.04	0.09	0.18	0.9	0.41	0.07

Table 6.4 Relaxation times of the as-, Ar-, O_2-CuO6-DTa and as-, Ar-, O_2-CuO6-DTb samples in the temperature range from -50°C to 30°C.

Temperature	CuO6-DTa				CuO6-DTb			
($°C$)	as-τ	Ar-τ	O_2-$\tau(\mu s)$		as-τ	Ar-τ	O_2-$\tau(ms)$	
	(μs)	(μs)	(1)	(2)	(μs)	(μs)	(1)	(2)
-50	1.5	2.8	0.15	-	90	3.79	1.7	-
-40	0.9	1.5	0.088	-	-	1.98	0.8	-
-30	0.57	0.88	0.056	-	-	1.1	0.56	-
-20	0.4	0.52	0.036	-	24	0.7	0.39	-
-10	0.27	0.35	0.025	-	51	0.44	0.24	-
0	0.22	0.24	0.018	-	34	0.29	0.17	-
10	0.17	0.17	0.014	-	22	0.21	0.12	-
20	0.12	0.13	0.011	-	27	0.15	0.084	-
30	0.11	0.1	0.008	-	19	0.11	0.062	-

about three order of magnitude higher than those of the Ar-CuO5-DTa samples which have their values lower by about three orders of magnitude than those of the Ar-CuO7-DTa samples. In addition, the O_2-CuO5-DTa and O_2-CuO5-DTb samples show two relaxation times the value of the relaxation time in region (1) is five to six orders of magnitude higher than that in region (2) for both samples. This might be due to the effect of the electrode polarization and the interface

Table 6.5 Relaxation times of the as-, Ar-, O_2-CuO7-DTa and as-, Ar-, O_2-CuO7-DTb samples in the temperature range from -50°C to 30°C.

Temperature	CuO7-DTa					CuO7-DTb				
($^\circ C$)	as-τ	Ar-$\tau(\mu s)$		O_2-$\tau(\mu s)$		as-$\tau(\mu s)$		Ar-τ	O_2-$\tau(ms)$	
	(μs)	(1)	(2)	(1)	(2)	(1)	(2)	(μs)	(1)	(2)
-50	1.33	6	1.1	0.7	-	11	1.2	1.2		
-40	0.87	4.5	0.64	0.42	-	8.5	0.77	0.68		
-30	0.48	2.7	0.37	0.28	-	4.7	0.49	0.41		
-20	0.37	1.7	0.24	0.2	-	-	0.32	0.27		
-10	0.23	1.2	0.17	0.15	-	4	0.15	0.18		
0	0.2	0.9	0.13	0.12	-	3.7	0.12	0.13		
10	0.14	0.64	0.11	0.1	-	2.3	0.09	0.09		
20	0.13	0.4	0.06	0.06	-	2.2	-	0.07		
30	0.09	0.34	-	0.05	-	1.9	-	0.05		

between electrode and the new surface layer. The dielectric relaxation time of these samples can be obtained by Arrhenius law (Eq. (6.2)). By using Eq. (6.2) the fitted curve can be obtained as shown in the insets of Figures 6.16 - 6.18 ((a) -(c)) and ((d) - (f)) for the as-, Ar-, O_2-CuO5-DTa; as-, Ar-, O_2-CuO6-DTa; as-, Ar-, O_2-CuO7-DTa and as-, Ar-, O_2-CuO5-DTb; as-, Ar-, O_2-CuO6-DTb; as-, Ar-, O_2-CuO7-DTb, respectively. The vales of activation energy (E_τ) are obtained to be 0.178; 0.180; 0.180(1), 0.178(2) and 0.206; 0.244(1), 0.228(2); 0.186(1), 0.198(2) eV for the as-, Ar-, O_2-CuO5-DTa (inset (a-1) to (c-1) of Figure 6.16) and as-, Ar-, O_2-CuO5-DTb (insets (d-1) to (f-1) of Figure 6.16), respectively. Whereas, the E_τ values of the as-, Ar-, O_2-CuO6-DTa and as-, Ar-, O_2-CuO6-DTb (insets of Figures 6.17 (a) - (f)) are 0.199; 0.243; 0.210 and 0.257; 0.256; 0.210 eV, respectively. In addition, the values of activation energy of the as-, Ar-, O_2-CuO7-DTa and as-, Ar-, O_2-CuO7-DTb samples (inset of Figures 6.18 (a) - (f)) are 0.192; 0.209(1), 0.228(2); 0.147 and 0.141; 0.240; 0.225; 0.218 eV, respectively.

6.2.2 The impedance analysis

In order to understand the responses of the dielectric dispersion of the samples prepared by the DT method, the complex impedance analysis was performed. By using the complex impedance, Z^*, plots (Figures 6.19 - 6.21 (a) - (f)) most the samples show a large semicircle at low frequencies with a non-zero intercept on the Z' axis at a high frequency (insets of Figures 6.19 - 6.2 (a) - (f)). The data were interpreted using an equivalence circuit of two parallel RC elements connected in series, as reported by Sakar et al., (2008a) and Tongbai et al., (2008a).

As observed in Figures 6.19 (a) and 6.19 (d) when the temperature is increased from -50°C to 0°C, the R_{int} and the R_{ext} of the as-CuO5-DTa (Figure 6.19 (a)) samples are decreased from 490Ω to 37Ω and 5,400Ω to 607Ω respectively. Whereas these values for the as-CuO5-DTb samples (Figure 6.19 (b)) decreased from 660Ω to 39Ω for the R_{int} and 5,530Ω to 83Ω for the R_{ext}, respectively. Figures 6.19 (b) and 6.19 (e) show the impedance plane, Z^*, plots for the Ar-CuO5-DTa and Ar-CuO5-DTb at the temperature between -50°C to 0°C The R_{int} values of both sample decrease from 968Ω to 95Ω and 698Ω to 95Ω, whereas the R_{ext} values of both samples decrease from 14000Ω to 1840Ω and 14000Ω to 1840Ω, respectively, when the temperature is increased from -50°C to 0°C. Figures 6.19 (c) and (f) show the complex, Z^* impedance plane plots of the O_2-CuO5-DTa and O_2-CuO5-DTb, respectively. The R_{int} values of both samples decrease from 386Ω to 251Ω and 550Ω to 80Ω, whereas the R_{ext} values decrease from 20615Ω to 5466Ω and 9901Ω to 1995Ω when the temperature is increased from -50°C to o°C.

Figure 6.20 shows the complex impedance, Z^*, plots of the as-, Ar- and O_2-CuO6-DTa (Figure 6.20 (a) - (c)) and the as-, Ar- and O-CuO6-DTb (Figure 6.20 (d) - (f)), respectively. Most the samples show large semicircle at low frequencies (Figure 6.20 (a) - (f)) with a non-zero intercept on the Z' axis at high frequency (inset of Figure 6.20 (a) - (f)). When the temperature is increased from -50°C to 0°C, the values of R_{int} and R_{ext} are decreased from 1030Ω to 120Ω and 3660Ω to 1090Ω respectively for the as-CuO6-DTa (Figure 6.20 (a)). The values of R_{int} and R_{ext} of the Ar-CuO6-DTa (Figures 6.20 (b)) are decreased from 1760Ω to 160Ω and 20100Ω to 2160Ω, respectively. Whereas, those of the Ar-CuO6-DTb (Figure 6.20 (e)) are decreased from 2700Ω to 230Ω and 23200Ω to 2510Ω respectively. In addition, the impedance, Z^*, plots of the O_2-CuO6-DTa and O_2-CuO6-DTb are shown in Figures 6.20 (c) and 6.20 (f). When the temperature is increased from -50°C to 0°C, the values of R_{int} and R_{ext} of both samples decrease from 744Ω to 37Ω and 10740Ω to 1788Ω and from 174Ω to 42Ω and 2566Ω to 674Ω, respectively.

Figure 6.21 (a) - (c) shows the complex, Z^*, plots of the as-, Ar- and O_2-CuO7-DTa and as-, Ar- and for those of the O_2-CuO7-DTb are shown in Figures 6.21 (d) - (f). Most samples show large semicircle at low frequencies with a non-zero intercept on the Z' axis at high frequency (inset). When the temperature is increased from -50°C to 0°C the values of R_{int} and R_{ext} are decreased from 630Ω to 100Ω and 9940Ω to 2370Ω for the as-CuO7-DTa (Figure 6.21 (a)), while the R_{int} and R_{ext} of the as-CuO7-DTb sample are decreased from 650Ω to 100Ω and 8800Ω to 2070Ω for (Figure 6.21 (d)). Figures 6.21 (b) and (e) show the decreased of the R_{int} and R_{ext} values from 800Ω to 100Ω and 26500Ω to 3350Ω for the Ar-CuO7-DTa (Figure 6.21 (b)), whereas, those of the Ar-CuO7-DTb samples decreased from 800Ω to 90Ω and 10060Ω to 1470Ω with increasing the temperature from -50°C to 0°C. In addition, the impedance, Z^*, plots of the O_2-CuO7-DTa and O_2-CuO7-DTb are shown in Figures 6.21 (c) and (f). When the temperature is increased from -50°C to 0°C, the R_{int} and R_{ext} values of the O_2-CuO7-DTa decrease from 524Ω to 183Ω and 20682Ω to 6422Ω whereas those of the O_2-CuO7-DTb decrease from 307Ω to 48Ω and 3618Ω to 693Ω, respectively. As observed in

Figures 6.19 - 6.21 (a) - (f), the complex, Z^*, impedance plane plots of the as-, Ar- and O_2-samples with different calcined temperature and sintered at 900°C and 950°C are similar to those observed for the as-, Ar-, O_2-samples prepared by using the commercial CuO powder as shown in section 6.1.2.

Table 6.6 The dielectric constant, dielectric loss tangent activation energy, resistance and capacitance of internal and external part of the as-, Ar-, O_2-samples calcined at 500 - 700°C and the sintered at 900°C (subscript a) and at 950°C (subscript b) prepared by the DT method.

Samples	Dielectric (ε')	tanδ	Resistance (Ω)		Capacitance (nF)	Activation Energy (eV)	
			R_{ext}	R_{int}	$C_{\text{ext}}(1)(2)$	$E_{\tau 1}$	$E_{\tau 2}$
as-CuO5-DTa	47,400	46.5	807	97	7.58	0.178	-
Ar-CuO5-DTa	19,000	200	680	53	2.14	0.18	-
O_2-CuO5-DTa	22,700	54.4	1,000	42	3.47(2.22)	0.18	0.178
as-CuO5-DTb	46,600	45.9	835	39	5.7	0.206	-
Ar-CuO5-DTb	18,900	185	470	63	2.49	0.244	0.228
O_2-CuO5-DTb	30,900	58.8	922	45	4.32(3.36)	0.186	0.198
as-CuO6-DTa	68,900	30.4	796	50	4.9	0.199	-
Ar-CuO6-DTa	15,700	139	780	70	2.54	0.243	-
O_2-CuO6-DTa	32,200	72.3	714	46	4.43	0.21	-
as-CuO6-DTb	16,100	4.79	-	-	3.76	0.257	-
Ar-CuO6-DTb	16,100	107	980	90	2.41	0.256	-
O_2-CuO6-DTb	21,700	96.5	791	53	2.95	0.234	-
as-CuO7-DTa	38,900	41	1,139	46	5.37	0.192	-
Ar-CuO7-DTa	19,400	83	1,150	30	2.6	0.209	0.228
O_2-CuO7-DTa	27,700	75	809	41	3.62	0.177	-
as-CuO7-DTb	50,800	13	1,060	46	7.76	0.24	0.141
Ar-CuO7-DTb	17,800	287	860	57	2.66	0.226	-
O_2-CuO7-DTb	46,000	210	165	21	4.23	0.218	-

Figure 6.22 shows the dielectric constant, ε' at room temperature at the frequency of 1 kHz of the samples prepared from the DT powders. Figures 6.22 (a) and 6.22 (d) show the dielectric constant, ε' of the as-, Ar-, O_2-CuO5-DTa and as-, Ar-, O_2-CuO5-DTb, respectively. The as-samples have giant dielectric constant values 4.74×10^4 and 4.66×10^4 and lower values of 1.90×10^4 and 1.89×10^4 for the Ar-samples, then it increase to 2.27×10^4 and 3.09×10^4 for

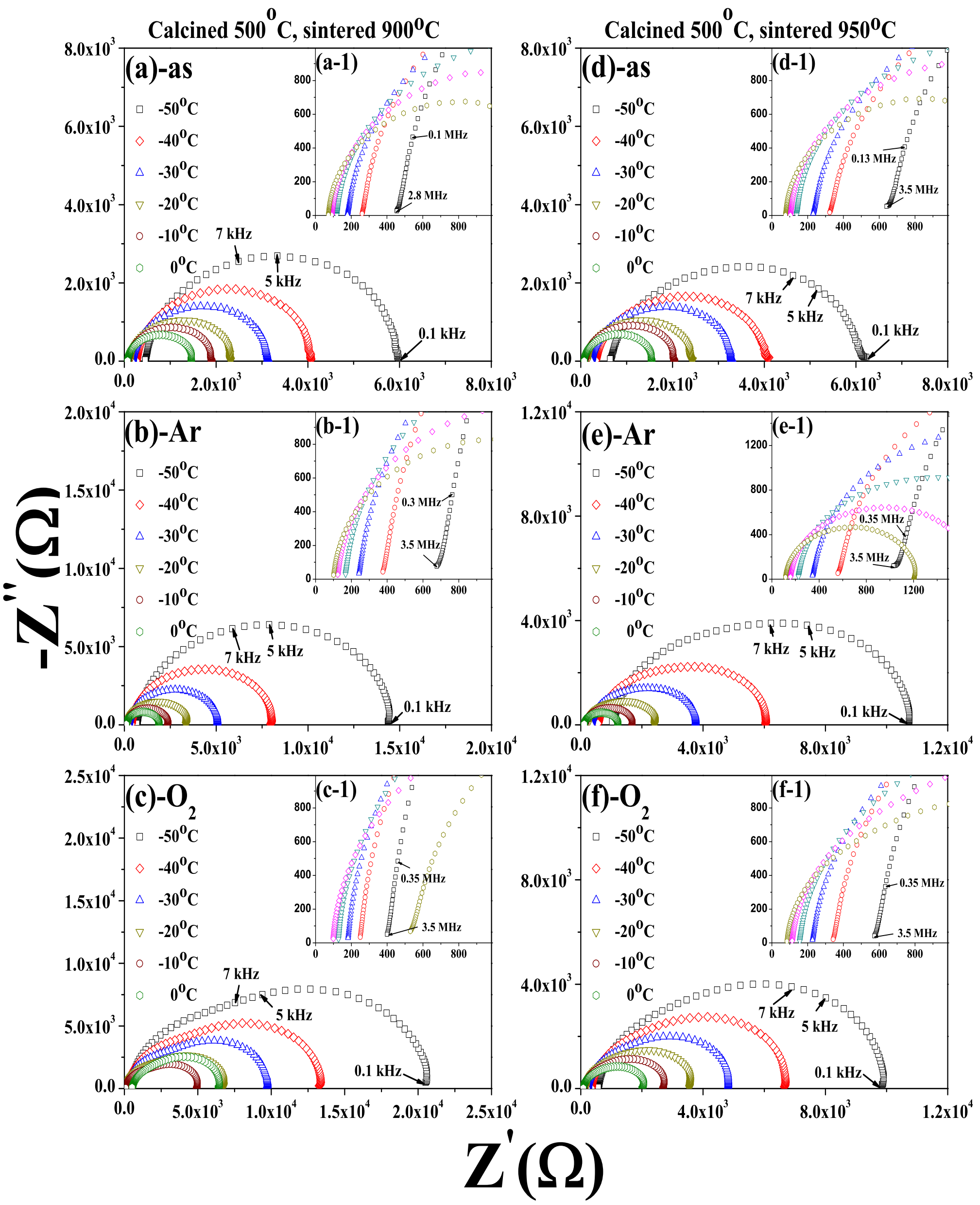

Figure 6.19 Complex impedance, Z^*, plots and the expanding scale (inset) for the as-CuO5-DTa (a), Ar-CuO5-DTa (b), O_2-CuO5-DTa (c), as-CuO5-DTb (d), Ar-CuO5-DTb (e) and O_2-CuO5-DTb (f) samples, respectively.

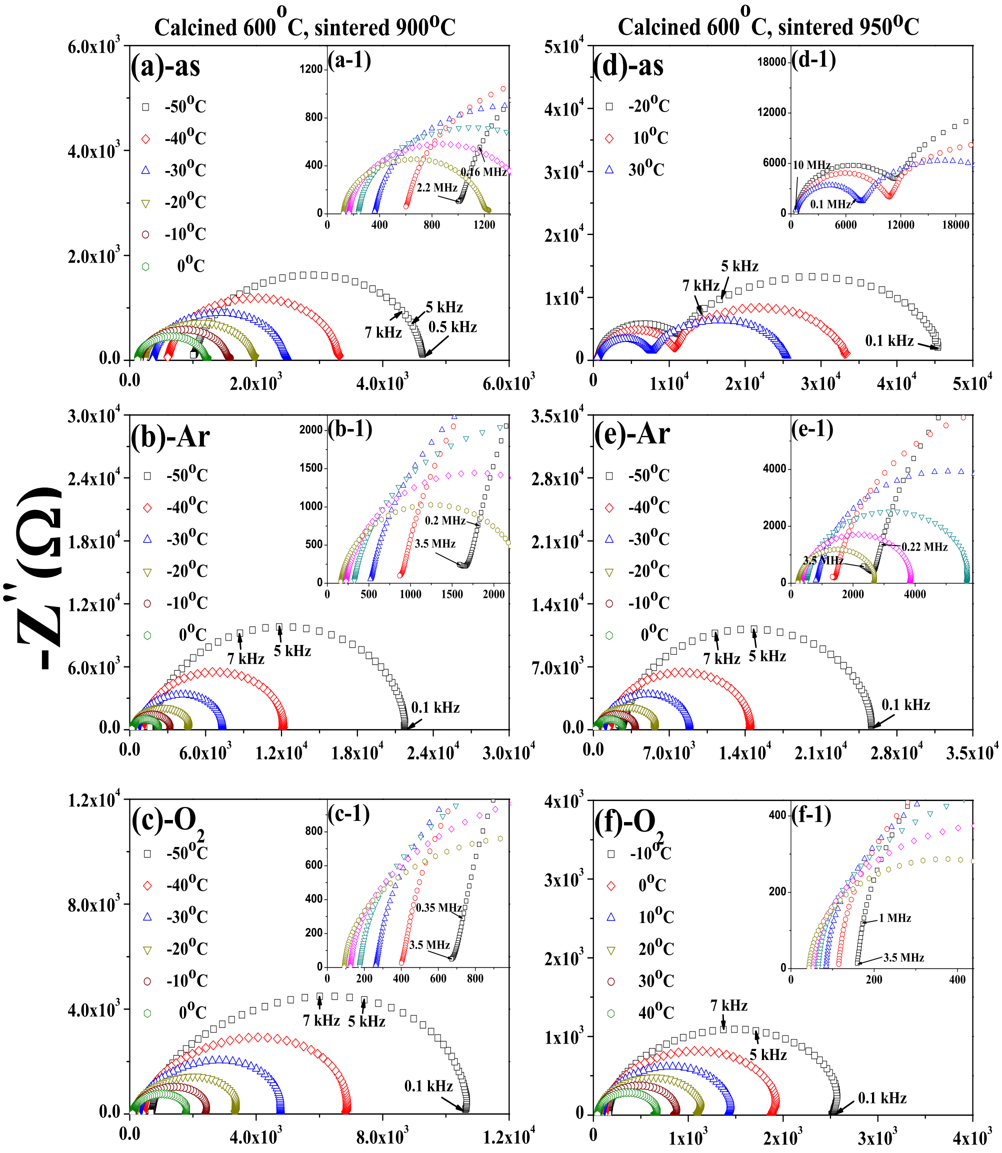

Figure 6.20 Complex impedance, Z^*, plots and the expanding scale (inset) for the as-CuO6-DTa (a), Ar-CuO6-DTa (b), O_2-CuO6-DTa (c), as-CuO6-DTb (d), Ar-CuO6-DTb (e) and O_2-CuO6-DTb (f) samples, respectively.

the O_2-samples. Figures 6.22 (b) and 6.22 (e) show the dielectric constant of the as-, Ar-, O_2-CuO6-DTa and as-, Ar-, O_2-CuO6-DTb, respectively. The as-samples show giant dielectric constant values 6.89×10^4 and 1.61×10^4 and lower to 1.57×10^4 and 1.61×10^4 for the Ar-samples, after that it increase to 3.22×10^4

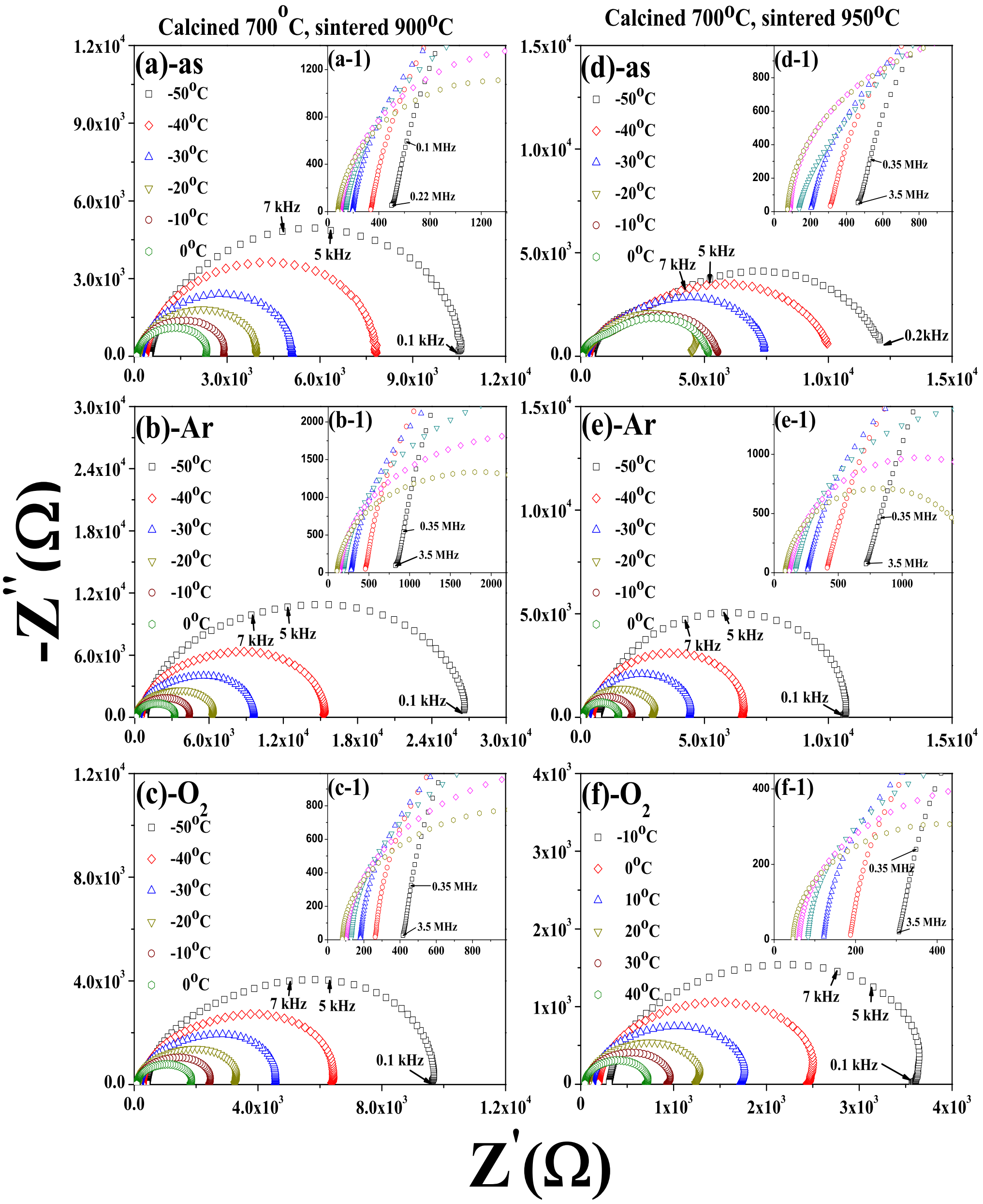

Figure 6.21 Complex impedance, Z^*, plots and the expanding scale (inset) for the as-CuO7-DTa (a), Ar-CuO7-DTa (b), O_2-CuO7-DTa (c), as-CuO7-DTb (d), Ar-CuO7-DTb (e) and O_2-CuO7-DTb (f) samples, respectively.

and 2.17×10^4 for the O-samples. The as-samples (Figures 6.22 (c) and 6.22 (f)) show giant dielectric constant values 3.89×10^4 and 5.08×10^4. These values are reduced to 1.94×10^4 and 1.78×10^4 for the Ar-samples, then increased again to 2.77×10^4 and 4.60×10^4 for the O_2-samples. This enhancement of the ε' in these samples is due to the oxygen vacancy presented in the samples as explained in section 6.1. However, the ε' cannot be recovered to the original values of the as-samples (Figures 6.22 (a) - (f), mark $\triangledown$), and it was found that the relaxation peak of both samples after annealing in oxygen shifts to higher frequencies when comparing with as- and Ar-samples at the same temperature. This effect might be result from the depletion resistance of the surface layer in the sample for O_2-samples.

Figures 6.23 (a) - (c) compare the dielectric constant of the as-, Ar- and O_2-samples prepared from the powders calcined at 500, 600 and 700°C as a function of sintering temperature. The dielectric constant of the as- samples sintered at 900°C is a little higher than that of the sintered at 950°C for the as-CuO7-DT samples (Figure 6.23 (c)), but smaller than those of the as-CuO5-DT samples. It can be seen that, the ε' of all the samples sintered at 900°C and 950°C are decreased after annealing in argon (Ar-samples), corresponding to the increasing of the tanδ (Figures 6.23 (d) - (f)). However, the ε' of the samples can be increased when re-annealed in oxygen (O_2-samples), corresponding to the decrease in the tanδ (Figures 6.23 (d) - (f)).

Figures 6.24 (a) - (c) compare the external resistance (R_{ext}) of the as-, Ar- and O_2-samples prepared from the powders calcined at 500, 600 and 700°C as a function of sintered. The R_{int} values of the as-CuO5-DTa and as-CuO5-DTb are decreased after annealing in argon (Ar-samples) and increased after re-annealing in oxygen (O_2-samples), whereas the R_{int} values are increased after annealing in argon and decreased after re-annealing in oxygen for the as-CuO5-DTb, but these do not occur for the as-CuO5-DTa (Figures 6.24 (a) and (d)). The R_{ext} values of the as-samples prepared from the powder calcined at 600°C and then sintered at 900°C and 950°C (Figure 6.24 (b)) are slightly increased for the Ar-

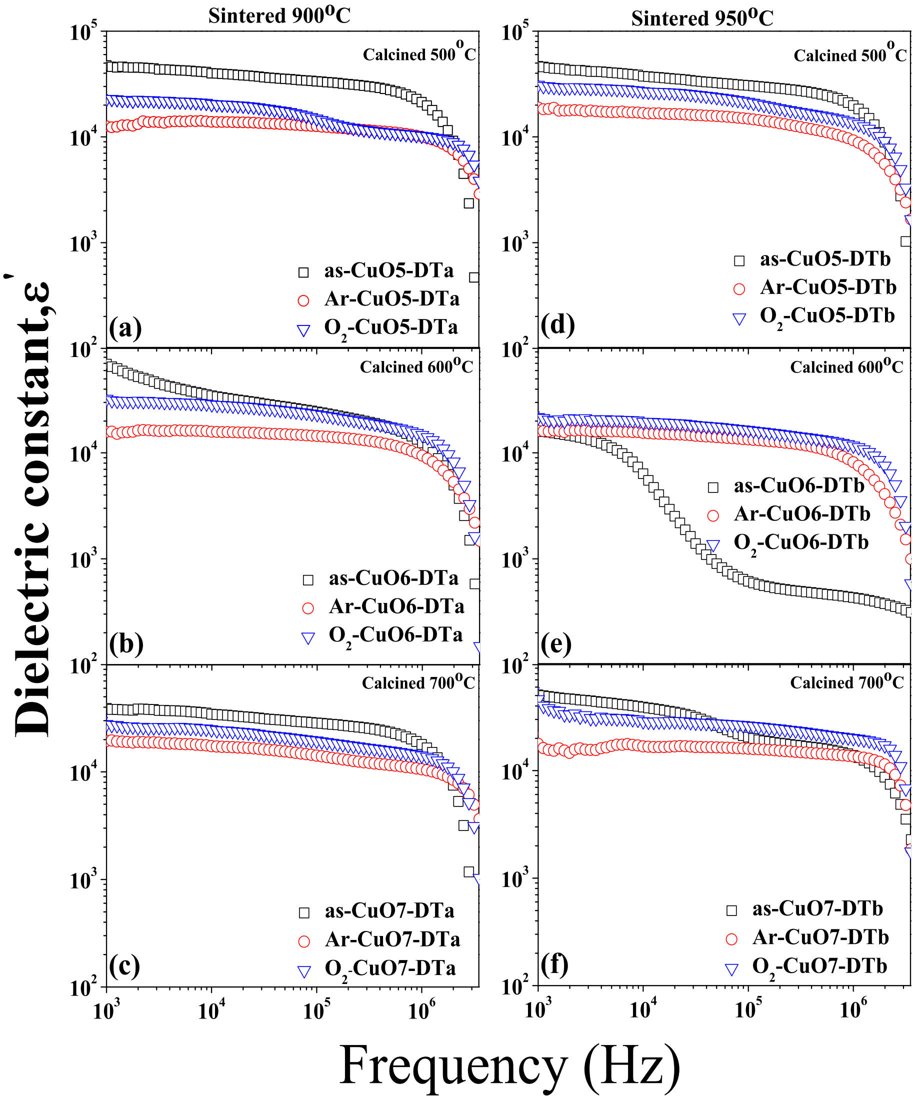

Figure 6.22 Frequency dependence of the dielectric constant at room temperature of the as-, Ar- and O_2-CuO5-DTa (a), as-, Ar- and O_2-CuO6-DTa (b), as-, Ar- and O_2-CuO7-DTa (c), as-, Ar- and O_2-CuO5-DTb (d), as-, Ar- and O_2-CuO6-DTb (e) and as-, Ar- and O_2-CuO7-DTb (f), respectively.

and O_2-samples, while the R_{int} values of the Ar- and O_2-samples are increased and decreased, respectively. The R_{ext} values of the as-samples prepared from the powder calcined at 700°C and then sintered at 900°C and 950°C (Figure 6.24 (c)) are decreased for the Ar-samples and decreased for the O_2-samples, while the R_{int} values (Figure 6.24 (f)) are decreased for the Ar-samples and increasing for the

O_2-samples sintered at 900°C, and similar results are observed in the Ar- and O_2-samples sintered at 950°C.

6.2.3 Effect of dc-bias voltage

Figures 6.25 (a) - (c) show the effect of the dc-bias voltage on the dielectric constants as a function of frequency (10 - 100 kHz) for those samples prepared from the powders calcined at 500, 600 and 700°C and then sintered at 900°C, respectively. The dielectric constants decrease with increasing the dc-bias voltage and then show step decrease with increasing frequencies (inset). Similarly, the dielectric constants decrease with increasing the dc-bias voltage for the as-samples sintered at 950°C (Figure 6.25 (d) - (f)). Again the dielectric constants decrease with increasing frequencies (inset). The decrease of the dielectric constant with the dc-bias voltage for the CuO-samples prepared by the DT method is similar to those observed in the CuO-samples prepared from the commercial CuO powder discussed in section 6.1.3.

Figures 6.26 (a) - (f) show the complex impedance (at room temperature) containing a large semicircle at low frequencies with non zero intercept at high frequency (inset) on the Z' axis. The R_{ext} and the dielectric constant decrease with increasing dc-bias voltage (0 - 3 V). The R_{ext} values for the samples prepared from the powders calcined at 500, 600 and 700°C and then sintered at 900°C (Figures 6.26 (a) - (c)) decrease from 1,443Ω to 81Ω; 458Ω to 114Ω; 830Ω to 87Ω, whereas the R_{int} values remain constant at 42Ω, 67Ω and 41Ω, respectively. Figure 6.26 (d) - (f) show the decreasing of the R_{ext} values of the samples prepared from the powders calcined at 500, 600 and 700°C and then sintered at 950°C from 784Ω to 82Ω; 2,000Ω to 120Ω; 1,645Ω to 107Ω, whereas the R_{int} remains constant at 47Ω, 110Ω and 41Ω, respectively. In this study, the capacitance bridge is not

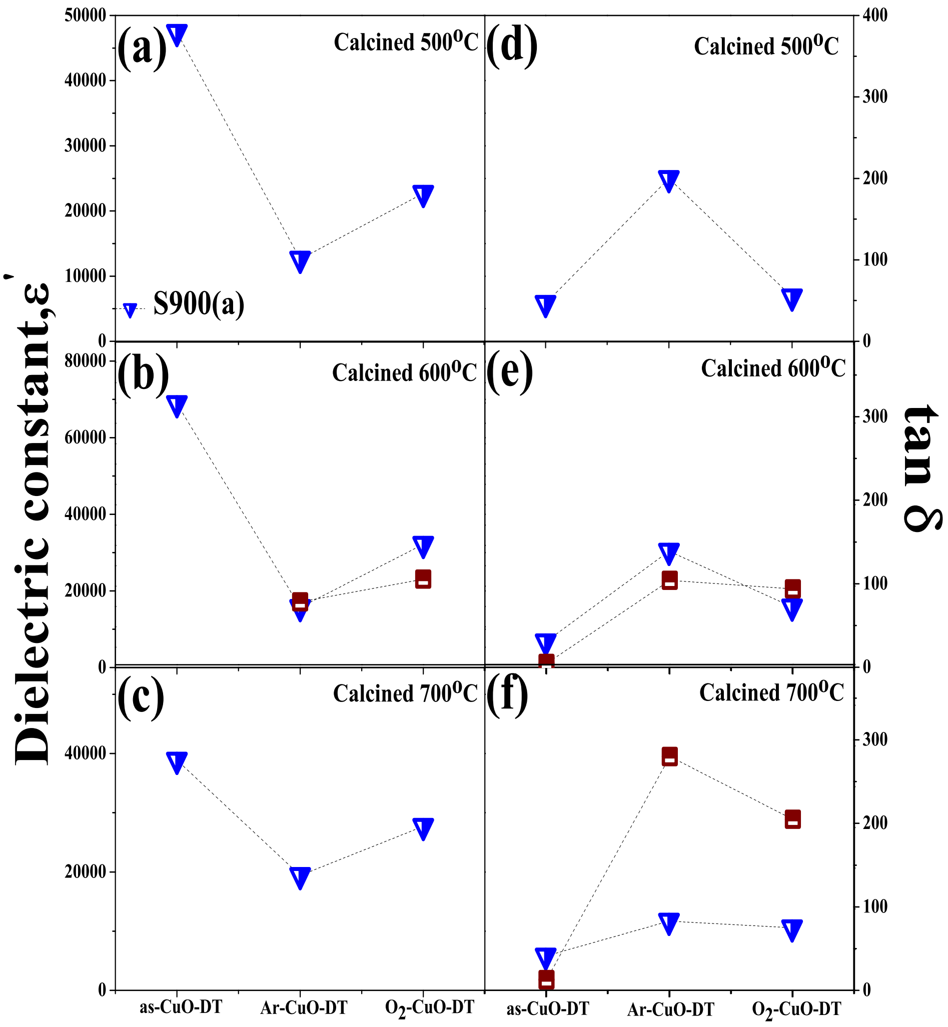

Figure 6.23 Dielectric constant (a) - (c) and dielectric loss tangent (d) - (f) of the as-, Ar- and O_2-samples prepared from the powders calcined at 500°C (a), 600°C (b) and 700°C (c) with the different sintering temperatures of 900°C (▽) and 950°C (□).

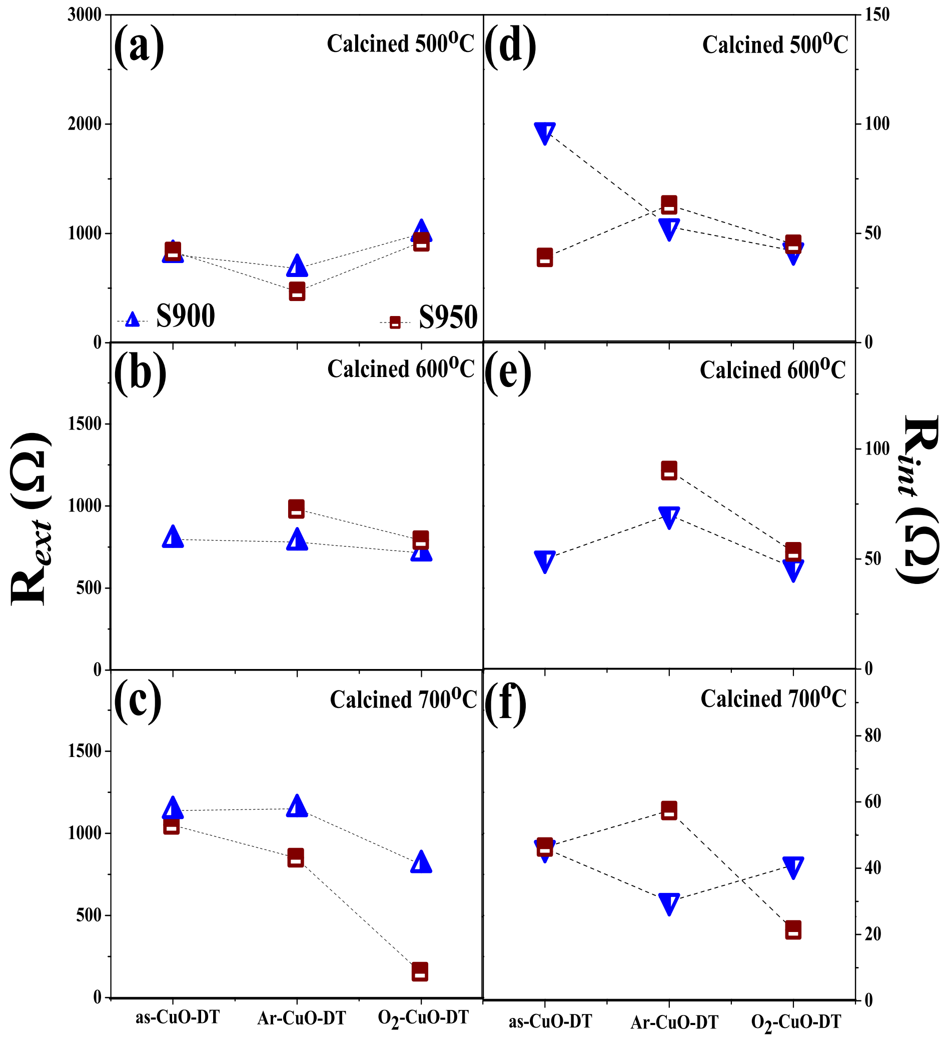

Figure 6.24 The external resistance (R_{ext}) (a) - (c) and the internal resistance (R_{int}) (d) - (f) of the as-, Ar- and O$_2$-samples prepared from the powders calcined at 500°C (a), 600°C (b) and 700°C (c) with different sintering temperatures of 900°C (▽) and 950°C (□).

balanced at the voltages over 3.6 V due to the large leakage current. When the dc-bias is over the limited balance, the charge carrier can cross over the potential well of the external part (electrode and surface layer), thus they are disappeared at the interfacial polarization and then the total polarization is only contributed by the internal part (grains and GBs). The decrement of the ε' due to the influence

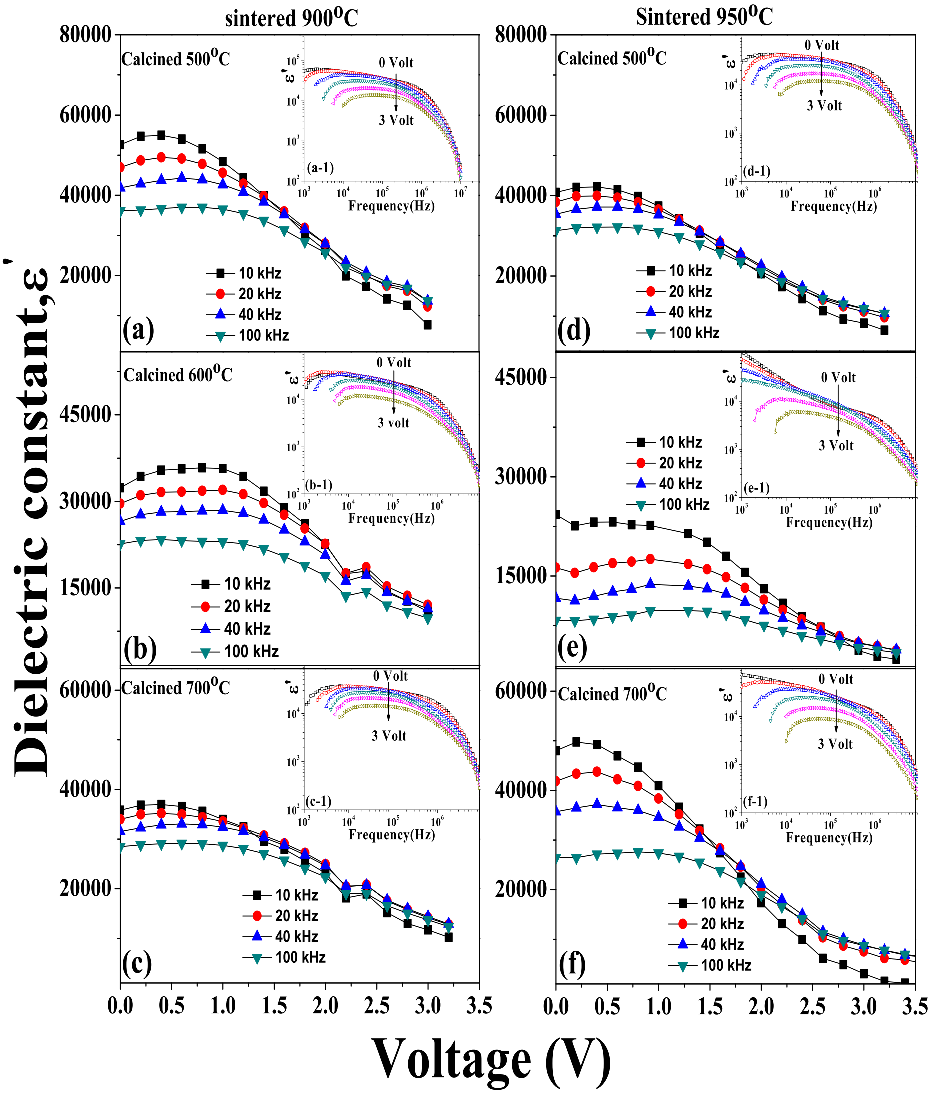

Figure 6.25 The effect of dc-bias voltage (0 - 3.5 V) on the dielectric constant as functions of frequency (10-100 kHz) and voltage (inset) for the as-CuO5-DTa (a), as-CuO6-DTa (b) and as-CuO7-DTa (c), as-CuO5-DTb (d), as-CuO6-DTb (e) and as-CuO7-DTb (f) , respectively.

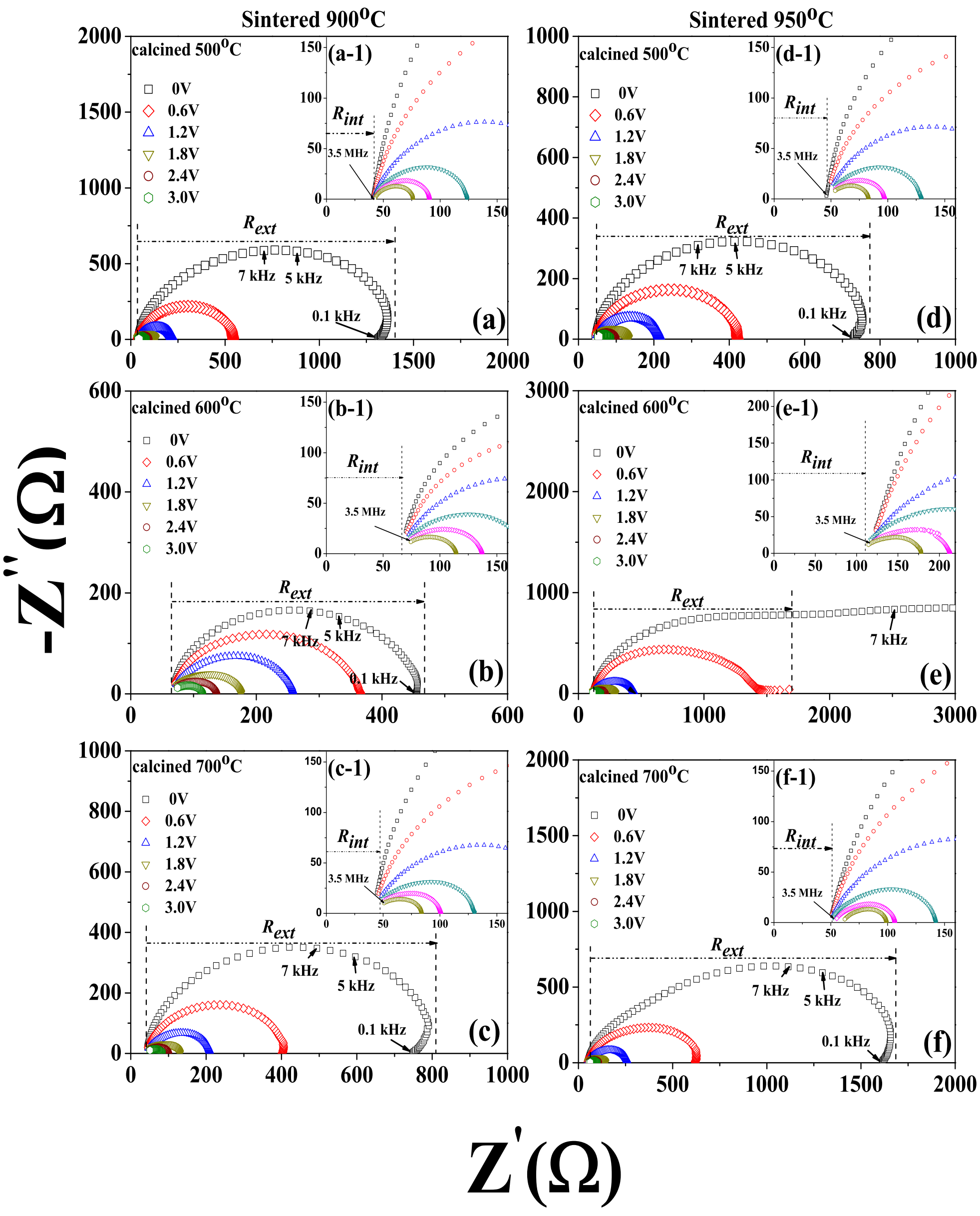

Figure 6.26 Complex impedance, Z^*, plot and the expanding scale (inset) at room temperature as a function of dc-bias voltage (0 - 3 V) of the as-CuO5-DTa (a), as-CuO6-DTa (b) and as-CuO7-DTa (c), as-CuO5-DTb (d), as-CuO6-DTb (e) and as-CuO7-DTb (f), respectively.

of dc-bias is partly contributed by the external free charge and the remaining contributive beyond the limiting balance of the dc-bias voltage causing from the internal free charge. Therefore, the dc-bias voltage should have effect on the electrical properties of the external free charge, whereas it has no effect on internal free charge.

6.2.4 Effect of uniaxial compressive stress

The effect of uniaxial compressive stress on the dielectric constant (ε') and dielectric loss tangent (tanδ) of the DT-prepared CuO samples were studied . Figures 6.27 (a) - (c) and Figures 6.27 (d) - (f) show the stress dependence of the dielectric constant (ε') at the frequencies of 2, 5, 10, 20 and 100 kHz for the as-samples prepared from the powders calcined at 500, 600 and 700°C and then sintered at 900°C (as-CuO5-DTa, as-CuO6-DTa, as-CuO7-DTa) and 950°C (as-CuO5-DTb, as-CuO6-DTb, as-CuO7-DTb), respectively. There is a significant change in the dielectric constant of the samples when the applied stress is increased from 0 to 100 MPa. The changes of the dielectric constant with the applied stress can be divided into two regions. Region 1 might be the effect of uniaxial compressive stress on the external part (electrode and surface layer), and region 2 might be the internal part (grains and GBs). For the as-CuO5-DTa, as-CuO6-DTa, as-CuO7-DTa samples (Figures 6.27 (a) - (c)), the dielectric constant is increased with increasing the applied stress to the maximum values of 4.1×10^7 at 37 MPa, 1.0×10^8 at 37 MPa, and 4.5×10^7 at 55 MPa, respectively. After that it decrease to 7.2×10^6 at 56 MPa for the as-CuO5-DTa, 12×10^6 at 62 MPa for the as-CuO6-DTa and 3.2×10^6 at 100 MPa for the as-CuO7-DTa. The results are similar to those observed for the as-CuO5-DTb, as-CuO6-DTb and as-CuO7-DTb samples (Figures 6.27 (d) - (f)).

Figures 6.28 (a) - (f) show the independent of the dielectric loss tangent (tanδ as a function of uniaxial compressive stress (0 - 100 MPa) at the frequencies of 2, 5, 10, 20 and 100 kHz for the as-samples prepared from the powders calcined

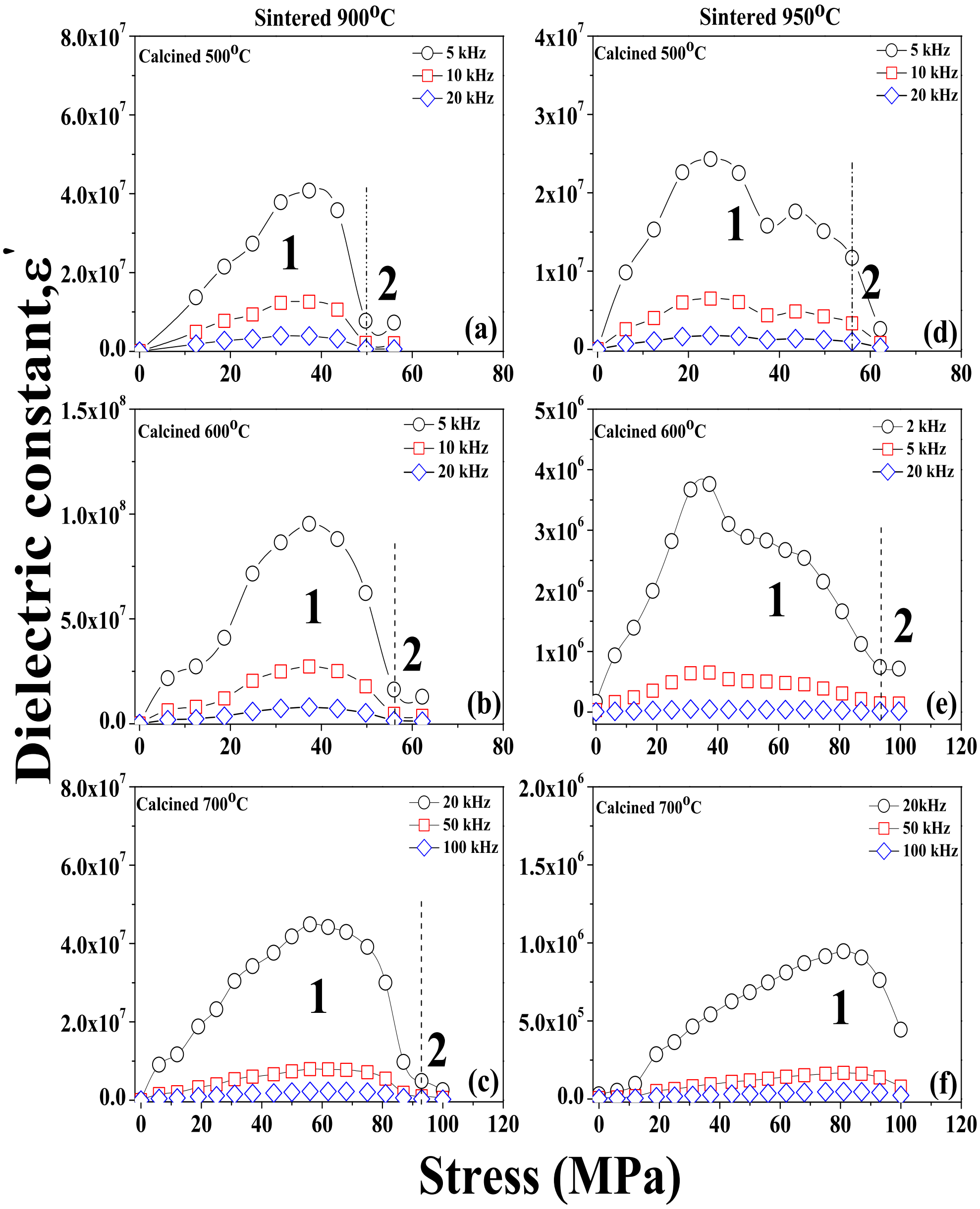

Figure 6.27 Effect of the uniaxial compressive stress (0 - 100 MPa) on the dielectric constant measured at different frequencies of the as-CuO5-DTa (a), as-CuO6-DTa (b) and as-CuO7-DTa (c), as-CuO5-DTb (d), as-CuO6-DTb (e) and as-CuO7-DTb (f), respectively.

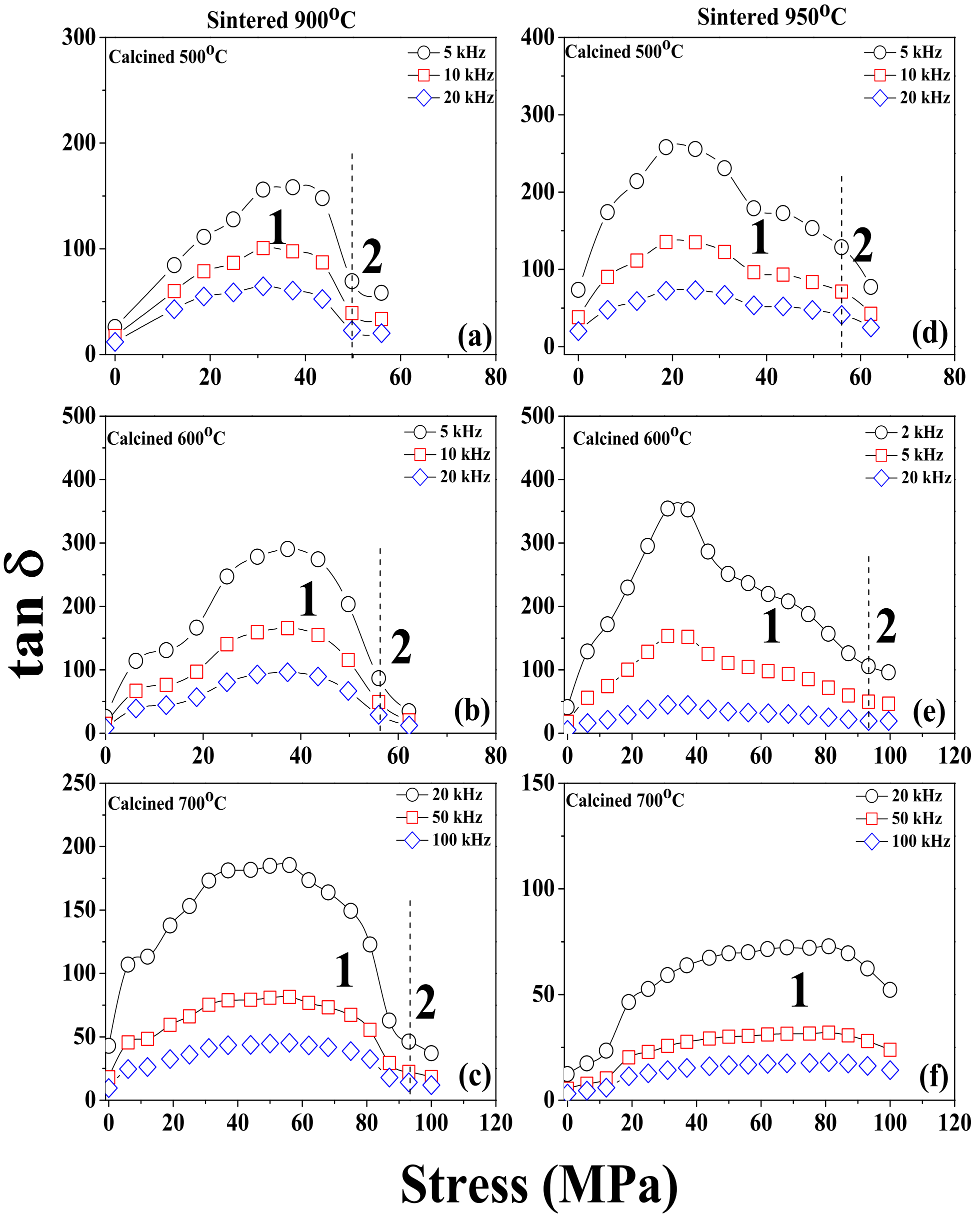

Figure 6.28 Effect of uniaxial compressive stress (0 - 100 MPa) on the dielectric loss tangent of the as-CuO5-DTa (a), as-CuO6-DTa (b) and as-CuO7-DTa (c), as-CuO5-DTb (d), as-CuO6-DTb (e) and as-CuO7-DTb (f), respectively.

at 500, 600 and 700°C and then sintered at 900°C (as-CuO5-DTa, as-CuO6-DTa, as-CuO7-DTa) and 950°C (as-CuO5-DTb, as-CuO6-DTb, as-CuO7-DTb), respectively. The tanδ value as a function of compressive stress (0-100MPa) is increased and decreased to the maximum and minimum values at the same compressive stress of the dielectric constant discussed in the Figures 6.27 (a) - (f). The tanδ of the as-CuO5-DTa, as-CuO6-DTa, as-CuO7-DTa samples (Figures 6.28 (a) - (c)), is increased with increasing the applied stress to the maximum values of 155 at 37 MPa; 300 at 37 MPa; and 175 at 55 MPa, respectively. After that it decreases to 58 at 56 MPa for the as-CuO5-DTa; at 62 MPa for the as-CuO6-DTa and at 100 MPa for the as-CuO7-DTa. Again these results are similarly to those observed in the as-CuO5-DTb, as-CuO6-DTb and as-CuO7-DTb samples (Figures 6.27 (d) - (f)).

The sudden change in the external capacitance (electrode and surface layer) gives rise to the change ε' and tanδ values of these samples which is due to the uniaxial compressive stress as discussed in section 6.1.4.

6.3 Electrical properties of the CuO ceramics prepared by the PR method

In this section, the dielectric behavior as a function of frequency, temperature together with the relaxation behaviors of the as-, Ar- and O_2-sample prepared from the powders calcined at 500, 600 and 700°C and sintered at 900°C and 950°C will be presented. The impedance spectroscopy model (IS model) used to study the electrical properties of these samples and the effect of the dc-bias voltage and uniaxial compressive stress on the dielectric constant and dielectric loss tangent is discussed also.

6.3.1 Dielectric properties

Figure 6.29 shows the frequency dependence of the dielectric constant, ε' (left axis) and the dielectric loss tangent, tanδ (right axis) for the sample prepared from the powders calcined at 500°C and then sintered at 900°C and 950°C of the as-samples ((a) and (d)), Ar-samples ((b) and (e)) and O_2-samples ((c) and (f)). Figures 6.29 (a) and 6.29 (d) show the ε' values at the temperature range from -50°C to 0°C of $(1.38 - 1.4) \times 10^4$ and $(1.20 - 1.4) \times 10^4$ and the tanδ values of $(1.29 - 15.7)$ and $(1.35 - 14.1)$ for the as-CuO5-PRa and as-CuO5-PRb at 1 kHz, respectively. After annealing in Ar, the ε' values decrease to $(0.52 - 0.79) \times 10^4$ and $(0.44 - 0.75) \times 10^4$, whereas the tan$\delta$ values are $(0.79 - 12.4)$ and $(0.67 - 5.21)$ for the Ar-CuO5-PRa and Ar-CuO5-PRb (Figures 6.29 (b) and 6.29 (e)). The ε' increases again to the values of $(1.13 - 1.34) \times 10^4$ and $(1.01 - 1.11) \times 10^4$, while the tan$\delta$ values are $(4.46 - 91.6)$ and $(4.10 - 43.2)$ for the O-CuO5-PRa and O_2-CuO5-PRb, respectively.

Figure 6.30 ((a) - (f)) shows the frequency dependence of the ε' (left axis) and tanδ (right axis) for the samples prepared from the powders calcined at 600°C following by sintering at 900°C and 950°C. The ε' and tanδ values of the as-CuO6-PRa and as-CuO6-PRb shown in Figure 6.30 ((a) and (d)) are $(1.09 - 2.30) \times 10^4$ and $(0.9 - 1.37) \times 10^4$ and $(0.97 - 5.57)$ and $(0.98 - 8.9)$, respectively. After that, the values of dielectric constant decrease to $(0.46 - 0.80) \times 10^4$ and $(0.92 - 6.17) \times 10^3$, while the values of dielectric loss tangent increase to $(1.30 - 12.3)$ and $(2.7 - 5.28)$ for the Ar-CuO6-PRa and Ar-CuO6-PRb (Figures 6.30 (b) and 6.30 (e)). Again, the ε' and tanδ values can be increased to the values of $(1.48 - 1.88) \times 10^4$, $(0.96 - 1.02) \times 10^4$ and $(1.30 - 80.2)$, $(3.44 - 42.2)$ for the O_2-CuO6-PRa and O_2-CuO6-PRb (Figures 6.10 (c) and (f)), respectively.

Figure 6.31 shows the frequency dependence of the dielectric constant, ε' (left axis) and dielectric loss tangent, tanδ (right axis) for the samples prepared from the powders calcined at 700°C and sintered at 900°C and 950°C, respectively. Figures 6.31 (a) and 6.31 (d) show $(0.75 - 1.38) \times 10^4$ and $(39.4 - 45.7)$ for the dielectric constant, ε', with the tanδ values of $(0.82-2.70)$ and $(0.03-0.13)$ at the temperature range from -50°C to 0°C for the as-CuO7-PRa and as-CuO7-PRb at 1 kHz, respectively. The values of dielectric constant decrease to $(0.36-2.41)\times10^3$ and $(4.10 - 15.16)$, whereas the values of dielectric loss tangent increase to $(50 - 73.8)$ and $(0.04 - 0.28)$ for the Ar-CuO7-PRa and Ar-CuO7-PRb (Figures 6.31 b and 6.31 e), respectively. Then, the dielectric constant, ε' and tanδ show the values of $(0.49 - 0.56) \times 10^4$, $(0.96 - 1.15) \times 10^2$ and $(6.11 - 126)$, $(1.49 - 16.1)$ for the O_2-CuO7-PRa and O_2-CuO7-PRb (Figures 6.31 (c) and 6.31 (f)), respectively. The dielectric constant and tanδ values of the Ar- and O_2-samples are similar to those observed for the samples prepared by the DT method and commercial CuO powder, shown in section 6.2.1. The dielectric constant of the CuO7-PRb (Figures 6.31 ((d) - (f))) is very small comparing with those of the CuO5-PRb and CuO6-PRb since there is less oxygen vacancy in the CuO7-PRb sample due to the high calcined temperature (700°C). This effect is attributed to the high resistance values which are more than 1MΩ.cm compared to those of the resistances of the samples prepared from the powders calcined at 500°C and 600°C (Table 6.10). The average grain size of the CuO7-PRb sample is higher by about two to three orders of magnitude than the other two samples (Figure 5.13 (f)).

The temperature dependence of the dielectric constant (left axis) and the dielectric loss tangent (right axis) over the temperature range from -50 to 100°C and the frequency range from 1 kHz to 1 MHz for the as-samples prepared from the powders calcined at and then sintered at 900°C and 950°C are shown in Figures 6.32 - 6.34 ((a) - (f)), respectively. At 1 kHz, the dielectric constant of most samples are independent of the temperature at above -50°C. This is corresponded to the dielectric loss tangent, tanδ, which shows on the right axis. The ε' starts to decrease at a higher frequency for the higher tested measuring temperatures. This indicates that thermally activated relaxation also occurs in the samples prepared by the PR method similar to those observed for the DT method, commercial CuO powder and to those reported by Sakar and Thongbai (Sarkar et al., 2008a; Thongbai et al., 2008b).

For further understanding on the physical nature of the observed dielectric relaxation behavior of the as-, Ar- and O_2-samples, the values of the dielectric spectra were fitted the Cole-Cole equation (Eq. (6.1)). The Cole-Cole fitting's results for the as-, Ar- and O_2-samples are shown in Figures 6.35 - 6.37 ((a) - (f)), respectively. The results of the Cole-Cole fitting for the samples calcined at different temperatures are shown in the Tables 6.7 - 6.9. It is clearly seen from Figures 6.35 - 6.36 ((a) - (f)) and Figure 6.37 ((a) - (c)) that the relaxation time can be well fitted with the Cole-Cole equation, indicating that the relaxation time of these samples are the Debye-type relaxation. The values are obtained to be 0.88, 0.93, 0.75(1), 0.93(2) for the as-, Ar- and O_2-CuO5-PRa (Figures 6.35 ((a) - (c))), and 0.88, 0.93, 0.72(1) and 0.89(2) for as-, Ar- and O_2-CuO5-PRb (Figures 6.35 ((d) - (f))). Whereas, Figure 6.36 ((a) - (f)) shows well fitted with the Cole-Cole equation for the sample prepared from the powders calcined at 600°C and the α values are obtained to be 0.76(1), 0.85(2), 0.71, 0.67 for the as-, Ar- and O_2-CuO6-PRa (Figures 6.36 ((a) - (c))); and 0.85, 0.91, 0.72 for as-, Ar- and O_2-CuO6-PRb (Figures 6.36 ((d) - (f))). Similarly, the well fitted results for the sample prepared from the powders calcined at 700°C are shown in Figure 6.37 ((a) - (f)) and the values of α are obtained to be 0.88, 0.93 and 0.74 for the as-, Ar- and O_2-CuO7-PRa (Figure 6.37 ((a) - (c))). Whereas, for those of the as-, Ar- and O_2-CuO7-PRb cannot fitted with the Cole-Cole equation because there is no relaxation time for these samples due to the phase changes of the CuO by the high calcined temperature (700°C) and sintered at 950°C.

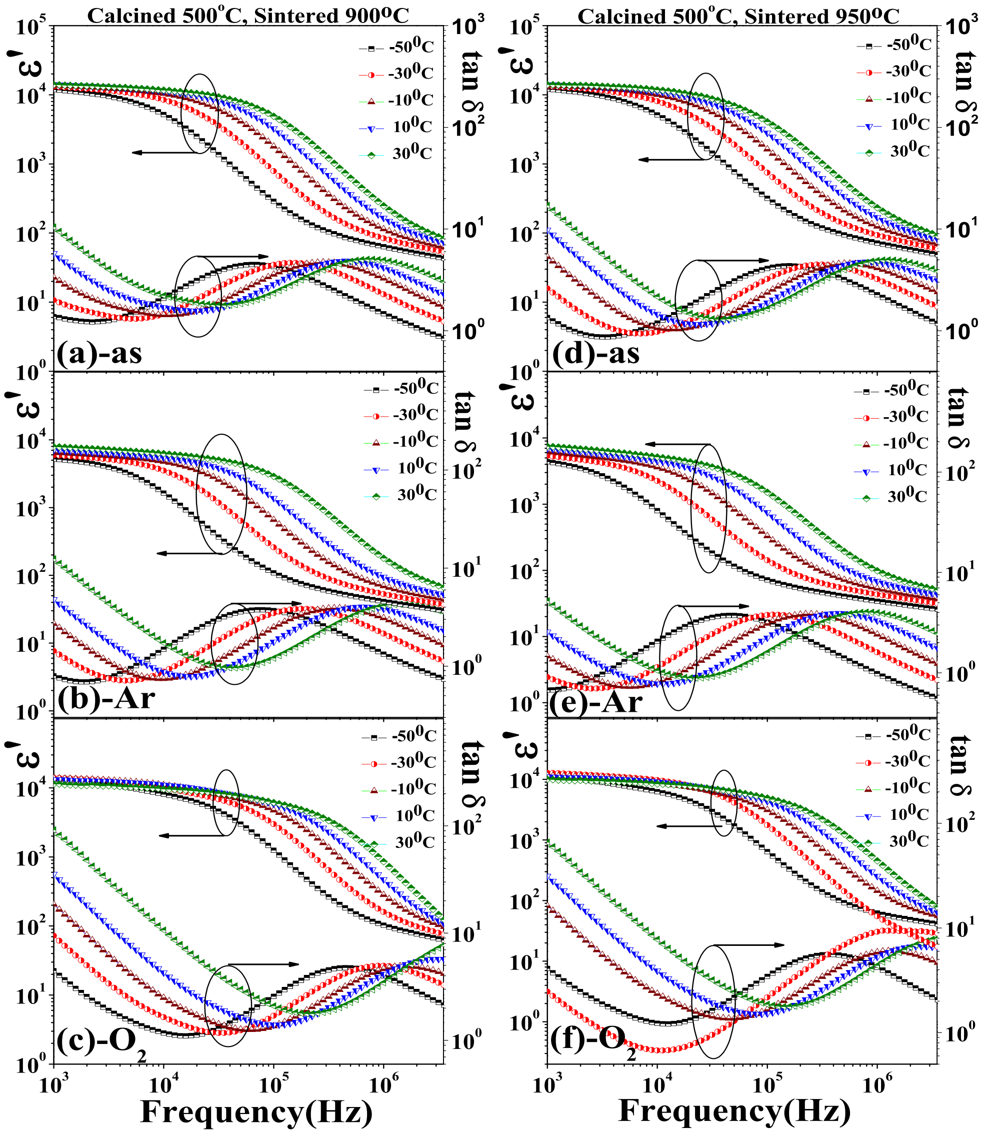

Figure 6.29 Frequency dependence of the dielectric constant (left axis) and dielectric loss tangent (right axis) for the as-CuO5-PRa (a), Ar-CuO5-PRa (b), O_2-CuO5-PRa (c), as-CuO5-PRb (d), Ar-CuO5-PRb (e) and O_2-CuO5-PRb (f) samples, respectively.

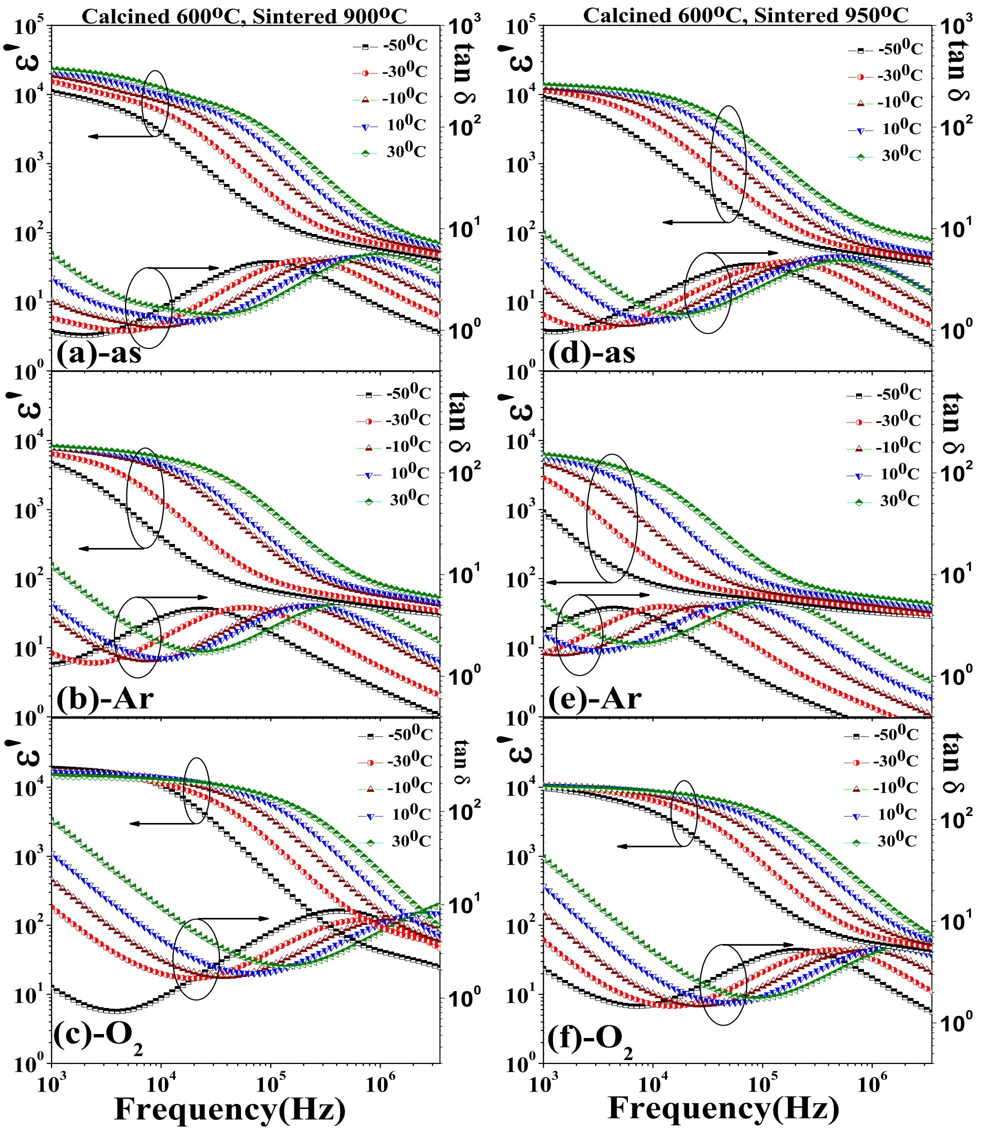

Figure 6.30 Frequency dependence of the dielectric constant (left axis) and dielectric loss tangent (right axis) for the as-CuO6-PRa (a), Ar-CuO6-PRa (b), O_2-CuO6-PRa (c), as-CuO6-PRb (d), Ar-CuO6-PRb (e) and O_2-CuO6-PRb (f) samples, respectively.

The relaxation time of all samples can be obtained by the Arrhenius law (Eq. (6.2)). The fitted curves are shown in the insets of Figures 6.35 - 6.36 ((a) - (f)) and Figure 6.37 ((a) - (c)). The values of relaxation time (τ) of the as-, Ar-, O_2-CuO5-PRa and as-, Ar-, O_2-CuO5-PRb samples are shown in the Table 6.7. In general, the relaxation time decreases with increasing temperature.

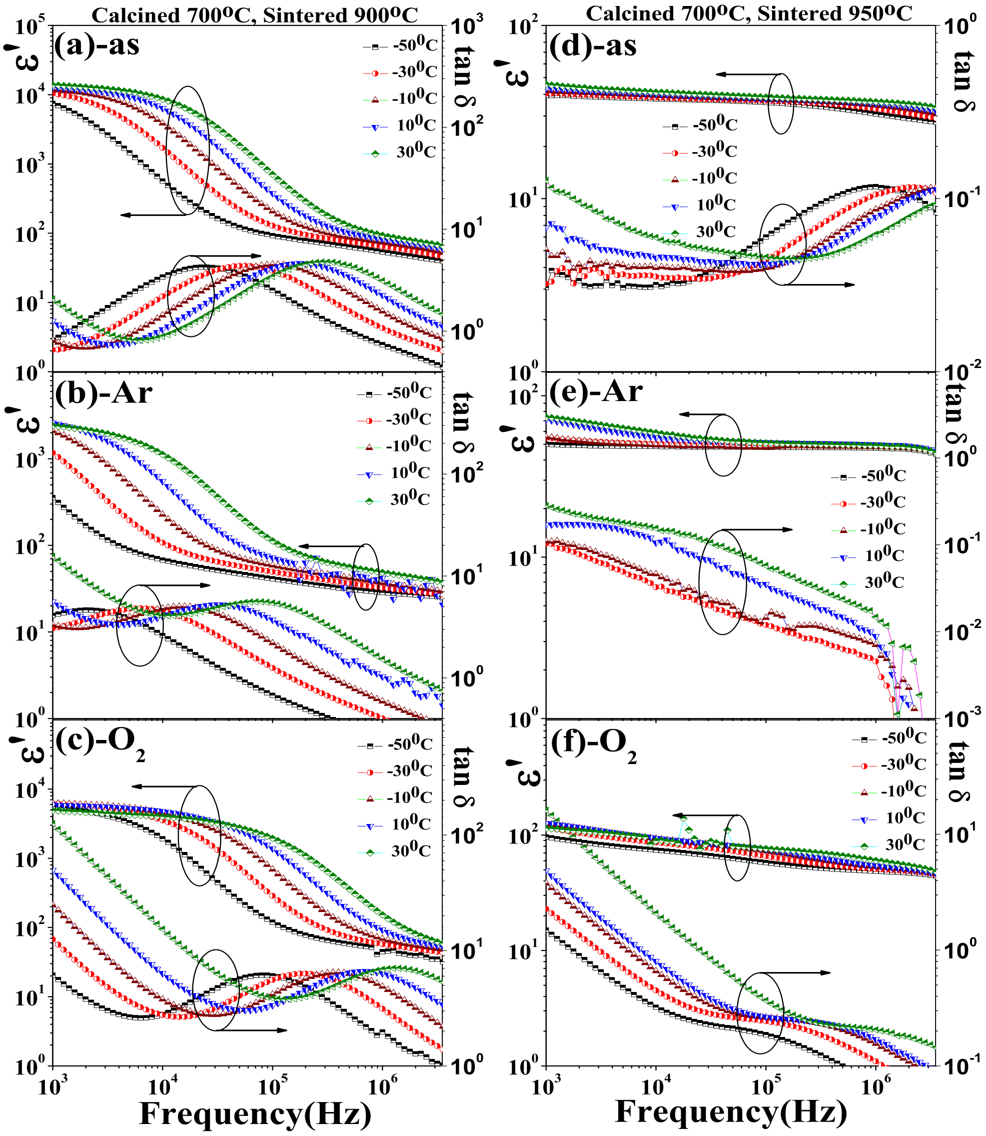

Figure 6.31 Frequency dependence of the dielectric constant (left axis) and dielectric loss tangent (right axis) for the as-CuO5-PRa (a), Ar-CuO7-PRa (b), O_2-CuO7-PRa (c), as-CuO7-PRb (d), Ar-CuO7-PRb (e) and O_2-CuO7-PRb (f) samples, respectively.

At low temperature the relaxation times of the Ar-CuO5-PRa and Ar-CuO5-PRb samples are higher than those of the as-Ar-CuO5-PRa and as-CuO5-PRb, then the relaxation times decrease and occur twice for the O_2-CuO5-PRa and O_2-CuO5-PRb. The relaxation time of the as-CuO6-PRa occurs twice as shown in Table 6.8, while those of the O_2-CuO6-PRa and O_2-CuO6-PRb occur only one compared with

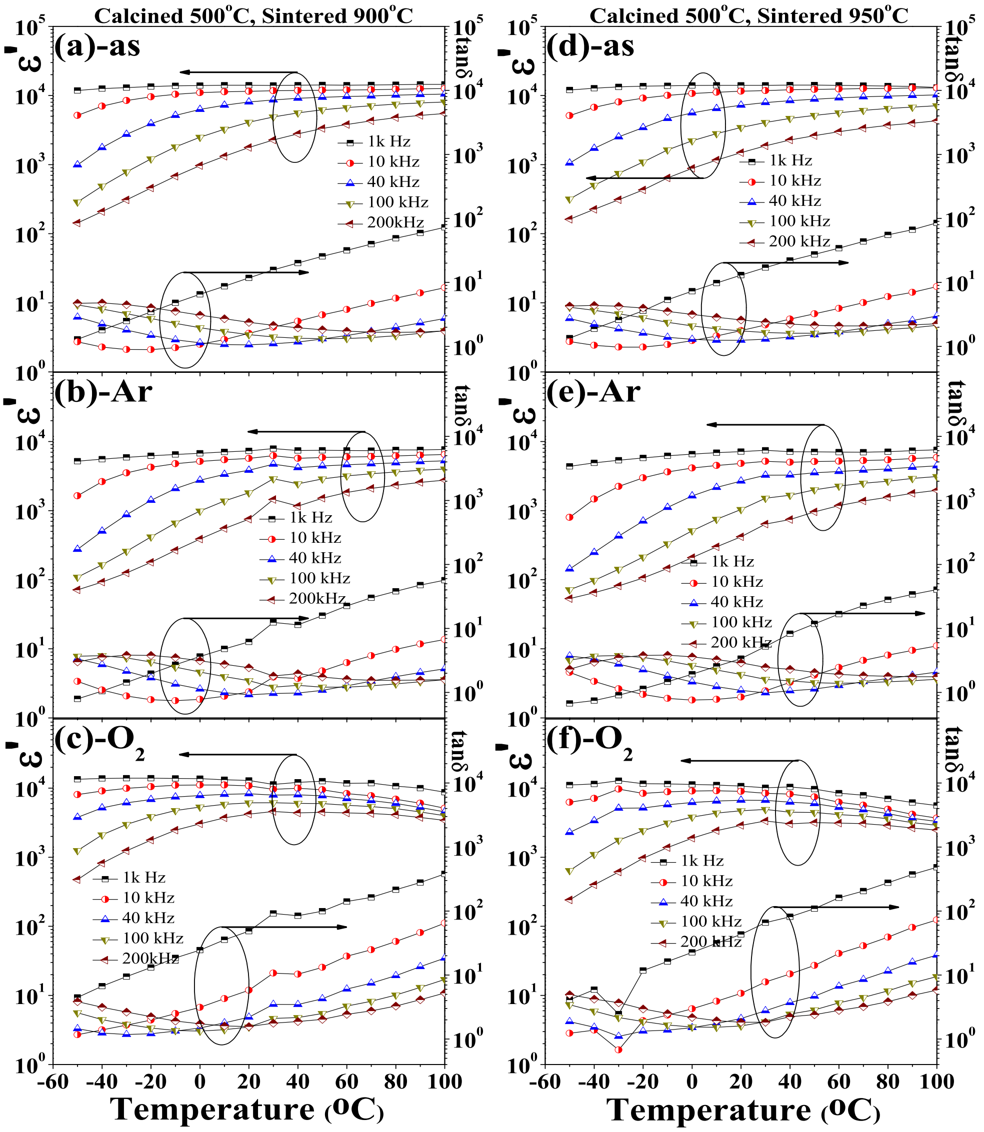

Figure 6.32 Temperature dependence of the dielectric constant (left axis) and dielectric loss tangent (right axis) for the as-CuO5-PRa (a), Ar-CuO5-PRa (b), O_2-CuO5-PRa (c), as-CuO5-PRb (d), Ar-CuO5-PRb (e) and O_2-CuO5-PRb (f) samples, respectively.

the O_2-CuO5-PRa and O_2-CuO5-PRb. No relaxation time was observed in the O_2-CuO7-PRb sample as shown in Table 6.9. The values of activation energy (E_τ) are obtained to be 0.144, 0.200, 0.144(1) and 0.133(2) eV; 0.134, 0.205, 0.145(1) and 0.142(2) eV for the as-, Ar-, O_2-CuO5-PRa and as-, Ar-, O_2-CuO5-PRb samples, respectively. For the as-, Ar-, O_2-CuO6-PRa and as-, Ar-, O_2-CuO6-PRb samples,

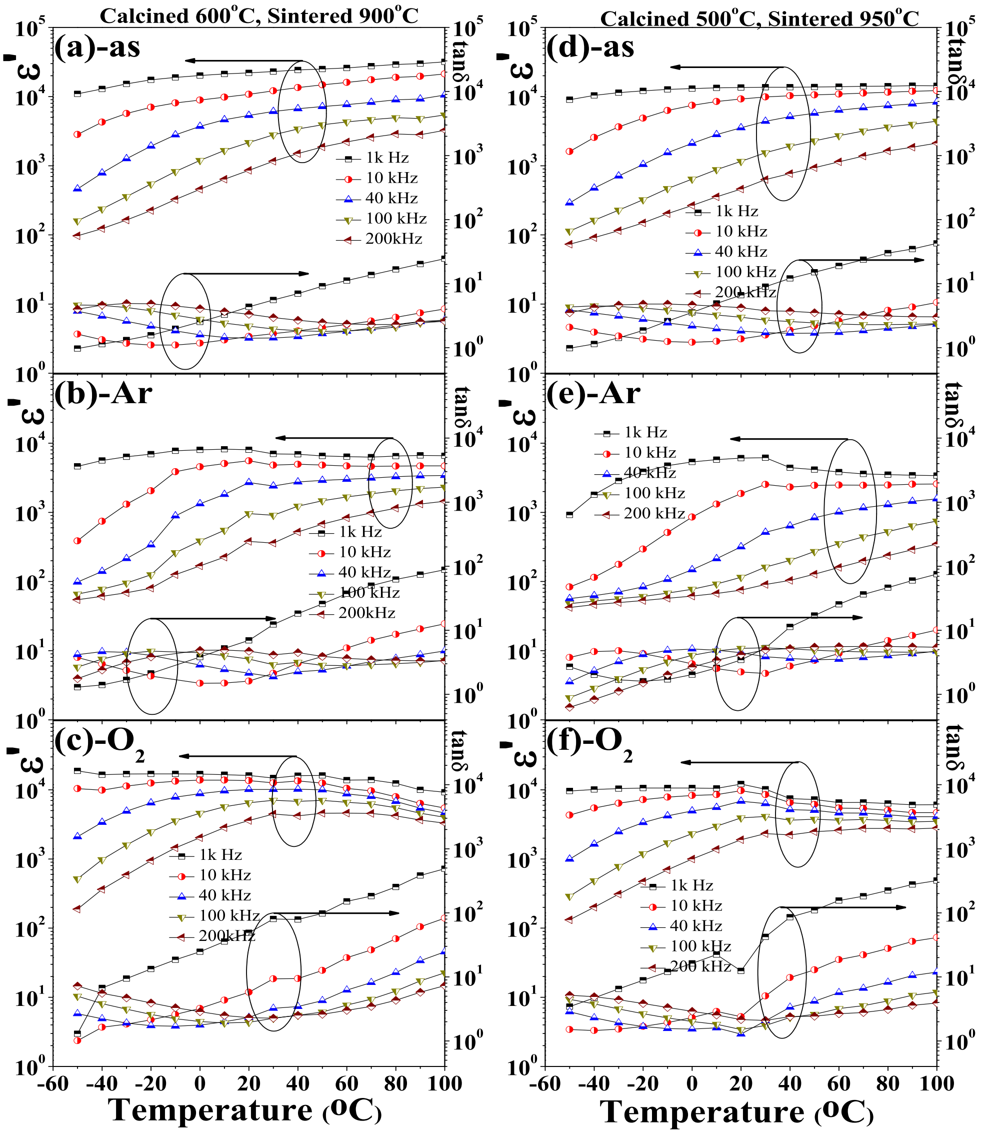

Figure 6.33 Temperature dependence of the dielectric constant (left axis) and dielectric loss tangent (right axis) for the as-CuO6-PRa (a), Ar-CuO6-PRa (b), O_2-CuO6-PRa (c), as-CuO6-PRb (d), Ar-CuO6-PRb (e) and O_2-CuO6-PRb (f) samples, respectively.

the E_τ values are obtained to be 0.169(1), 0.158(2), 0.212; 0.170 and 0.153; 0.205; 0.167 eV, respectively. Finally, the activation energy values of the as-, Ar-, O_2-CuO7-PRa are 0.177, 0.231 and 0.181 eV, respectively.

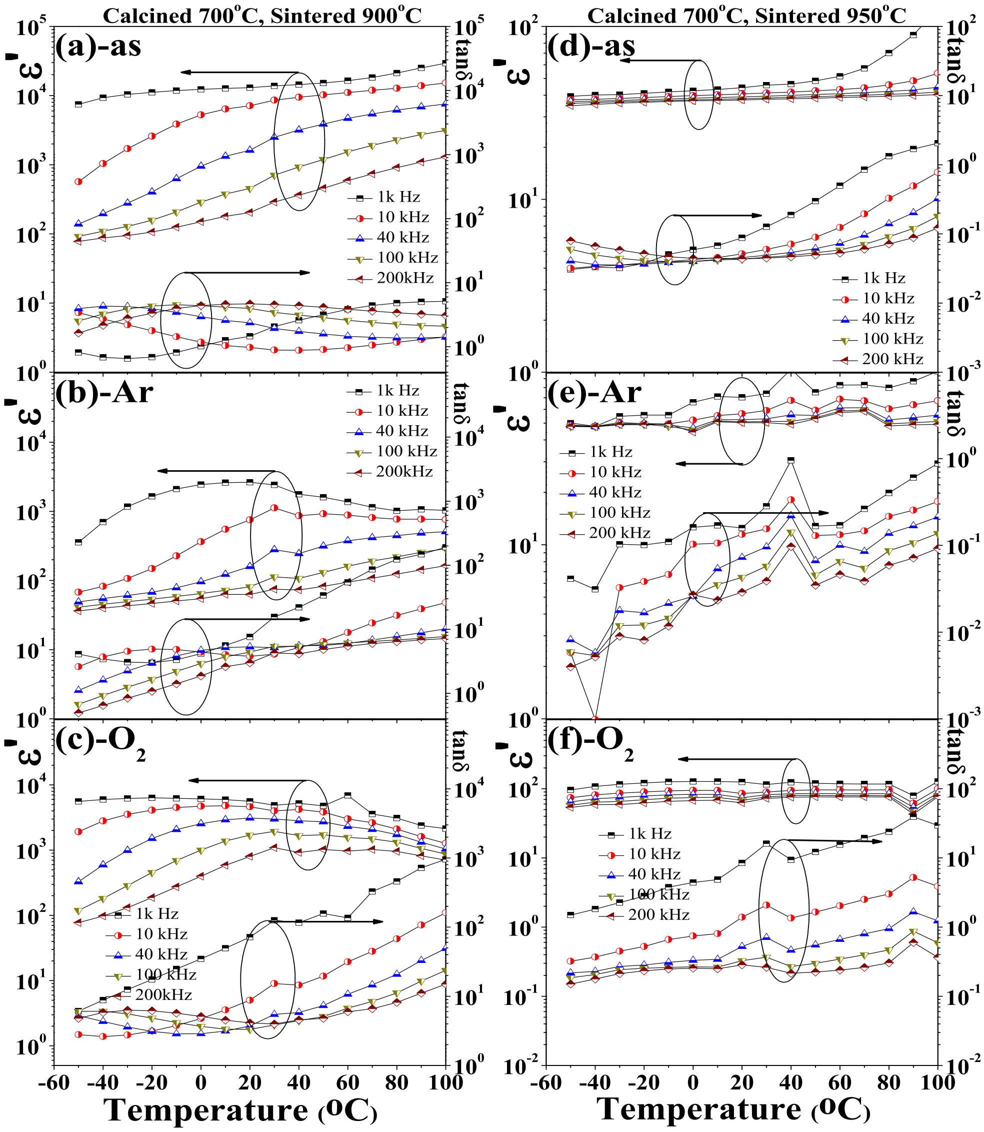

Figure 6.34 Temperature dependence of the dielectric constant (left axis) and dielectric loss tangent (right axis) for the as-CuO7-PRa (a), Ar-CuO7-PRa (b), O_2-CuO7-PRa (c), as-CuO7-PRb (d), Ar-CuO7-PRb (e) and O_2-CuO7-PRb (f) samples, respectively.

6.3.2 The impedance analysis

In order to understand the responses of the dielectric dispersion of the samples prepared by the PR method, the complex impedance analysis was performed. By using the complex impedance, Z^*, plots (Figures 6.38 - 6.40 ((a) - (f))) most samples show a large semicircle at low frequencies with a small semicircle at a

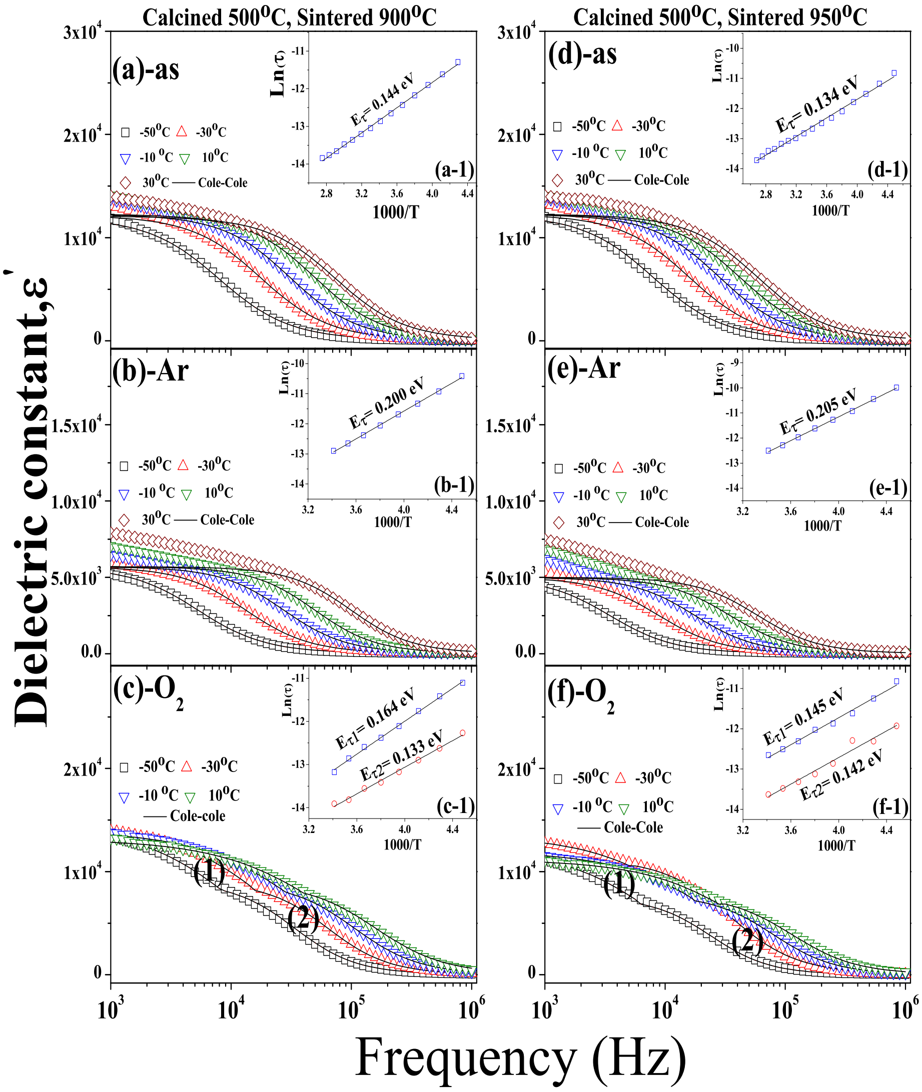

Figure 6.35 The frequency dependence of ε' at various temperatures (the solid lines represent calculated values of Cole-Cole equation) and Arrhenius plots of the dielectric relaxation time (inset) (a-1) to (f-1) for the as-CuO5-PRa (a), Ar-CuO5-PRa (b), O_2-CuO5-PRa (c), as-CuO5-PRb (d), Ar-CuO5-PRb (e), and O_2-CuO5-PRb (f) samples, respectively.

higher frequency (insets of Figures 6.38 - 6.40 ((a) - (f))). The data were interpreted using an equivalence circuit of two parallel *RC* elements connected in series, as reported by Sakar et al., (2008a) and Tongbai et al., (2008a). However, the complex impedance, Z^*, plots of the as-, Ar- and O_2-CuO7-PRb samples (Figure 6.40 ((d) - (f))) do not show semicircles due to the effect of high resistant in

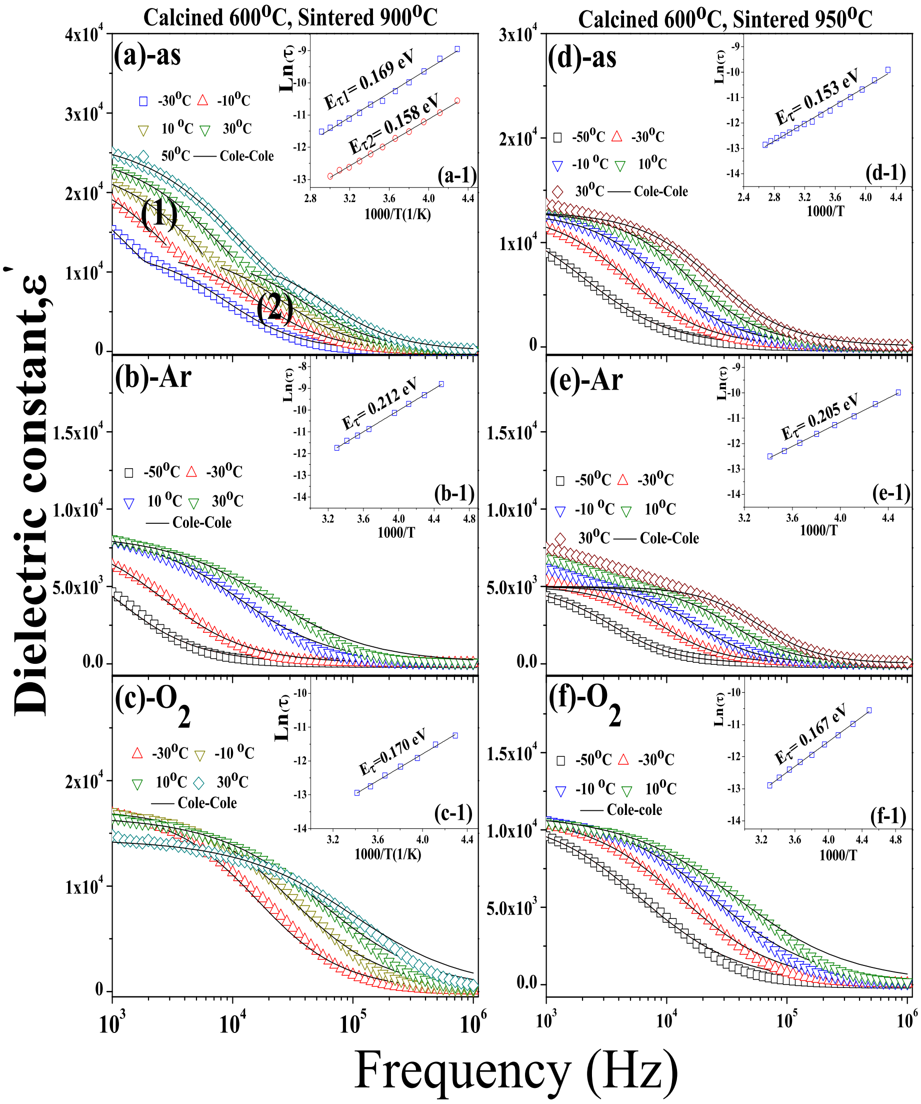

Figure 6.36 The frequency dependence of ε' at various temperatures (the solid lines represent calculated values of Cole-Cole equation) and the Arrhenius plots of the dielectric relaxation time (inset) (a-1) to (f-1) for the samples as-CuO6-PRa (a), Ar-CuO6-PRa (b), O_2-CuO6-PRa (c), as-CuO6-PRb (d), Ar-CuO6-PRb (e), and O_2-CuO6-PRb (f), respectively.

the samples.

When the temperatures increase from -50°C to 0°C the R_{int} and R_{ext} values of the as-CuO5-PRa (Figure 6.38 (a)) decrease from $1.37 \times 10^4\Omega$ to $2.7 \times 10^3\Omega$ and $1.3 \times 10^5\Omega$ to $1.74 \times 10^4\Omega$, respectively. Those of the as-CuO5-PRb samples (Figure 6.38 (d)) decrease from $1.35 \times 10^4\Omega$ to $2.95 \times 10^3\Omega$ and $1.17 \times 10^5\Omega$ to

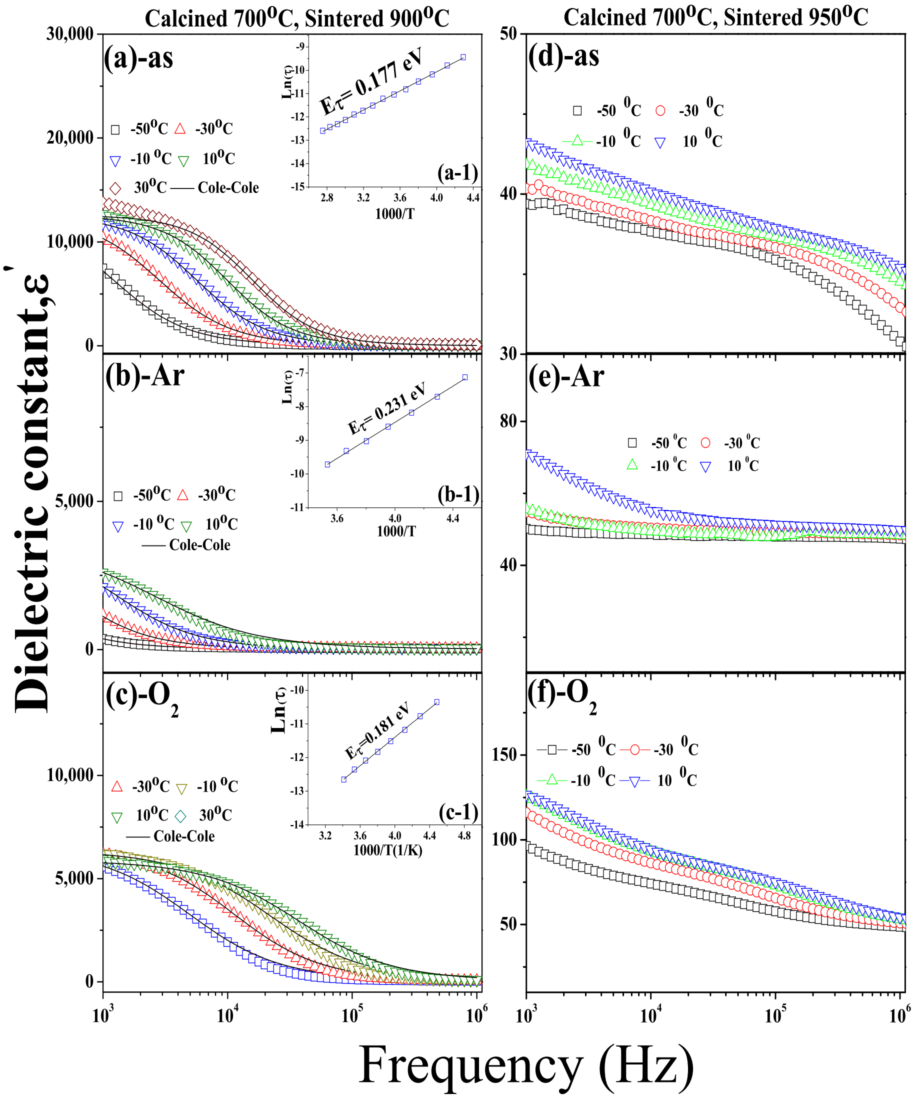

Figure 6.37 The frequency dependence of ε' at various temperatures (the solid lines represent calculated values of Cole-Cole equation) and the Arrhenius plots of the dielectric relaxation time (inset) (a-1) to (c-1) for the samples as-CuO7-PRa (a), Ar-CuO7-PRa (b), O_2-CuO7-PRa (c), as-CuO7-PRb (d), Ar-CuO7-PRb (e), and O_2-CuO7-PRb (f), respectively.

$1.5 \times 10^4\Omega$, respectively. While the R_{int} and R_{ext} values of the Ar-CuO5-PRa samples (Figures 6.38 (b) and 6.38 (e)) decreased from $4.55 \times 10^4\Omega$ to $6.7 \times 10^3\Omega$ and $5.88 \times 10^5\Omega$ to $6.8 \times 10^4\Omega$; for those of the Ar-CuO5-PRb decreasing from $8.1 \times 10^4\Omega$ to $1.11 \times 10^4\Omega$ and $1.49 \times 10^6\Omega$ to $1.5 \times 10^5\Omega$ respectively. Figure 6.38 ((c) and (f)) shows the R_{int} and R_{ext} values decreasing from $3.7 \times 10^3\Omega$ to

Table 6.7 Relaxation times of the as-, Ar-, O_2-CuO5-PRa and as-, Ar-, O_2-CuO5-PRb samples in the temperature range from -50°C to 30°C.

Temperature	CuO5-PRa				CuO5-PRb			
($°C$)	as-τ	Ar-τ	O_2-$\tau(\mu s)$		as-τ	Ar-τ	O_2-$\tau(ms)$	
	(μs)	(μs)	(1)	(2)	(μs)	(μs)	(1)	(2)
-50	20	30	15	4.7	20	46	20	6.6
-40	12.5	18	11	3.3	14	29	13	4.5
-30	9	12	7.8	2.5	10	18	9	4.6
-20	6.8	8.4	5.5	1.9	7.6	12.7	7	2.6
-10	5.15	5.8	4.2	1.5	5.6	9	6	2
0	4	4.2	3.4	1.3	4.5	6.3	4.5	1.65
10	3.2	3.2	2.6	1	3.8	4.6	3.7	1.4
20	2.6	2.5	1.9	0.91	3.15	3.7	3.2	1.2
30	2.16	1.6	-	-	2.7	2.7	-	-

Table 6.8 Relaxation times of the as-, Ar-, O_2-CuO6-PRa and as-, Ar-, O_2-CuO6-PRb samples in the temperature range from -50°C to 30°C.

Temperature	CuO6-PRa				CuO6-PRb		
($°C$)	as-$\tau(\mu s)$		Ar-τ	O_2-τ	as-τ	Ar-τ	O_2-τ
	(1)	(2)	(μs)	(μs)	(μs)	(μs)	(μs)
-50	-	38	150	15	76	530	26
-40	130	26	90	13	50	300	17
-30	96	18	60	10	33	200	12
-20	65	13.5	40	6.7	23	130	9
-10	46	10	20	5.2	17	85	6.5
0	35	8.1	19	4	13	63	5.2
10	26	6.2	14.1	2.9	10	42	4.1
20	23	5	11	2.4	8.5	32	3.2
30	18	4	8	1.6	6.5	24	2.5

$8.7 \times 10^2\Omega$ and $2.2 \times 10^4\Omega$ to $3.7 \times 10^3\Omega$ for the O-CuO5-PRa; from $6.17 \times 10^3\Omega$ to $1.35 \times 10^3\Omega$ and $2.9 \times 10^4\Omega$ to $4.8 \times 10^3\Omega$ for the O_2-CuO5-PRb, respectively.

Figures 6.39 (a) and 6.39 (d) reveal that the R_{int} and R_{ext} values are decreased from $2.43 \times 10^4\Omega$ to $4.45 \times 10^3\Omega$ and $3.88 \times 10^5\Omega$ to $3.68 \times 10^4\Omega$; from $3.74 \times 10^4\Omega$ to $6.9 \times 10^3\Omega$ and $3.3 \times 10^5\Omega$ to $3.33 \times 10^4\Omega$ when the temperatures are increased from -50°C to 0°C for the as-CuO6-PRa and as-CuO6-PRb, respectively.

Table 6.9 Relaxation times of the as-, Ar-, O_2-CuO7-PRa and as-, Ar-, O_2-CuO7-PRb samples in the temperature range from -50°C to 30°C.

Temperature ($°C$)	CuO7-PRa as-τ (μs)	CuO7-PRa Ar-τ (μs)	CuO7-PRa O_2-τ (μs)	CuO7-PRb as-τ (μs)	CuO7-PRb Ar-τ (μs)	CuO7-PRb O_2-τ (μs)
-50	130	30	32	-	-	-
-40	80	18	21	-	-	-
-30	56	12	14	-	-	-
-20	38	8.4	10	-	-	-
-10	28	5.8	7.3	-	-	-
0	20	4.2	5.6	-	-	-
10	16	3.2	4.3	-	-	-
20	13.5	2.5	3.2	-	-	-
30	10	1.6	3.2	-	-	-

While the R_{int} and R_{ext} values of the Ar-CuO6-PRa and Ar-CuO6-PRb (Figures 6.39 (b) and 6.39 (e)) decrease from $1.12 \times 10^5\Omega$ to $1.46 \times 10^4\Omega$ and $4.7 \times 10^5\Omega$ to $4.9 \times 10^4\Omega$; from $5.86 \times 10^5\Omega$ to $5.9 \times 10^4\Omega$ and 2.02×10^6 to 1.47×10^5, respectively. In addition, the R_{int} and R_{ext} values of O_2-CuO6-PRa and O_2-CuO6-PRb (Figures 6.39 (c) and (f)) are decreased from $6.5 \times 10^3\Omega$ to $1.2 \times 10^3\Omega$ and $7.7 \times 10^4\Omega$ to $3.14 \times 10^3\Omega$; from $1.27 \times 10^4\Omega$ to $2.44 \times 10^3\Omega$ and $4.44 \times 10^4\Omega$ to $8.1 \times 10^3\Omega$, respectively.

Figure 6.40 shows the complex, Z^*, impedance plots of the as-, Ar, and O_2-CuO7-PRb samples. Figures 6.40 ((a) - (c)) show the R_{int} and R_{ext} values decreasing from $8.4 \times 10^4\Omega$ to $1.39 \times 10^4\Omega$ and $1.58 \times 10^6\Omega$ to $1.59 \times 10^5\Omega$; from $1.1 \times 10^6\Omega$ to $1.01 \times 10^5\Omega$ and $1.3 \times 10^6\Omega$ to $9.56 \times 10^4\Omega$; from $2.38 \times 10^4\Omega$ to $3.9 \times 10^3\Omega$ and $2.8 \times 10^4\Omega$ to $4.2 \times 10^3\Omega$ for the as-CuO7-PRa, Ar-CuO7-PRa and O_2-CuO7-PRa, respectively. The complex impedance, Z^*, plots of the as-, Ar-CuO7-PRb (Figures 6.40 (d) and 6.40 (e)) shows higher resistance values ($> 1M\Omega$ at 1 kHz). The R_{ext} of the O_2-CuO7-PRb sample decreases from $1.6 \times 10^7\Omega$ to $3.7 \times 10^6\Omega$ as the temperature increases. The dielectric constant, dielectric loss

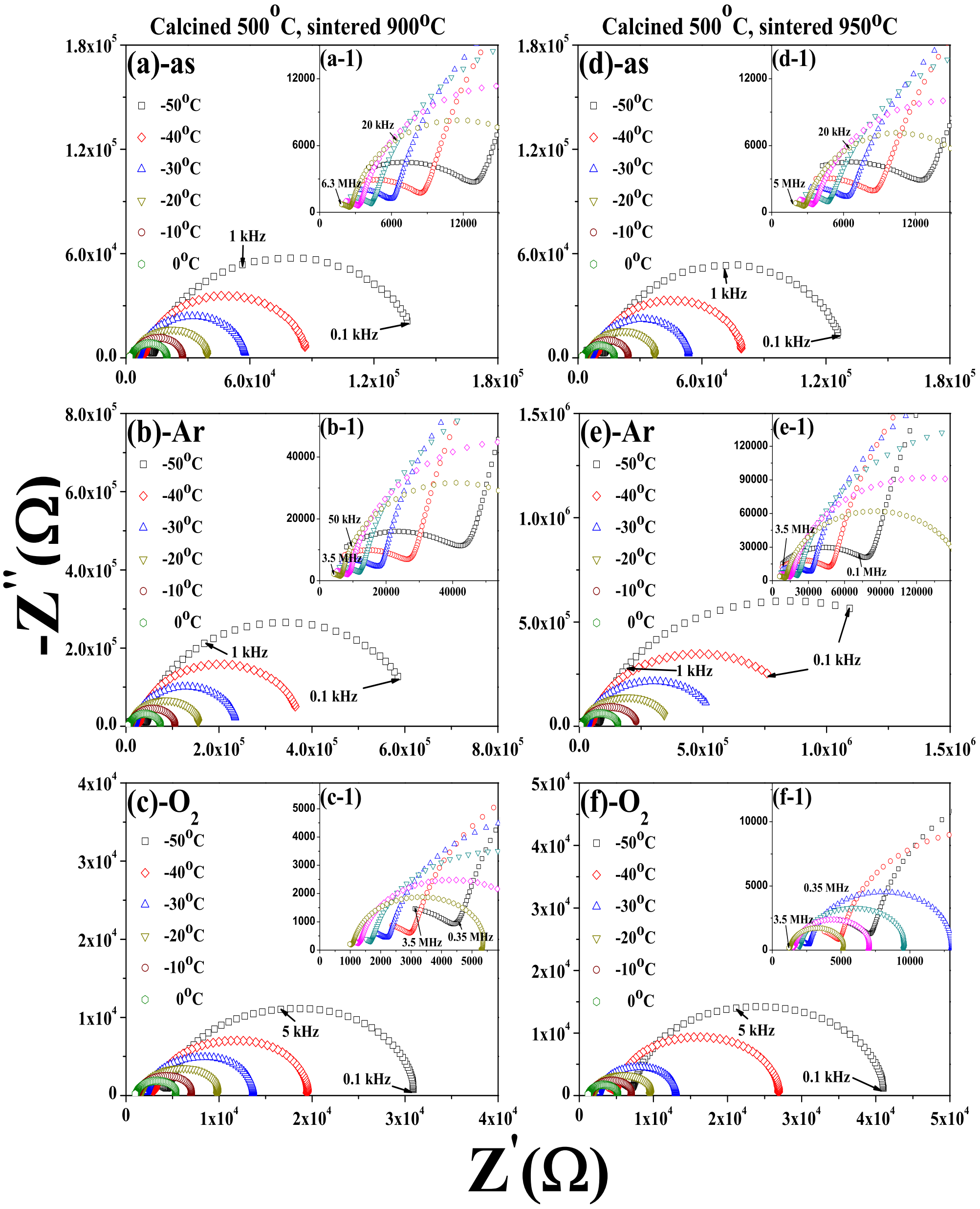

Figure 6.38 Complex impedance, Z^*, plots and the expanding scale at a high frequency (inset) for the as-CuO5-PRa (a), Ar-CuO5-PRa (b), O_2-CuO5-PRa (c), as-CuO5-PRb (d), Ar-CuO5-PRb (e) and O_2-CuO5-PRb (f) samples, respectively.

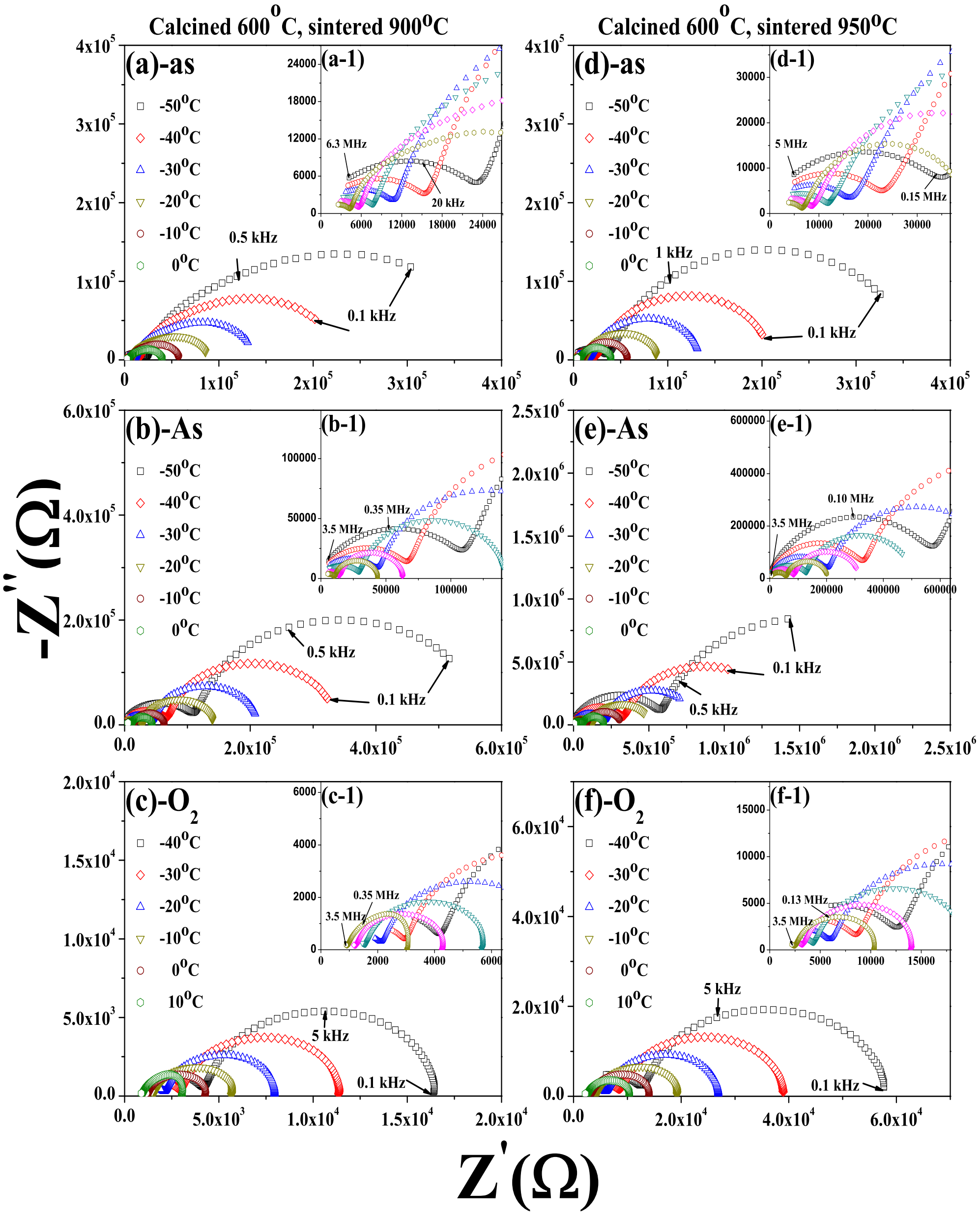

Figure 6.39 Complex impedance, Z^*, plots and the expanding scale at a high frequency (inset) for the as-CuO6-PRa (a), Ar-CuO6-PRa (b), O_2-CuO6-PRa (c), as-CuO6-PRb (d), Ar-CuO6-PRb (e) and O_2-CuO6-PRb (f) samples, respectively.

tangent, R_{int}, R_{ext}, Cint, Cext and the activation energy of these samples are summarized in Table 6.10.

Figures 6.41 (a) and 6.41 (d) demonstrate the dielectric constant, ε' of the as-, Ar-, O_2-CuO5-PRa and as-, Ar-, O_2-CuO5-PRb, respectively. The as-CuO5-

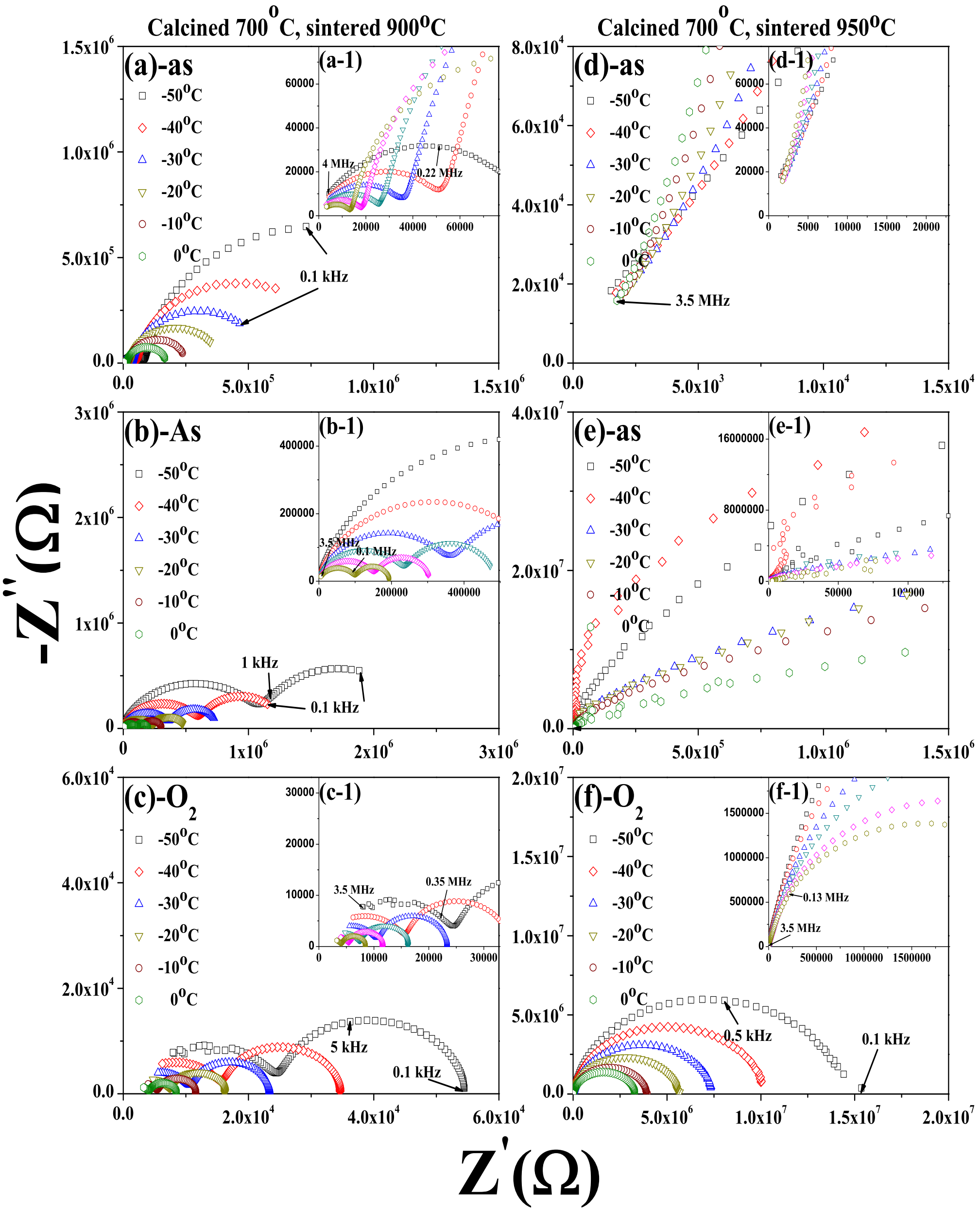

Figure 6.40 Complex impedance, Z^*, plots and the expanding scale at a high frequency (inset) for the as-CuO7-PRa (a), Ar-CuO7-PRa (b), O_2-CuO7-PRa (c), as-CuO7-PRb (d), Ar-CuO7-PRb (e) and O_2-CuO7-PRb (f) samples, respectively.

PRa and as-CuO5-PRb as-samples have dielectric constant values of 1.41×10^4 and 1.41×10^4; then they decrease to 7.9×10^3 and 7.48×10^3 for the Ar-CuO5-PRa and Ar-CuO5-PRb samples. After that, the dielectric constants increased to the values of 1.13×10^4 and 1.01×10^4 for the O_2-CuO5-PRa and O_2-CuO5-PRb,

Table 6.10 The dielectric constant, dielectric loss tangent activation energies, resistance and capacitance of internal and external part of the as-, Ar-, O_2-samples prepared from the powders calcined at 500 - 700°C and then sintered at 900°C (subscript a) and 950°C (subscript b) prepared by the PR method.

Samples	Dielectric (ε')	tanδ	Resistance (Ω)		Capacitance (nF)	Activation Energy (eV)	
			R_{ext}	R_{int}	$C_{\text{ext}}(1)(2)$	$E_{\tau 1}$	$E_{\tau 2}$
as-CuO5-PRa	14,000	15.7	6.9	1,400	2.08	0.144	-
Ar-CuO5-PRa	7,900	12.4	16,000	2,420	1.15	0.2	-
O_2-CuO5-PRa	11,300	91.6	1,040	430	1.40(0.66)	0.133	0.164
as-CuO5-PRb	14,049	17.1	5,900	1,610	2.15	0.134	-
Ar-CuO5-PRb	7,480	5.21	43,000	3,600	1.1	0.205	-
O_2-CuO5-PRb	10,100	65.9	1,700	690	1.36	0.142	0.145
as-CuO6-PRa	23,000	5.57	12,600	2,250	3.85(1.37)	0.169	0.158
Ar-CuO6-PRa	7,000	12.3	13,100	5,300	1.2	0.212	-
O_2-CuO6-PRa	14,800	80.2	1,000	540	2.11	0.17	-
as-CuO6-PRb	13,700	8.98	11,400	3,500	2.14	0.153	-
Ar-CuO6-PRb	6,170	5.28	37,000	20,400	1.04	0.205	-
O_2-CuO6-PRb	10,200	42.2	3,100	1,160	1.43	0.167	-
as-CuO7-PRa	13,800	2.07	61,100	6,800	2.32	0.177	-
Ar-CuO7-PRa	2,410	15.6	19,600	29,400	0.52	0.2	-
O_2-CuO7-PRa	4,870	126	1,200	1,600	0.77	0.181	-
as-CuO7-PRb	45.7	0.13	¿107		-	-	-
Ar-CuO7-PRb	73.8	28.3	¿106		-	-	-
O_2-CuO7-PRb	115	16.1	106		0.002	-	-

respectively. Figures 6.41 (b) and 6.41 (e) show 2.3×10^4 and 1.37×10^4 dielectric constant for the as-CuO6-PRa and as-CuO6-PRb; they are then decreased to 7.0×10^3 and 6.71×10^3 for the Ar-CuO6-PRa and Ar-CuO6-PRb samples. After that, these can be increased again to the values of 1.48×10^4 and 1.02×10^4 for the O_2-CuO6-PRa and O_2-CuO6-PRb samples. In addition, Figure 6.41 (c) reveals dielectric constant of about 1.38×10^4 for the as-CuO7-PRa, and then it decreases to 2.41×10^3 for the Ar-CuO7-PRa sample. The dielectric constant can be increased again to the value of 4.8×10^3 for the O_2-CuO7-PRa sample. While, the as-, Ar, and O_2-CuO7-PRb shows a small dielectric constant that might be caused by the small of free charge carrier or oxygen vacancy in the external past due to the high calcined temperature. This enhancement of the ε' of these sample is due to the oxygen vacancy in the sample as discussed in section 6.2.2. The dielectric constant, dielectric loss tangent, internal resistant (R_{int}), external resistant (R_{ext}), external capacitance and activation energy at room temperature of these samples prepared by the PR method are shown in Table 6.10.

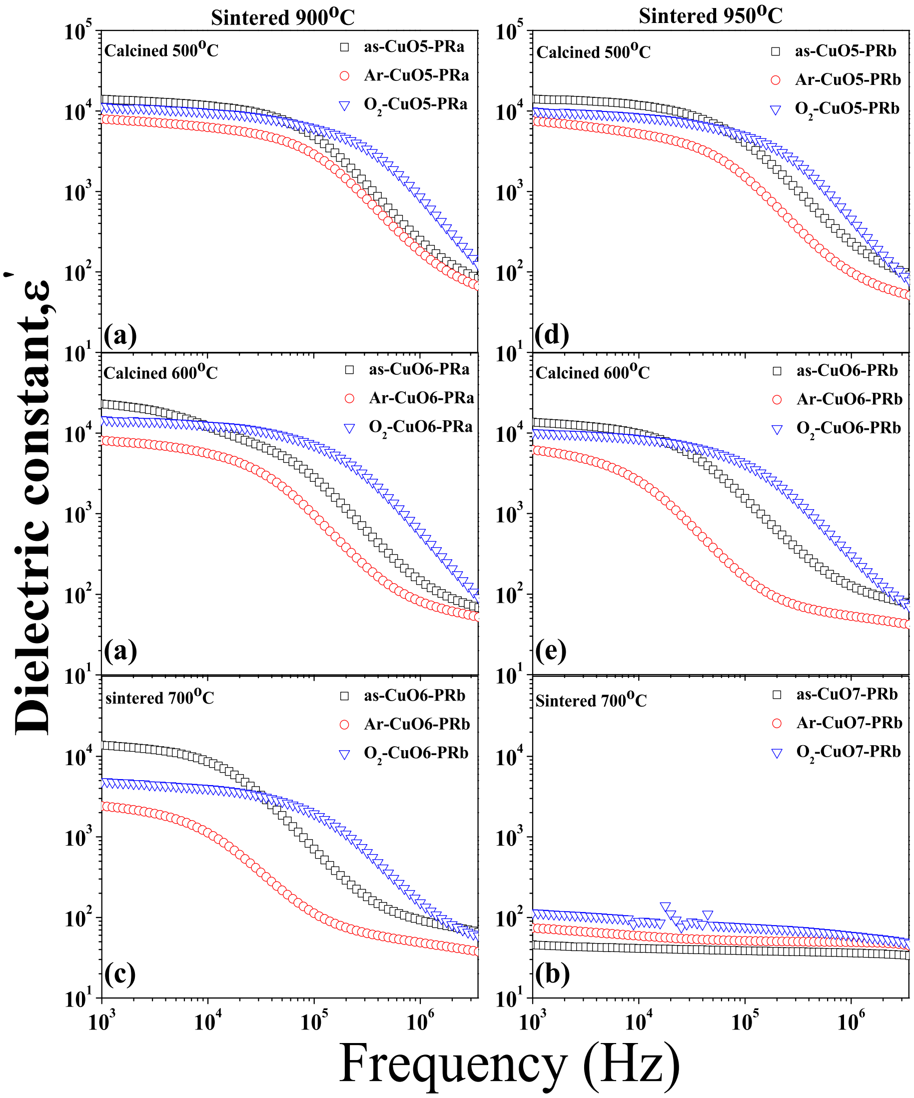

Figure 6.41 Frequency dependence of the dielectric constant at room temperature for the as-, Ar- and O_2-CuO5-PRa (a), as-, Ar- and O_2-CuO6-PRa (b), as-, Ar- and O_2-CuO7-PRa (c), as-, Ar- and O_2-CuO5-PRb (d), as-, Ar- and O_2-CuO6-PRb (e) and as-, Ar- and O_2-CuO7-PRb (f), respectively.

Figure 6.42 ((a) - (c)) compares the dielectric constants of the as-, Ar- and O_2-CuO5-PR; as-, Ar- and O_2-CuO6-PRa; as-, Ar- and O_2-CuO7-PR samples as a function of sintering temperature. While, Figure 6.42 ((d) - (f)) compares the dielectric loss tangent as a function of sintering temperature for the as-, Ar- and O_2-CuO5-PR; as-, Ar- and O_2-CuO6-PR; as-, Ar- and O_2-CuO7-PR samples. The ε' value of the as-CuO5-PRa sample is a little higher than those of the as-CuO5-PRb sample (Figure 6.42 (a)), and the values of both samples decrease in the Ar-samples. However, the ε' values of both samples can be increased again for the O_2-samples, whereas the tanδ (Figure 6.42 (d)) decreases but increases for the Ar- and O_2-samples, respectively. Similarly, the ε' and tanδ values for the as-, Ar-, O_2-CuO6-PRa and as-, Ar-, O_2-CuO6-PRb (Figures 6.42 (b) and 6.42 (e)). Figure 6.42 (c) and (f) compare the ε' and tanδ. The ε' and tanδ of the as-sample are decreased for Ar-sample and increased for O_2-sample sintered at 900°C, but the as-, Ar-, O_2-samples sintered at 950°C show small dielectric constant and dielectric loss tangent. The small dielectric constant of these samples might be due to the small of free charge carrier corresponding to the high resistance which was discussed previously and shown in the Figure 6.40 ((d) - (f)).

Figure 6.43 ((a) - (d)) compares the external resistant (R_{ext}) and internal resistant (R_{int}) of the as-, Ar- and O_2-samples prepared from the powders calcined at 500°C and 600°C as a function of sintering temperatures of 900°C and 950°C. The R_{ext} and R_{int} values of the as-CuO5-DTa, as-CuO5-DTb, as-CuO6-DTa and as-CuO6-DTb increase after the samples were annealed in argon and decrease after annealing in oxygen.

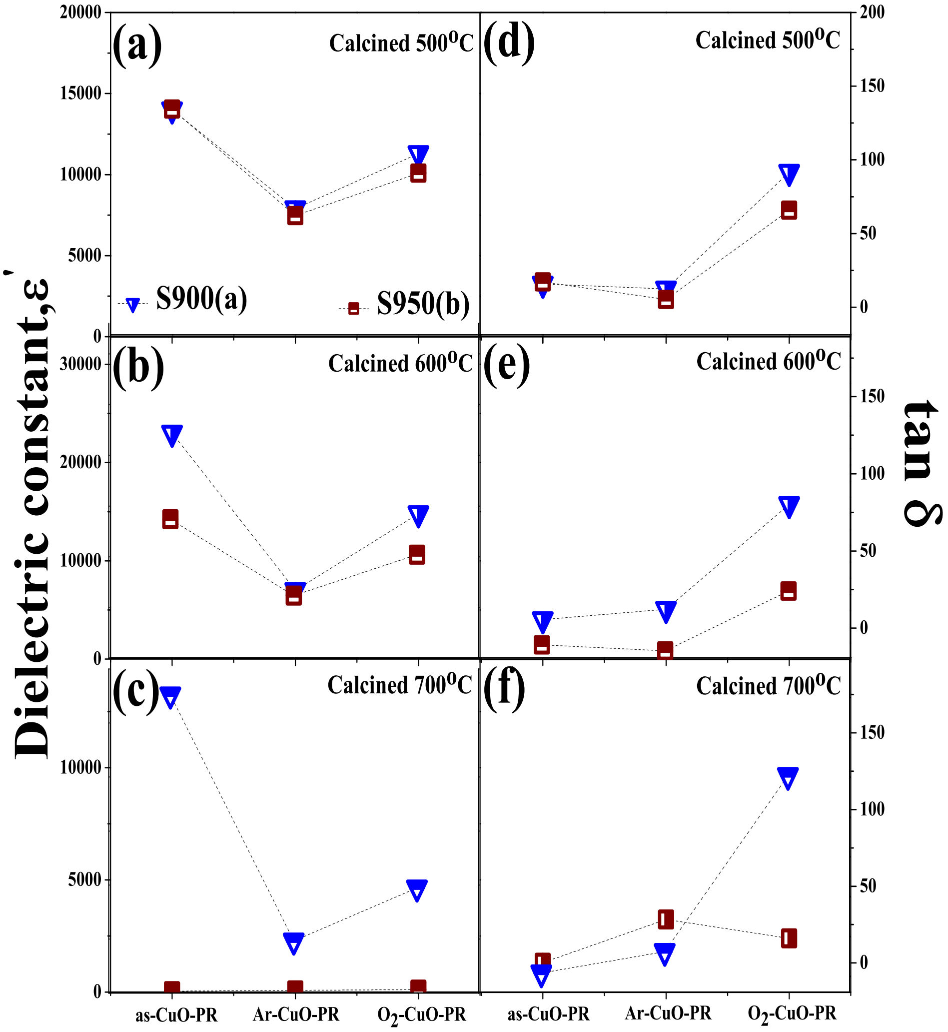

Figure 6.42 Dielectric constant (a) - (c) and dielectric loss tangent (d) - (f) of the as-, Ar- and O_2-samples prepared from the powders calcined at 500°C (a), 600°C (b) and 700°C (c) with the different sintering temperatures of 900°C (▽) and 950°C (□).

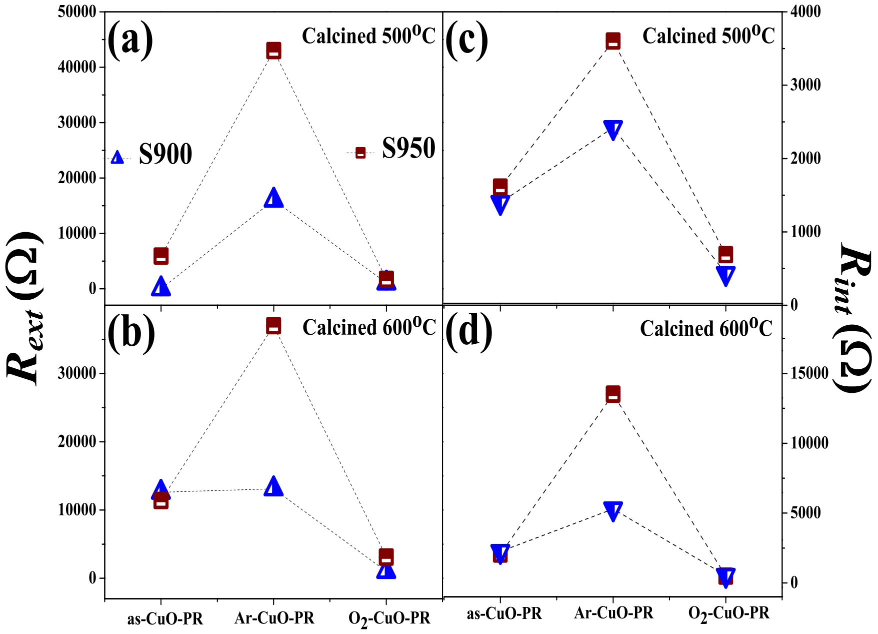

Figure 6.43 The external resistance (R_{ext}) (a) - (b) and internal resistance (R_{int}) (c) - (d) of the as-, Ar- and O_2-samples prepared from the powders calcined at 500°C and 600°C with different sintering temperatures of 900°C (▽) and 950°C (□).

6.3.3 Effect of dc-bias voltage

Figure 6.44 ((a) - (c)) shows the effect of the dc-bias voltage on the dielectric constant as a function of frequency (1 - 20 kHz) for the samples prepared from the powders calcined at 500, 600 and 700°C and then sintered at 900°C, respectively. In Figure 6.44 ((a) - (c)), the dielectric constant decreases with increasing the dc-bias voltage and it shows step decrease with increasing the frequencies (inset). Similarly, the dielectric constant decreases with increasing the dc-bias voltage for the as-samples sintered at 950°C (Figures 6.44 ((d) - (e))). In addition, the dielectric constant decreases with increasing frequencies (inset of Figures 6.44 ((a) - (e))). The decrease of the dielectric constant with the dc-bias voltage of the CuO sample prepared by the PR method is similar to those observed with the CuO sample prepared by using the commercial CuO powder and the DT method. The dielectric behavior of these samples was discussed in section 6.1.3. However the samples prepared from the PR method can be applied dc-bias voltage higher than the samples prepared by using the DT method, because the R_{ext} of the sample prepared from the DT method is smaller than that of the samples prepared by the PR method.

Figure 6.45 ((a) - (e)) show the complex impedance (Z^* plot at room temperature) containing a large semicircle correspond with the external resistance (R_{ext}) at low frequencies and small semicircle corresponds with the internal resistance (R_{int}) at a high frequencies. The R_{ext} and the dielectric constant decrease with increasing the dc-bias voltage (0 - 4 V). Namely, when voltages from 0 to 4 V were applied, the R_{ext} values for the samples prepared from the powders calcined at 500, 600 and 700°C and then sintered at 900°C (Figures 6.45 ((a) - (c))) decrease from 12300Ω to 530Ω ; from 3140Ω to 690Ω; from 8900Ω to 2200Ω, whereas, the R_{int} values remain constant at 1800Ω; 2840Ω and 11000Ω, respectively. Figure 6.45((d) - (e)) shows that the R_{ext} values for the samples prepared from the powders calcined at 500 and 600°C and sintered at 950°C decrease from 9600Ω to 530Ω; from 19000Ω to 1200Ω, while the R_{int} values remains constant at 2400Ω and 5200Ω, respectively. The CuO samples prepared from this method which calcined at 700°C and sintered at 950°C cannot be plotted for the complex impedance, Z^*, because the sample has a phase change has a high resistance. In this study, the capacitance bridge is not balanced at voltage over 30 V due to the large leakage current. When the dc-bias is over the limited balance, the charge carrier can be crossed the potential well of the external part, thus they are disappeared at external part (interfacial polarization) and then the total polarization is only contributed by the internal part. We think that part of the decrement in ε', due to

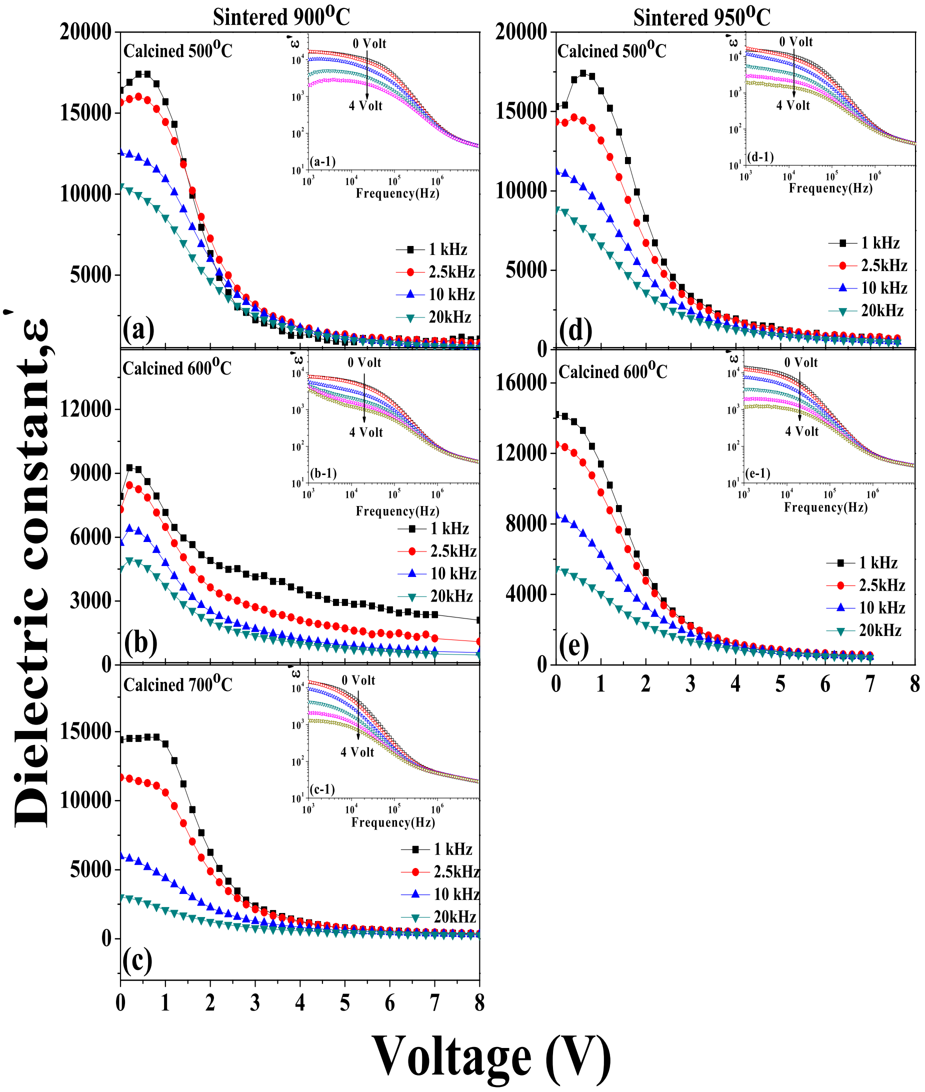

Figure 6.44 The effect of dc-bias voltage (0 - 8 V) on the dielectric constant as a function of frequency (1 - 20 kHz) and the insets show the dielectric constant as a function of dc-bias voltage of the as-CuO5-PRa (a), as-CuO6-PRa (b) and as-CuO7-PRa (c), as-CuO5-PRb (d) and as-CuO6-PRb (e), respectively.

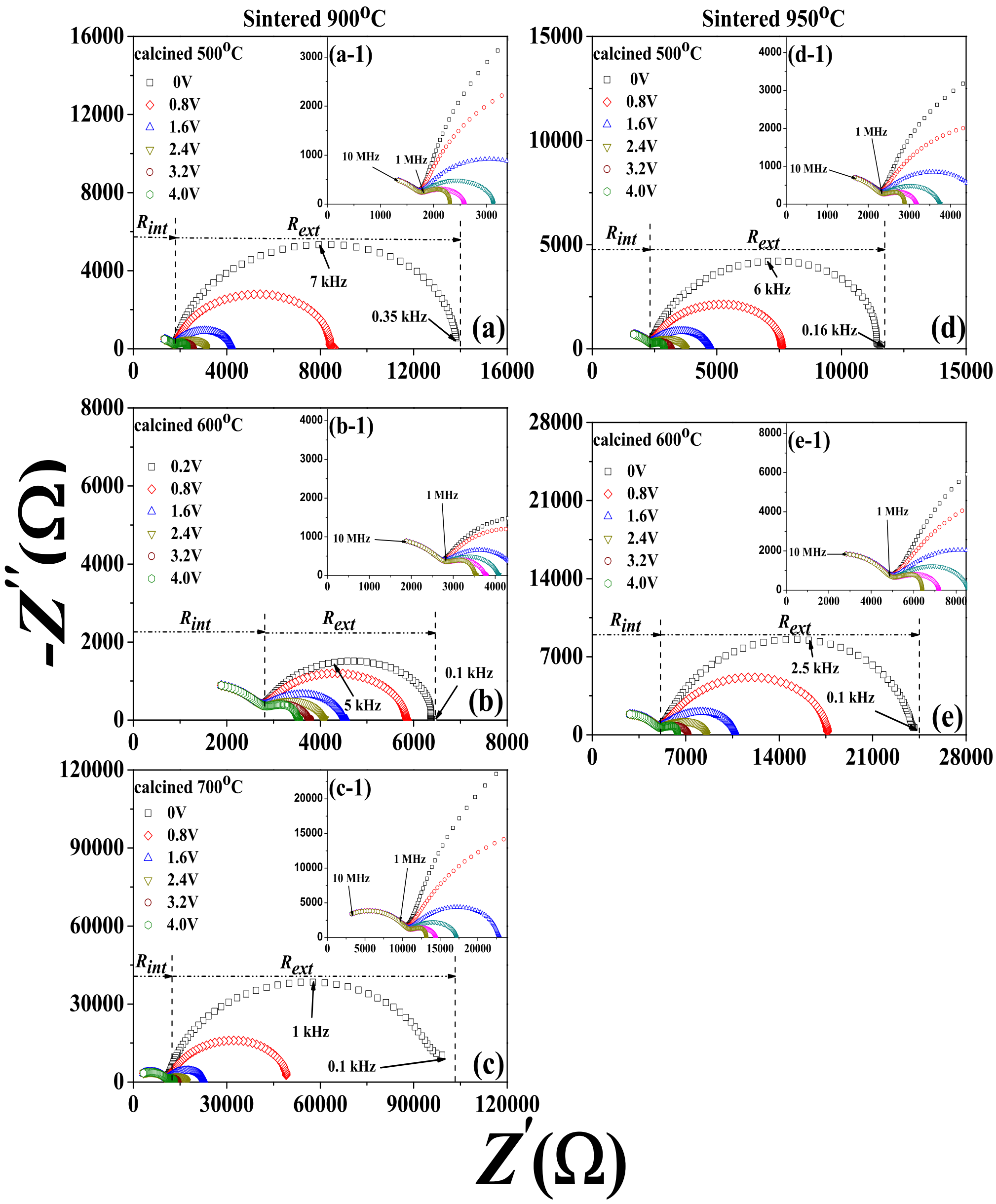

Figure 6.45 Complex impedance, Z^*, plots and the expanding scale at a high frequency (inset) at room temperature as a function of dc-bias voltage (0 - 4) of the as-CuO5-PRa (a), as-CuO6-PRa (b) and as-CuO7-PRa (c), as-CuO5-PRb (d) and as-CuO6-PRb (e), respectively. (the as-CuO7-PRb sample cannot plot the complex impedance, Z^*, plots).

the influence of dc-bias is contributed by external free charge and the remaining value of ε' beyond the limiting balance of the dc-bias voltage is contributed by internal part free charge. Therefore, the dc-bias voltage should have effect on the electrical properties of external part, whereas it has no effect on internal part as observed previously.

6.3.4 Effect of uniaxial compressive stress

In order to gain more understanding on the effect of the dc-bias voltage on the electrical properties (ε' and tanδ), the effect of uniaxial compressive stress on the dielectric constant, ε' and tanδ is investigated. Figures 6.46 ((a) - (c)) and 6.47 ((d) - (f)) show the stress dependence on dielectric constant (ε') as a function of 1, 2, 5, 10, 20 and 50 kHz for the as-samples prepared from the powders calcined at 500 - 700°C and sintered at 900°C (as-CuO5-PRa, as-CuO6-PRa, as-CuO7-PRa) and 950°C (as-CuO5-PRb, as-CuO6-PRb, as-CuO7-PRb), respectively. The changes of the dielectric constant and tanδ of these samples are similar to those observed of CuO samples prepared by using commercial CuO powder (section 6.1.4) and the PR method (section 6.2.4). Namely, the dielectric constant and tanδ with the applied stress can be divided into two regions. For the as-CuO5-PRa, as-CuO6-PRa, as-CuO7-PRa samples (Figures 6.46 ((a) - (c))), the dielectric constant is increased to the maximum values of 3.5×10^7 at 20 MPa (region 1); 2.2×10^7 at 50 MPa (region 1); and 4.5×10^7 at 35 MPa (region 1), respectively. After that the values of dielectric constant are decreased to 2.5×10^6 at 62 MPa (region 2) for the as-CuO5-PRa; 7.5×10^6 at 62 MPa (region 2) for the as-CuO6-PRa and 6.6×10^6 at 100 MPa (region 2) for the as-CuO7-PRa. Similar to those observed for the as-CuO5-PRb, as-CuO6-PRb, as-CuO7-PRb samples (Figure 6.46 ((d) - (f))), the values of dielectric constant are increased to the maximum value of 8.5×10^6 at 30 MPa (region 1); 4.6×10^6 at 25 MPa (region 1); and 5.3×10^4 at 25 MPa (region 1), respectively. Then these values are decreased to 3.3×10^6 at

62 MPa (region 2) for the as-CuO5-PRb; 3.7×10^6 at 74 MPa (region 2) for the as-CuO6-PRb and at 62 MPa (region 2) for the as-CuO7-PRb.

The behavior of tanδ as a function of compressive stress (0 - 100 MPa) is shown in Figures 6.47 ((a) - (f)). The tanδ is increased and decreased to the maximum and minimum value at the same compressive stress as the dielectric constant discussed in the Figures 6.46 ((a) - (f)). Namely, the tanδ values of the as-CuO5-PRa, as-CuO6-PRa, as-CuO7-PRa samples (Figures 6.47 ((a) - (c))), are increased to the maximum values of 295 at 20 MPa; 365 at 43 MPa (region 1); and 354 at 31 MPa (region 1), respectively. After that the values dielectric constant are decreased to 60 at 62 MPa (region 2) for the as-CuO5-PRa; 185 at 111 MPa (region 2) for the as-CuO6-PRa and 96 at 46 MPa (region 2) for the as-CuO7-PRa. Similar to those observed for the as-CuO5-PRb, as-CuO6-PRb, as-CuO7-PRb samples (Figures 6.47 ((d) - (f))) the values of dielectric constant are increased to the maximum values of 132 at 31 MPa (region 1); 178 at 31 MPa (region 1); and 50 at 31 MPa (region 1), respectively, then are decreased to 86 at 54 MPa (region 2) for the as-CuO5-PRb; 155 at 62 MPa (region 2) for the as-CuO6-PRb and 30 at 62 MPa (region 2) for the as-CuO7-PRb. The large ε' and tanδ values of these samples, occur in region 1, cause a sudden change in the external capacitance (electrode and surface layer) due to the uniaxial compressive stress as discussed in section 6.1.4.

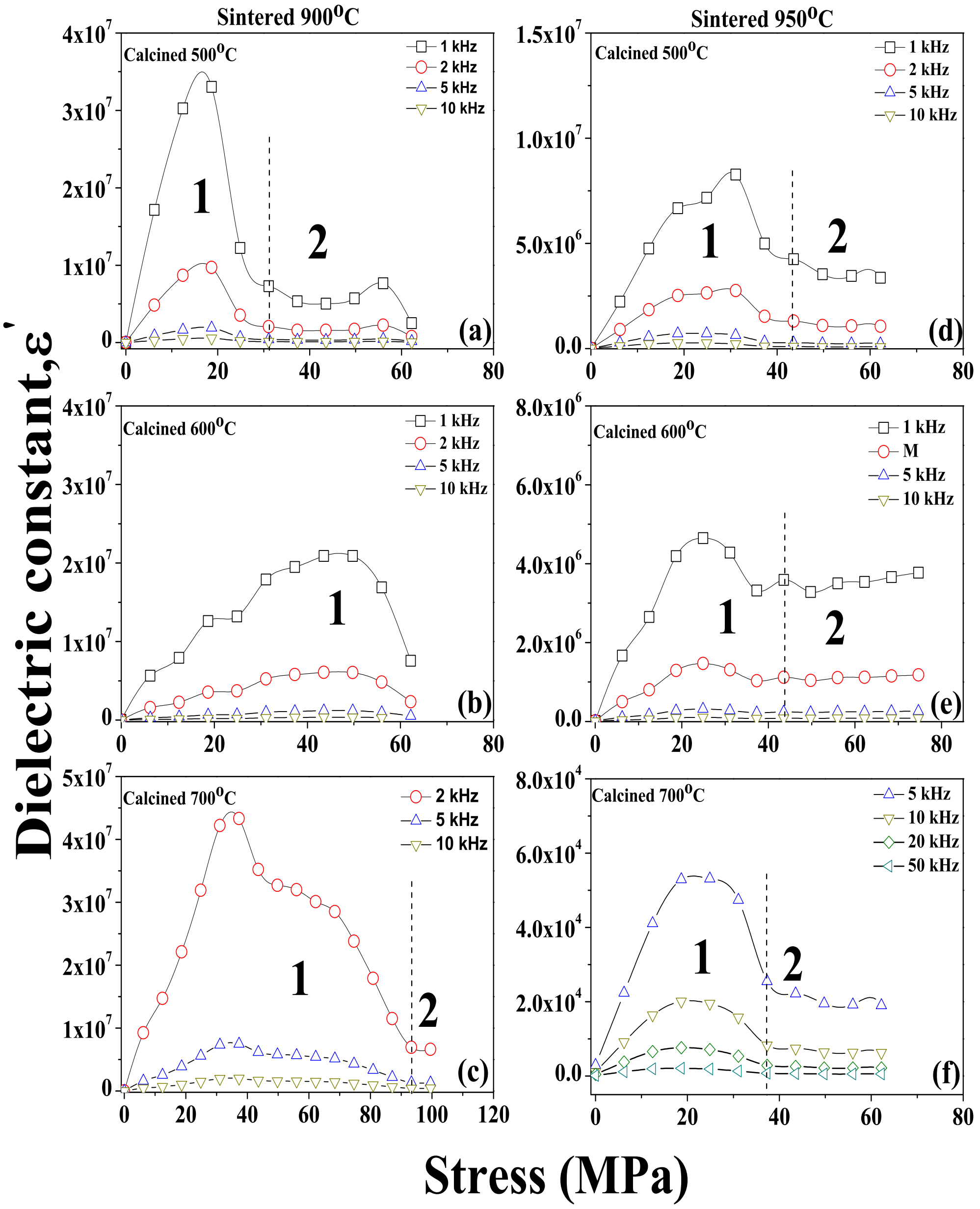

Figure 6.46 Effect of (0 - 100 MPa) uniaxial compressive stress on the dielectric constant for the as-CuO5-PRa (a), as-CuO6-PRa (b) and as-CuO7-PRa (c), as-CuO5-PRb(d), as-CuO6-PRb (e) and as-CuO7-PRb (f), respectively.

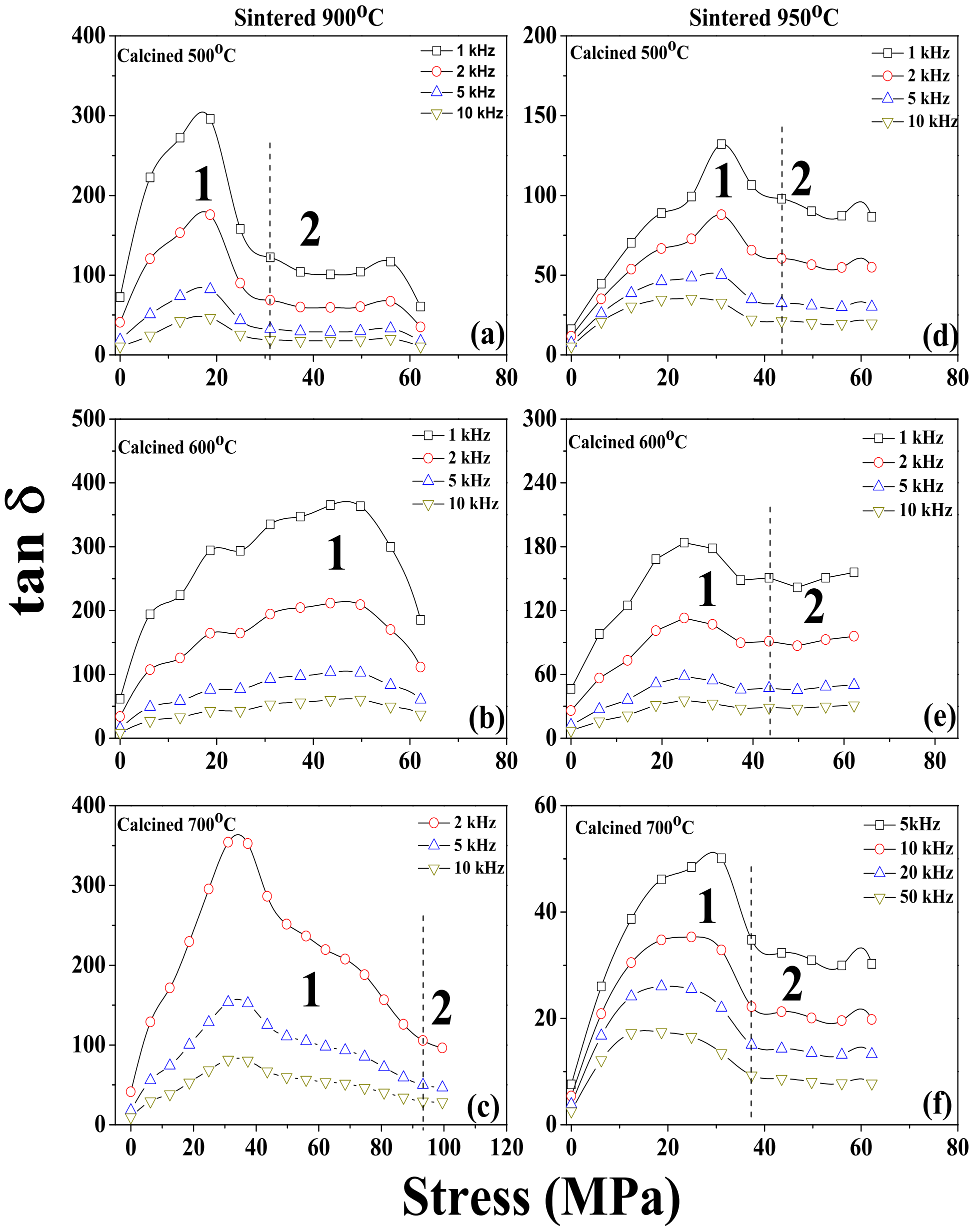

Figure 6.47 Effect of (0 - 100 MPa) uniaxial compressive stress on the dielectric loss tangent for the as-CuO5-PRa (a), as-CuO6-PRa (b) and as-CuO7-PRa (c), as-CuO5-PRb (d), as-CuO6-PRb (e) and as-CuO7-PRb (f), respectively.

CHAPTER VII

CONCLUSION

In this research, the commercial CuO powder and the CuO powders prepared by the DT and PR methods were used to fabricate the CuO ceramics. The particle sizes of the prepared CuO powders were calculated using the Scherrer formula. The particle size of the CuO powder prepared by the PR method is smaller than that of the DT method. It was found that the particle sizes of the CuO powders prepared by these two methods increase with increasing the calcination temperature. The XRD results reveal that all of the prepared CuO powders exhibit the diffraction peaks corresponding to the CuO phase for monoclinic structure. Impurity phases cannot be detected from the XRD patterns of the CuO powders.

To investigate the dielectric and electrical properties of the CuO ceramics, the CuO powders calcined at the temperature range of 500 - 700°C as well as the commercial CuO powder were sintered at two different temperature of 900 and 950°C for 10 h in air. The crystal structure of all the sintered CuO ceramic samples can be indexed as the monoclinic structure similar to that of the CuO powders. The SEM images of the CuO ceramics revealed that the sintered CuO ceramics exhibit the obvious grain and grain boundary structure. Large amounts of porosity can be observed in most ceramic samples. In all cases the average grain size of the CuO ceramics increases with the increase in the sintering temperature. All of the CuO ceramics show giant dielectric constant behavior with the values of about $10^3 - 10^4$ at room temperature and of low frequency. The temperature and frequency dependence of the dielectric properties of these three sets of CuO ceramics, which were synthesized from the commercial CuO powder and the CuO powders prepared by the DT and PR methods, are similar. A Debye-like dielectric relaxation behavior can be observed in all CuO ceramic samples. The giant dielectric constant value drops rapidly to the low value at low temperature and high frequency. The rapid decrease in the dielectric constant is accompanied by the presence of the peak of the dielectric loss (tanδ and ε'') Both of the rapid decrease in the dielectric constant and the peak of the dielectric loss shift to the higher frequency with increasing the temperature. The dielectric relaxation behavior of the CuO ceramics can be fitted using the Cole-Cole model. The relaxation time of the relaxation process at various temperatures is obtained. As a result, the activation energies for the relaxation process can be calculated using Arrhenius law and were found to be in the range of about 0.140 - 0.280 eV.

The dielectric constant of these three sets of the CuO ceramics decreases after annealing in Ar. Interestingly, the reduced dielectric constant can be tuned to the initial value by re-annealing in O_2. These results should therefore be related to the concentration of oxygen vacancies at the surface layer of the CuO ceramics. The polarization at the interface between the inner part and the outmost surface layer may be responsible for the observed interesting dielectric behavior. The annealing in Ar and O_2 can cause the increase and decrease in the concentration of oxygen vacancies at surface layer, respectively. Consequently, the insulating surface of the as-CuO sample can be transformed to the semiconducting surface by annealing in Ar. Then, this semiconducting surface of the Ar-sample can be reversed to the insulating surface again by annealing in O_2. The polarization at the interface between the insulating surface and the semiconducting inner part can be introduced. On the other hand, the polarization at the interface between the semiconducting surface and the semiconducting inner part cannot be produced. Thus, the dielectric constant of the Ar-sample should be smaller than those of the as-sample and O_2-sample.

The electrical properties of the CuO ceramics are studied using the impedance spectroscopy. The complex impedance plot suggests that the CuO ceramics are electrical inhomogeneous. The electrical responses in the CuO ceramics can be identified as the electrode, surface layer, grain and grain boundary effects. The first two effects are assigned as the external effect and the other two are assigned as the internal effect. The annealing processes also have a remarkable influence on the electrical properties of the CuO ceramics. The resistance of the external part decreases after annealing in Ar. However, it can be enhanced to the initial value by annealing the Ar-sample in O_2.

The study of the effect of dc-bias on the dielectric and electrical properties of the CuO ceramics reveals that the dielectric constant decreases with increasing the dc-bias voltage. The related result is also observed in which the resistance of the external part also decreases with increasing the dc-bias. These dielectric and electrical behavior can be ascribed based on the jump of free charge carriers crossed the potential barrier at the external part.

The investigation of the effect of the compressive stress on the dielectric properties of the CuO ceramics reveals that both the dielectric constant and the dielectric loss increase with increasing the compressive stress to the a maximum value, then they begin to decrease with further increase in the compressive stress. This dielectric behavior can be ascribed based on the electrical polarization at interface between electrode and sample surface.

REFERENCES

REFERENCES

Ahmed Farag, I., Ahmed, M. A., Hammad, S. M., and Moustafa, A. M. (2001). Application of Rietveld Method to the Structural Characteristics of Substituted Copper Ferrite. **Cryst. Res. Technol.**, 36: 85–92.

Blythe, A. (1979). **Electrical Properties of Polymers**. Oxford. Cambridge University Press.

Bruce, P. G. (1987). Elsevier applied science. **Polymer Electrolyte Reviews**, 1.

Chung, S. Y., Kim, I., and Kang, S. (2004). Strong nonlinear current-voltage behaviour in perovskite-derivative calcium copper titanate. **Nat. Mater.**, 3: 774.

Cole, K. and Cole, R. (1941). Dispersion and Absorption in Dielectrics I. Alternating Current Characteristics. **J. Chem. Phys.**, 9: 341–351.

Cullity, B. and Stock, S. (2001). **Elements of X-ray Diffraction**. New Jersey. Prentice Hall.

Klein, R. (2007). **Dielectric Properties of Conductive Ionomers**. Doctoral thesis. The Pennsylvania State University.

Lasaga, A. and Cygan, R. (1982). Electronic and ionic polarizabilities of silicate minerals. **Am. Mineral.**, 67: 328–334.

Liu, J., Duan, C., Mei, W. N., Smith, R. W., and Hardy, J. R. (2005). Dielectric properties and Maxwell-Wagner relaxation of compounds $ACu_3Ti_4O_{12}$ (A = Ca, $Bi_{2/3}$, $Y_{2/3}$, $La_{2/3}$. **J. Appl. Phys.**, 98: 093703.

Liu, J., Sui, Y., Duan, C., Mei, W., Smith, R., and Hardy, J. (2006). $CaCu_3Ti_4O_{12}$: Low-temperature synthesis by pyrolysis of an organic solution. **Chem. Mater.**, 18: 3878–3882.

Lunkenheimer, P., Fichtl, R., Ebbinghaus, S., and Loidl, A. (2004). Nonintrinsic origin of the colossal dielectric constants in $CaCu_3Ti_4O_{12}$. **Phys. Rev. B.**, 70: 172102.

Macdonald, J. (2005). **Impedance Spectroscopy**. New York. Wiley.

Maensiri, S., Thongbai, P., and Yamwong, T. (2007). Giant dielectric response in (Li, Ti)-doped NiO ceramics synthesized by the polymerized complex method. **Acta Materialia.**, 55: 2851–2861.

Masingboon, C. (2008). **Giant Dielectric Properties of CaCu3Ti4O12 Ceramics prepared by solution growth method**. Doctoral thesis. Khon Kaen University.

Ming, L., Ferteira, A., and Sinclair, D. (2009). Relaxer ferroelectric-like high effective permittivity in leaky dielectric/oxide semiconductor induced by electrode effects: A case study of CuO ceramics. **J. Appl. Phys.**, 105: 114109.

Moulson, A. and Herbert, J. (2003). **Electroceramics. 2nd ed**. New York. Wiley.

Obaid, A. Y., Alyoubi, A. O., Samarkandy, A. A., Al-Thabaiti, S. A., Al-Juaid, S. S., El-Bellihi, A. A., and Deifallah-El, H. M. (2000). Kinetics of thermal decomposition of copper (II) acetate monohydrate. **J. Therm. Anal. Cal.**, 61: 985–994.

Raevski, I. P., Prosandeev, S. A., Bogatin, A. S., Malitskaya, M. A., and Jastrabik, J. (2003). High dielectric permittivity in AFe1/2B1/2O3 nonferroelectric perovskite ceramics (A=Ba, Sr, Ca; B=Nb, Ta, Sb). **J. Appl. Phys.**, 93(7): 4130–4136.

Ramirez, A., Subramanian, M., Gardela, M., Blumberg, G., Li, D., Vogt, T., and Shapiro, S. (2000). Giant dielectric constant response in a copper-titanate. **Solid State Commun.**, 115: 217–220.

Sarkar, S., Jana, P., and Chaudhuri (2008a). Colossal internal barrier layer capacitance effect in polycrystalline copper (II) oxide. **Appl. Phys. Lett.**, 92: 022905.

Sarkar, S., Jana, P., and Chaudhuri (2008b). Origin of electrically heterogeneous microstructure in CuO from scanning tunneling spectroscopy study. **Appl. Phys. Lett.**, 92: 142901.

Sarkar, S., Jana, P., Chaudhuri, B., and Sakata, H. (2006). Copper (II) oxide as a giant dielectric material. **Appl. Phys. Lett.**, 69: 212905.

Schonhals, A. and Kremer, F. (2003). **Broadband Dielectric Spectroscopy**. New York. Springer-Verlag.

Sinclair, D., Adams, T., Morrison, F., and West, A. (2002). $CaCu_3Ti_4O_{12}$: One-step internal barrier layer capacitor. **Appl. Phys. Lett.**, 80: 2153–2155.

Sinclair, D. and West, A. (1989). Impedance and modulus spectroscopy of semiconducting $BaTiO_3$ showing positive temperature coefficient of resistance. **J. Appl. Phys.**, 66: 3850–3856.

Subramanian, M., Dong, L., Duan, N., Reisner, B., and Sleight, A. (2000). High dielectric constant in $ACu_3Ti_4O_{12}$ and $ACu_3Ti_3FeO_{12}$ phases. **J. Solid State Chem.**, 151: 323–325.

Thongbai, P., Maensiri, S., Yamwong, T., and Yimnirun, R. (2008a). Giant dielectric properties of CaCu3Ti4O12/(Li,Ti)-doped NiO composites subjected to post-sintering annealing and compressive stress. **J. Appl. Phys.**, 103: 114107.

Thongbai, P., Masingboon, C., Maensiri, S., Yamwong, T., Wongsaenmai, S., and Yimnirun, R. (2007). Giant dielectric behaviour of $CaCu_3Ti_4O_{12}$ subjected to post-sintering annealing and uniaxial stress. **J. Phys: Condens Matter.**, 19: 236208.

Thongbai, P., Meansiri, S., and Yamwong, T. (2008b). Effects of grain, grain boundary, and dc electric field on giant dielectric response in high purity CuO ceramics. **Appl. Phys.**, 104: 036107.

Thongbai, P., Yamwong, T., and Maensiri, S. (2008c). Correlation between giant dielectric response and electrical conductivity of CuO ceramic. **Solid State Commun.**, 147: 385–387.

Thongbai, P., Yamwong, T., and Meansiri, S. (2008d). The sintering temperature effects on the electrical and dielectric properties of Li0.05Ti0.02Ni0.93O ceramics prepared by adirect thermal decomposition method. **J. Appl. Phys.**, 104: 074109.

Von Hippel, A. R. (1954). **Dielectric Materials and Applications**. Massachusetts. Massachusetts Institute of Technology (MIT) press.

Wang, C. and Zhang, L. (2006a). Oxygen-vacancy-related dielectric anomaly in $CaCu_3Ti_4O_{12}$: post-sintering annealing studies. **Phys. Rev. B.**, 74: 024106.

Wang, C. and Zhang, L. (2006b). Surface-layer effect in $CaCu_3Ti_4O_{12}$. **Appl. Phys. Lett.**, 88: 042906.

Yimnirun, R. (2006). Contributions of Domain-Related Phenomena on Dielectric Constant of Lead-Based Ferroelectric Ceramics under Uniaxial Compressive Pre-Stress. **Int. J. Mod. Phys. B.**, 20: 3409–3417.

Yimnirun, R., Ananta, S., Ngamjarurojana, A., and Wongsaenmai, S. (2005). Uniaxial Stress Dependence of Ferroelectric Properties of xPMN-(1-x) PZT Ceramic Systems. **Appl. Phys. A: Mater. Sci. Process.**, 81: 1227–1231.

Yimnirun, R., Ananta, S., Ngamjarurojana, A., and Wongsaenmai, S. (2006a). Effects of Uniaxial Stress on Dielectric Properties of Ferroelectric Ceramics. **Curr. Appl. Phys.**, 6: 520–524.

Yimnirun, R., Laosiritaworn, Y., Wongsaenmai, S., and Ananta, S. (2006b). Scaling Behavior of Dynamic Hysteresis in Soft PZT Bulk Ceramics. **Appl. Phys. Lett.**, 89: 162901–162903.

Yimnirun, R., Moses, P., Meyer, R., and Newnham, R. (2003). Dynamic compressometer for converse electrostriction measurements. **Rev. Sci. Instrum.**, 74: 3429–3432.

Yimnirun, R., Unruan, M., Laosiritaworn, Y., and Ananta, S. (2006c). Change of Dielectric Properties of Ceramics in Lead Magnesium Niobate-Lead Titanate System With Compressive Stress. **J. Physics D.**, 39: 3097–3102.

Zhang, K., Hong, J., Cao, G., Zhan, D., Tao, Y., and Cong, C. (2005). The kinetics of thermal dehydration of copper(II) acetate monohydrate in air. **Thermochim. Acta.**, 437: 145–149.

CURRICULUM VITAE

The author, Mr. Thanin Putjuso, was born on the 20th December 1977 in Suwannaphum District of Roi-Et Province, Thailand. From May, 1996 to March, 2000, he obtained his Bachelor degree in Physics from the Department of Physics, Faculty of Science at Khon Kaen University. In May, 2000, he started his graduate study at the same department and graduated in 2004. His M. Sc. thesis involved a study on effect of copper concentration on the thermo luminescence of LiF:Mg,Cu single crystal. He then worked as a lecturer in the Faculty of Science and Technology at Rajamangala University of Technology Rattanakosin, Khaikangwol Campus. In May 2007, he returned to his education, by pursuing his Doctoral's degree in the School of Physics Institute of Science Suranaree University of technology. His Ph.D. thesis was entitled "Giant dielectric properties of CuO ceramics" which was under the supervision of Assoc. Dr. Prapun Manyum. His Ph.D. study was supported by Rajamangala University of Technology Rattanakosin, Khaikangwol Campus. Thanin successfully completed his Ph.D. in March 2010. He now works as a Lecturer of Physics at Rajamangala University of Technology Rattanakosin, Khaikangwol Campus. His research of interest is on giant dielectric ceramics.